THE SIMULATION OF A NOVEL FAST NEUTRON PORTAL MONITOR AND THE DEVELOPMENT OF TEXCAAM, THE TEXAS CSI ARRAY FOR ASTROPHYSICAL MEASUREMENTS

A Dissertation

by

ERIC EVAN ABOUD

Submitted to the Graduate and Professional School of
Texas A&M University
in partial fulfillment of the requirements for the degree of

DOCTOR OF PHILOSOPHY

Chair of Committee,	Grigory V. Rogachev
Committee Members,	Jeremy W. Holt
	Sherry J. Yennello
	Dan G. Melconian
Head of Department,	Grigory V. Rogachev

May 2022

Major Subject: Physics

Copyright 2022 Eric Evan Aboud

ABSTRACT

The field of nuclear physics relies heavily on the innovation of detectors. Development of a next-generation fast-neutron detector with high position and timing resolution is essential for the advancement of nuclear science and applications. In particular, new neutron detection technologies may improve the regulation of dangerous materials such as highly enriched uranium (HEU) and weapons-grade plutonium (WGPu). Current generation portal monitors have limited sensitivity and usually do not utilize advantages that come with position sensitivity. Also, since the existing systems are normally based on the detection of thermal neutrons, active interrogation techniques with low energy neutron beams cannot be implemented. They also rely on increasingly expensive and rare ^{3}He . By designing a highly-segmented array of organic scintillators, we posit that we can overcome the limitations of the current-generation detectors as well as accurately and quickly identify these hard to detect fissile materials. Simulations and analyses were conducted as a proof-of-principle investigation to test the viability of this next-generation neutron detector.

Another innovation is the development of a detector apparatus that allows for the study of sub-Coulomb α-transfer reactions, the **Tex**as **C**sI **A**rray for **A**strophysical **M**easurements (TexCAAM). TexCAAM has been constructed in efforts to bring sub-Coulomb α-transfer reaction study capabilities through γ-ray spectroscopy to the Cyclotron Institute at Texas A&M University using radioactive ion beams. The development of this array has opened the possibilities to study questions such as the reaction rates of the hot-pp chain. This particular study may influence our understanding of the early universe and how the first generation of stars evolved, producing the necessary elements to create the current universal landscape and provide us with the elemental cradle of life. The full development of TexCAAM has provided the capabilities to study such reactions, among others.

DEDICATION

To my parents who have never given up hope for me. They have supported me in so many ways through the years. If not for them, I would not have achieved as much as I have nor would I be the man I am today. I would also like to dedicate my thesis to Dr. Michael Carroll, Dr. Janice Crawford, and Dr. Kevin Barnwell. Their amazing work has given me the motivation to overcome the most difficult of tasks, including the completion of my research and this dissertation.

ACKNOWLEDGMENTS

I want to thank my advisor, Dr. Grigory Rogachev, for not only his invaluable insight and teaching, but also his faith in me and patience with me. I would like to thank the rest of my committee, Dr. Jeremy Holt, Dr. Sherry Yennello, and Dr. Dan Melconian for their advice and input.

I would also like to thank Dr. Sunghoon 'Tony' Ahn who was like a second advisor to me. During his time at the Cyclotron Institute, he spent countless hours with me teaching me everything from science to electronics and software. I would like to thank Dr. Evgeniy Koshchiy for teaching me about design, construction, and detector testing and development.

I would like to thank Dustin Scriven, Dr. Cody Parker, Dr. Joshua Hooker, and the CENTAUR collaboration for their support and help with the neutron detector development work.

I would like to thank Dr. Marina Barbui, Dr. Kris Hagel , Dr. Antti Saastamoinen, Curtis Hunt, Logan Jeffery, Alex Ascione, as well as my entire research group for their support in the development and testing of TexCAAM.

I want to thank Dr. Jack Bishop, Dr. Cody Parker, Dr. Heshani Jayatissa, and Dr. Sriteja Upadhyayula for their incredible friendships, their invaluable support of me, and the knowledge that they passed on to me.

I would also like to thank Dr. Robert Burch for his patience with me and the entire machine shop staff, especially Larry Whitely, for their advice, training, and teachings.

Lastly, I would like to thank Dr. Brian Roeder and all of the cyclotron staff for providing beam for us as well as a great learning environment that has allowed me to learn about many different fields and practical skills.

CONTRIBUTORS AND FUNDING SOURCES

Contributors

This work was supported by a dissertation committee consisting of Professor Grigory V. Rogachev [advisor], Professor Jeremy W. Holt, and Professor Dan Melconian of the Department of Physics and Astronomy and the Cyclotron Institute, and Professor Sherry J. Yennello of the Department of Chemistry and the Cyclotron Institute.

Parts of the development of TexCAAM, including the energy and efficiency calculations and design elements, were performed by Logan Jeffery and Alexander Ascione under the supervision of Eric Aboud and Dr. Marina Barbui. All other work was conducted by the student independently under the instruction of members of the research group and the Cyclotron Institute.

Funding Sources

The works were supported by the National Nuclear Security Administration (NNSA) through the Center for Excellence in Nuclear Training and University Based Research (CENTAUR) under Award No. DE-NA0003841, by the U.S.Department of Energy, Office of Science, Office of Nuclear Physics, under Award No. DE-FG02-93ER40773, and the College of Science at Texas A&M University through the Strategic Transformative Research Program (CoS STRP).

The student was also supported by the Nuclear Solutions Institute's Graduate Student Merit Fellowship.

TABLE OF CONTENTS

LIST OF FIGURES

FIGURE Page

LIST OF TABLES

TABLE Page

1. INTRODUCTION

The field of nuclear physics started with the discovery of radioactivity by Henri Becquerel in 1896. The possibilities of the nucleus were almost immediately realized with scientists such as Frederick Soddy, saying that it could change the world or transform the whole world into a "smiling Garden of Eden" [18]. As early as 1914, nuclear power was brought to science fiction writing, and the public's eye, in H.G. Well's book *The World Set Free*. In the past century, radioactivity has had its place in every household from uranium glass dinnerware to smoke detectors. The immense power of the nucleus has led to the development of nuclear reactors that can power energy grids or power vessels like aircraft carriers and submarines. In 1957, Ford even made a concept car called the Ford Nucleon that was fueled by uranium, however, it was never realized due to the immense cost of it.

Over the past century, our knowledge of nuclear physics has made giant leaps. Facilities such as the Cyclotron Institute at Texas A&M University have allowed us to probe fundamental questions about radioactive nuclei and enlighten our understanding of the universe, whether it's the fundamental properties of the nucleus or how the universe came to be through nucleosynthesis and similar processes. In the process, complex and novel radiation detectors have been developed, and continue to be developed, to answer the evolving questions of the nucleus. Detectors such as TexCAAM, the Texas CsI Array for Astrophysical Measurements, and the novel fast neutron detector TexNeut are among those detectors that will allow for novel discoveries and further push our understanding of nuclear physics as a whole.

1.1 Fundamentals of Nuclear Physics

Nuclear physics revolves around radioactive decay, where a parent nucleus decays into a daughter nucleus, usually via α, β, or γ decay or fission. The daughter nucleus, which can be the same isotope as the parent nucleus, can further decay via nucleon emission or any of the other decay methods. Our understanding of the properties of both the parent and daughter nuclei can be probed by detecting the decay products.

1.1.1 Excited states and the Nuclear Shell Model

Nuclear excited states are the basis of nuclear physics. As we can have excited electrons in an atom, we can have excited nucleons in a nucleus. Excited states in the nucleus occur when energy is added to the nuclear core, in the form of rotation or vibrations, or when an individual nucleon is moved to a higher energy state. Excited states are determined by quantum mechanics and are characterized by a state's angular momentum, parity, and isospin. Commonly, states are denoted in the J^π notation, referred to as spin and parity, such as a 0^+ or 2^+ state. The shell model describes the structure of the nucleus as shells, where nucleons fill in a specific order according to the Pauli Principle.

Similar to in chemistry, the nucleons sequentially fill orbitals denoted as *s,p,d,f,g,h,i,* and *j* (*l*=0,1,2,3,4,5,6). The occupation number, given by the Pauli principle, is (2*j*+1) which arises from the degeneracy of the total angular momentum quantum number (m_j). Shell closures, or magic numbers, appear when shells are completely filled which creates gaps between the shells (labeled in Figure 1.1). The original nuclear shell model potential was based on a combination of an infinite well and a harmonic oscillator. However, this did not reproduce the shell closures that were found experimentally. Instead, multiple terms have been added as corrections to the potential. By including a spin-orbit potential, the second term, and a Coulomb potential, the third term, shells are accurately reconstructed using the Woods-Saxon potential [19]:

$$V(r) = \frac{-V_0}{1 + exp[(r-R)/a]} + V_{so}\frac{df_{SO}(r)}{rdr}\boldsymbol{l}\cdot\boldsymbol{s} + V_C(r) \tag{1.1}$$

with V_0 being the well depth that is determined by the separation energies, R=1.25$A^{1/3}$ fm (mean radius), a being the diffuseness, V_{so} being the spin-orbit potential, l being the angular momentum,s being the spin, and V_C is the Coulomb potential. The spin-orbit fermi shape, $f_{SO}(r)$, is defined as:

$$f_{SO}(r) = \frac{1}{1 + exp[(r-R_{SO})/a_{SO}]} \tag{1.2}$$

The Coulomb term, V_C, is defined as:

$$V_C(r) = \frac{Ze^2}{r} \;\text{ for }\; r \geq R_C \tag{1.3}$$

or

$$V_C(r) = \frac{Ze^2}{r}\Big[\frac{3}{2} - \frac{r^2}{2R_C^2}\Big] \;\text{ for }\; r < R_C \tag{1.4}$$

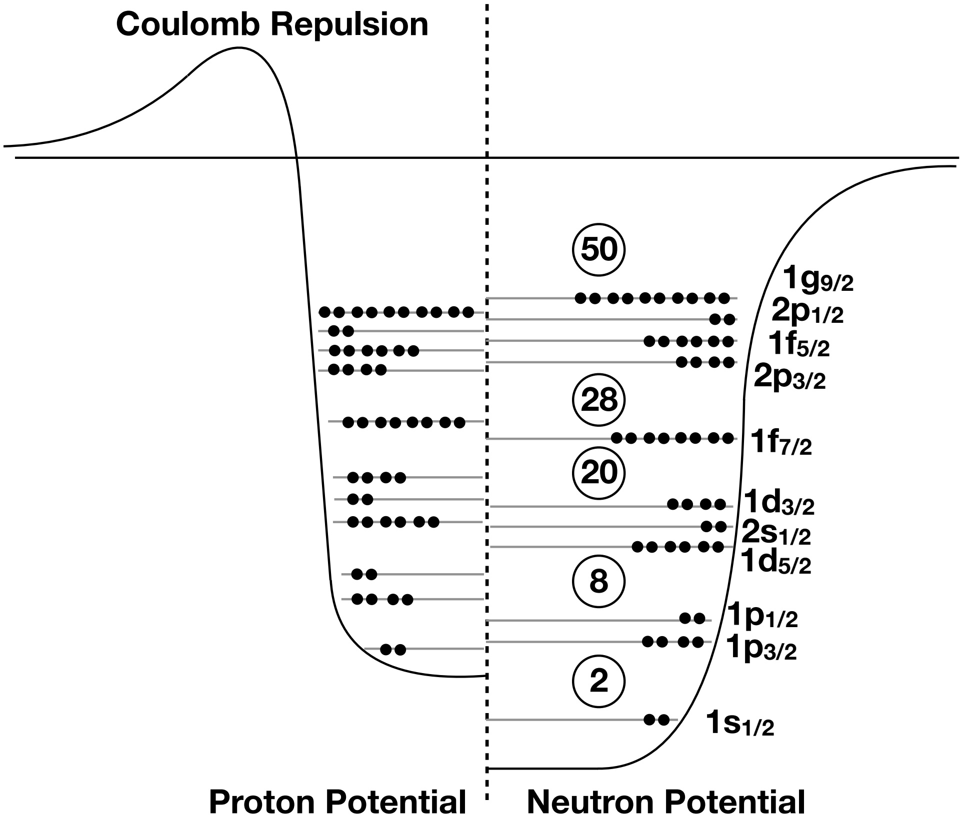

Figure 1.1: The Woods-Saxon potential for both protons and neutrons. A few shells are also depicted to show how the nucleons are filled in each of the levels. The shell closures, or magic numbers, are shown in the gaps between the shells.

Accordingly, the Woods-Saxon potential is different for protons and neutrons. The proton potential well is shifted up and will observe the effect of Coulomb repulsion (Figure 1.1). However, both neutrons and protons observe the same shell structures and fill the same way.

1.1.2 α Decay

The Coulomb force grows as Z^2, therefore as we look at heavier nuclei we see a stronger Coulomb repulsion effect. As the nuclear binding energy grows proportional to A, we see a point in which the Coulomb repulsion energy overcomes the nuclear binding energy. When this occurs we may observe spontaneous α emission. Since an α particle is tightly bound, very stable, and has a low mass, heavier nuclei tend to decay by emitting α particles with large amounts of kinetic energy (typically around 5 MeV to 10 MeV). Residual daughter nuclei are often themselves α or β radioactive [19].

Spontaneous α emission can occur when the α Q-value (Q_α) is greater than zero. Q_α is defined as the difference between the binding energies for the parent, daughter, and α nuclei:

$$Q_\alpha = B(N-2, Z-2) + B(2,2) - B(N, Z) \tag{1.5}$$

where B(2,2) is 28.296 MeV. Q_α generally becomes positive above $Z \sim 50$.

1.1.3 β Decay

β decay can take one of three forms: β^--decay, β^+-decay, and electron capture (ε). During beta decay, a neutron (β^--decay) or a proton (β^+-decay) is transformed into the other releasing an electron or positron, respectively. For this to occur, one of the quarks in the nucleon changes flavor, emitting a W boson which leads to the creation of the electron or positron. In each case, an electron neutrino or antineutrino is released to conserve lepton number and subsequently take a part of the kinetic energy from the reaction resulting in β particles having a continuous energy distribution instead of discrete energy.

Unlike the traditional β-decay methods, electron capture (ε) can occur when an inner atomic electron is captured by a proton. The proton then transforms into a neutron and the process releases a neutrino. ε is allowed where β^+-decay is energetically allowed and is a competing decay method in these situations. However, ε is also allowed in proton-rich nuclei where there is not enough energy for β^+-decay to occur. β^+ decay is energetically allowed when the mass excess of the parent nucleus is greater than that of the daughter nucleus by more than $2m_ec^2$ (two electron rest masses).

For the traditional β decays, β^--decay, and β^+-decay, two types of transitions are allowed: Fermi decay and Gamow-Teller decay. The process selection is determined by the spins of the electrons and neutrinos. The electron and neutrino both have spins of $\frac{1}{2}$ and can spin parallel or anti-parallel to one another. If the spins are anti-parallel (Fermi decay) then the nuclear spin cannot be changed. If the spins are parallel (Gamow-Teller) then the nuclear spin can remain the same or change by 1. However, transitions from a 0 spin state to another 0 spin state are purely Fermi decay as Gamow-Teller transitions must carry a unit of angular momentum. In either case, a parity change does not occur for allowed β decay. Larger isospin changes, as well as parity changes, can occur under “forbidden" β decays (Table 1.1).

Transition	**L**	**ΔI**	**$\Delta\pi$**
Fermi	0	0	0
Gamow-Teller	0	0,1	0
First-Forbidden	1	0,1,2	1
Second-Forbidden	2	2,3	0
Third-Forbidden	3	3,4	1
Fourth-Forbidden	4	4,5	0

Table 1.1: β-decay selection rules in terms of L, angular momentum, ΔI, change in isospin, and $\Delta\pi$, change in parity. This table is adapted from the β-decay selection rules table found in [15].

1.1.4 γ Decay

Unlike the previous decay methods, γ decay occurs when the parent and the daughter nucleus are the same. During γ decay the nucleus doesn't undergo a change to the number of neutrons and protons that are in it, but rather the nucleus deexcites and emits a γ ray. γ decay may occur after another decay or after a reaction takes place, leaving the nucleus in an excited state.

During γ decay, the γ ray carries away at least one unit of angular momentum from the nucleus. The γ ray can also cause a parity change during the decay. This is determined by the multipolarity of the γ ray. The parity change for electric multipoles goes as $(-1)^l$ and for magnetic multipoles, it goes as $(-1)^{l-1}$. Table 1.2 shows the multipolarity, the angular momentum, and the change of parity for five magnetic and five electric multipolarities.

Multipolarity (Magnetic)	**Angular Momentum (l)**	**Parity Change**	**Multipolarity (Electric)**	**Angular Momentum (l)**	**Parity Change**
M1	1	No	E1	1	Yes
M2	2	Yes	E2	2	No
M3	3	No	E3	3	Yes
M4	4	Yes	E4	4	No
M5	5	No	E5	5	Yes

Table 1.2: A table displaying the correlation between parity change and angular momentum for various magnetic and electric multipolarities. As a nucleus γ decays the γ ray carries a non-zero amount of angular momentum with it. The quanta for angular momentum, along with the multipolarity, determine the parity difference between the initial and final states.

1.1.4.1 Pair Production

γ rays of energies above 1022 keV can undergo pair production where the photon can spontaneously produce an electron and positron pair. 1022 keV is the minimum energy required to produce a 511 keV electron and a 511 keV positron, where 511 keV is the rest energy of an electron. However, it is important to understand the energy ranges of the detection processes that occur for γ-ray spectroscopy. The photoelectric effect, or the complete absorption of a γ ray in a material such as a detector, is the primary detection mode at energies below 0.1 MeV. Above that energy and below 2.5 MeV the detection mode is split between photoelectric effect and Compton scattering. Compton scattering is an inelastic scattering on a charged particle where the photon loses some of its energy. Generally in this region a photon will Compton scatter until the energy is sufficiently low in order to undergo photoelectric effect. Above 2.5 MeV (2.5 MeV for large Z such as U or Pb) Compton scattering is accompanied by pair production. As the photon produces the electron-positron pair the remaining energy above 1.022 MeV is split between the two products as kinetic energy.

1.1.5 Spontaneous and Induced Fission

Fission is a product of binding energy, as a nucleus becomes heavier the binding energy per nucleon is less favorable than if the nucleus split into two fragments. These two fragments will be more tightly bound systems than the original nucleus and energy will be released in the process. The release of energy is favorable in many applied scenarios such as fission reactors. In order for the fission process to occur, the Coulomb barrier has to be overcome, which requires an amount of energy known as the activation energy or fission barrier (Figure 1.2). The two types of fission processes are spontaneous and induced fission. Spontaneous fission is when the fission process competes with other decay modes, making it a major decay type for a specific nucleus. Fission will occur naturally at a rate determined by effects from non-spherical structures. The deformed liquid drop model is used to estimate the non-spherical nature of a heavy nucleus prior to fission. A ‘fissility parameter’, x, is defined to determine the favorability condition for fission to occurr [20]

$$x = \frac{Z^2/A}{(Z^2/A)_{crit}} \approx \frac{Z^2}{50A} \tag{1.6}$$

Very accurate nucleus deformation calculations have been done with up to 2.6 million grid points to accurately estimate elongation, mass asymmetry, neck and fragment deformations, as well as mathematical features such as saddle points and valleys [21]. Spontaneous fission becomes a more favorable decay mode in nuclei that are $A >\sim 230$ [20, 1].

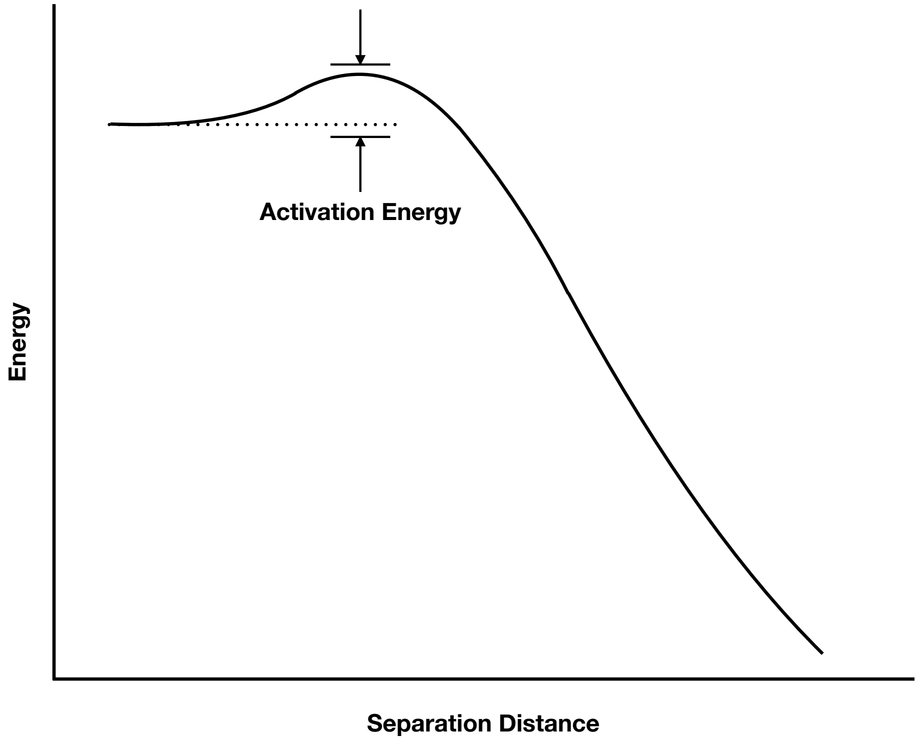

Figure 1.2: A plot showing the necessary activation energy to excite a nucleus (specifically ^{238}U for this case) above the Coulomb barrier so that fission can occur. This figure was reproduced from one found in [1].

Induced fission is the second type of fission mode. Induced fission is when a heavy nucleus is granted the energy needed to overcome the Coulomb barrier. These nuclei don't undergo spontaneous fission alone or their spontaneously fissioning decay branch is very small. One example is ^{235}U where fission can easily be induced by introducing a neutron. This neutron may come from a neutron generator or a neighboring decay. In fact, neutron emission in certain heavy elements can fuel induced fission in neighboring nuclei. When a mass of this heavy element can sustain continuous fission, this is called critical. If the rate of fission is uncontrolled, or the fission process grows exponentially, then it is considered supercritical. In criticality studies, the effective neutron multiplication factor (k_{eff}) is used to denote the criticality of a system. If $k_{eff} < 1$ the system is considered subcritical, if $k_{eff} = 1$ the system is considered critical, and if $k_{eff} > 1$ the system is considered supercritical. The quantity k_{eff} is just the average number of neutrons that cause new fission events. For the case of inducing fission in ^{235}U, the ^{235}U will capture the neutron and become ^{236}U for a very short time before it fissions. This is important when considering safeguards, which will be mentioned later. ^{235}U is difficult to detect because it won't decay on its own, however inducing fission makes it much easier to detect. In the quantities being sought the system cannot enter the critical or supercritical states during the fission-inducing process.

1.2 Radiation Detection

In order to study the nucleus, one must detect and infer from the products of a nuclear reaction. An early example is Ernest Rutherford's gold-foil experiment where an α-particle emitter was used to determine the scattering angles on a gold foil. From this experiment, Rutherford developed his model of the atom, where a tightly formed nucleus is surrounded by a large area of orbiting electrons.

Scintillators, as well as semiconductor detectors, make up the majority of current detectors used. The detector chosen is dependent on the type of radiation being detected as well as detection efficiency and energy resolution. Energy resolution is a product of drift in operating characteristics of the detector and data acquisition, random noise in the detector and data acquisition, and statistical noise. Statistical noise is a property of the detector chosen as it derives from the generation of discrete charge carriers during interactions with the detector. Detection efficiency is also a property of the chosen detector. Efficiency, for interactions such as γ-ray spectroscopy and neutron detection, is usually substantially lower than 100% as neutral radiation must undergo significant interactions to deposit their energies. As a product, these particles can partially interact or not interact at all before leaving the detector array.

1.2.1 γ-ray Detection

As mentioned in section 1.1.4.1, the energy of a γ ray directly affects the process in which it is detected. There are a few modes of γ-ray detection: the Photoelectric effect, Compton scattering, and Pair Production (which was described in section 1.1.4.1).

1.2.1.1 Photoelectric Effect

The first mode of γ-ray detection is the photoelectric effect and it is the dominant mode at extremely low energies ($< 100\ keV$). In this process, a γ ray is directly absorbed by the detection medium. Particularly, the γ ray will produce a photoelectron by converting all of its energy to electron kinetic energy. The energy of the photoelectron will be equal to the energy of the γ-ray energy (minus a small activation energy, on the order of 1 eV). The energy of this photoelectron is measured by charged-particle detectors, such as HPGe or scintillators, providing information on the initial energy of the γ ray.

1.2.1.2 Compton Scattering

Another process is dominant above the photoelectric effect energies up to about 2.5 MeV (Z dependent). This is the Compton Scattering mode. A photon will scatter off of an electron in the detection medium. The angle of scattering determines the amount of energy transferred to the electron. Since all possible angles can be observed, we observe a continuum of energies (i.e. the Compton continuum) behind the photopeak. This occurs up to a maximum energy (i.e. the Compton edge) where the angle of the scattering is maximum (π). A γ ray may observe multiple Compton scatters in the detector volume, losing more and more energy each time it scatters. The γ-ray energy may reduce to the point where the photoelectric effect will become dominant again.

1.2.1.3 CsI(Tl) as a γ-ray Spectrometer

Two popular choices for γ-ray detection are CsI and high-purity germanium (HPGe), among others. CsI, or CsI(Tl) (thallium doped CsI), is a scintillator detector that γ rays can propagate through, interact with, excite electrons, and transfer a fraction or all of the energy to the electron.

The electrons will lose energy as they propagate through the crystal and a small fraction of this energy will be converted to visible light through a complex multi-step mechanism which involves luminescence. The thallium doping in the CsI crystal improves the luminescence at room temperatures, shifts the wavelength of the emitted photons, and in turn, improves the detection efficiency. Generally, the scintillator will be wrapped in a reflective foil that will direct the photons from the fluorescence back into the crystal at the surfaces. The photons are then directed to the semiconductor photodiode that will collect the light and produce a voltage signal which can be read out. CsI, as a scintillator, is also sensitive to other forms of radiation such as electrons and other charged particles. The characteristics of CsI(Tl) as a γ-ray spectrometer will be probed further in the sections below.

1.2.1.4 Escape Peaks

Escape peaks are a phenomenon that is a direct result of pair production, as described in section 1.1.4.1. The positron will annihilate creating two photons that can be detected. However, these photons can go undetected resulting in an energy deposition equal to the photopeak energy minus the rest mass of an electron (if only one photon is lost). If both are lost, an energy deposition equal to the photopeak minus the rest mass of two electrons can be observed. If one is lost it is referred to as an escape peak, and if two, a double escape peak. In some cases, escape peak information can be utilized to probe photopeak information to determine values such as γ-ray intensities [22].

1.2.2 Neutron Detection via Scintillation Detectors

There are two types of neutron detection modes. The first is thermal neutron detection, which uses thermalized neutrons, and the second is fast neutron detection.

1.2.2.1 Thermal Neutron Detection

Thermal neutron detection relies heavily on the thermalization of neutrons to make them detectable. Generally, a neutron moderator can be used to induce a series of scatterings that allow the neutron to lose its energy. Once the neutron is of sufficiently low energy, the neutron capture cross-section for reactions such as ^{3}He(n,p) will be large enough to efficiently detect the neutrons.

As described in section 2.1, the international supply of ^{3}He is limited and the production of such detectors is increasingly difficult. Multiple thermal neutron detector types exist, however for the scope of this work ^{3}He detection methods will be described.

As a thermal, or slow, neutron enters the ^{3}He the gas will absorb the neutron. The neutron capture in ^{3}He produces a proton (^{3}He(n,p)) which is typically measured using proportional counter techniques. The thermal neutron capture cross-section for the ^{3}He(n,p) may be up to 5330 barns [23].

1.2.2.2 Fast Neutron Detection

Fast neutron detection relies on neutron scattering in a medium such as an organic scintillator. Fast neutrons have a large cross-section for scattering on hydrogen and a slightly lower cross-section for scattering off of carbon. Naturally, hydrocarbon (or organic) scintillators are used to detect these fast neutrons. Fast neutrons can elastically scatter off of the hydrogen and can deposit all of its energy into the recoiling hydrogen atom. This produces an excitation in the hydrocarbon molecule that produces fluorescence. The photons produced during the excitation of the hydrocarbon permeate through the crystal, oftentimes redirected on the surface of the crystal using specular film. The photons are directed to the light-collection device such as a photomultiplier tube (PMT) or a silicon photomultiplier (SiPM).

Examples of organic scintillators used for fast-neutron detection are *para-terphenyl* (*p-terphenyl*) and stilbene. *P-terphenyl* [$C_{18}H_{14}$] has a light output of about 20,000 ph/MeV and a decay time of 14.1 ns [24]. *P-terphenyl* is especially interesting as it has a high light output and has great pulse-shape discrimination (section 1.2.3.1).

1.2.2.3 Light Collection Photodiodes

The three types of light-collection devices used in this work are photomultiplier tubes (PMTs), silicon photomultipliers (SiPMs), and Si PIN diodes. Photomultiplier tubes use an array of dynodes to multiply the electrons produced when the photons interact with the photocathode, which converts the photons to electrons. The electrons produced at the photocathode are focused, using focusing electrodes, to the start of the dynode array. In the dynodes the electrons deposit their energy which can cause secondary electron emission, causing the re-emission of more than one electron. The number of secondary electrons depends on the dynode potential and the number of primary electrons hitting the dynode [23]. This process continues through an array of dynodes, producing more secondary electrons at each of the dynodes. Eventually, the electrons are directed to the anode, which produces a current when the electrons hit it. This current is then read out as the signal.

Silicon photomultipliers are semiconductor photodetectors. A SiPM is a pixelated array of avalanche photodiodes (APDs) and quenching resistors. The array of APDs is connected in parallel, needing only one anode and one cathode. The SiPM is biased such that the voltage on each APD is above its breakdown voltage, which is called an overvoltage. Once the SiPM absorbs a photon, the charge carrier triggers an avalanche in the APD. The avalanche can produce 10^5 to 10^6 charge carriers [25]. The quenching resistor then recovers the APD back to overvoltage, readying it for another detection. SiPMs offer a substantial decrease to the size of the photomultiplier, with a size on the order of millimeters in length and width and around a millimeter in thickness. SiPMs generally require reflow soldering onto a PCB which can be designed to minimize the necessary clearance for the photodetector arrays, reducing the impact on the detector geometry when compared to PMTs.

Relatively similar to SiPMs, silicon PIN diodes are often used because they are virtually insensitive to magnetic fields and they have a very small footprint compared to PMTs [23]. Si PIN diodes are conventional photodiodes instead of the avalanche photodiodes used in SiPMs. A PIN diode is a p-n junction (p-type semiconductor coupled to an n-type semiconductor) intersected by an intrinsic (i) semiconductor, hence the PIN diode naming. A photon can be detected by creating electron-hole pairs inside of the intrinsic (depleted) region. The charges are collected at the boundaries and the current is recorded. For the CsI(Tl) detectors, the signal is processed by an on-board preamplifier. PIN diodes, unlike SiPMs or PMTs, are unity gain devices and are therefore normally used with the brightest of scintillators, such as CsI(Tl).

1.2.3 Waveforms and Their Properties

Detectors are read out by observing a change in the current, such as an abundance of electrons hitting an anode in the case of a PMT. This surge in current produces a voltage change which can decay over time, the time depending on the detector. For the case of fast-neutron detection, a quick rise and a short decay are observed. For TexCAAM, a γ-ray signal produces a relatively long decay time (Figure 1.3).

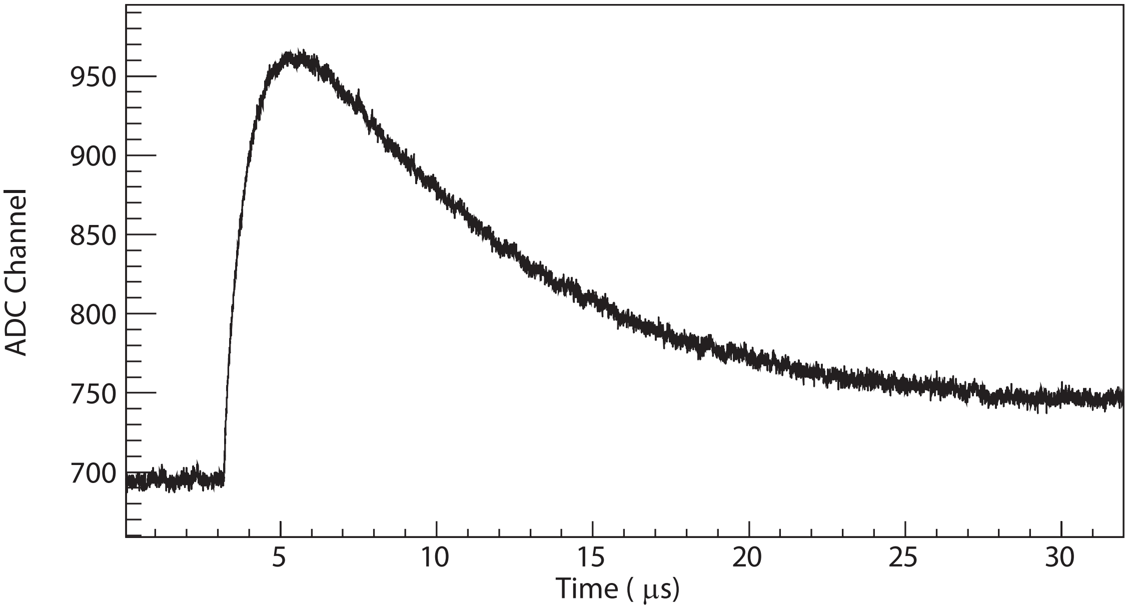

Figure 1.3: A typical CsI waveform after digitization through STRUCK.

The decay signature is unique to the interaction process. For example, a neutron scatting off of a proton produces a slightly different decay signature than a photon being absorbed and exciting an electron in some scintillator materials. The difference in these decay signatures can be exploited to determine the particle of interaction, allowing for pulse-shape discrimination.

1.2.3.1 Pulse-Shape Discrimination Techniques

There are various techniques to perform pulse-shape discrimination. PSD used to require novel and complicated circuitry in order to separate the fine differences between the waveforms [26]. Fortunately, computers have made PSD easier and a lot more sophisticated. A simple PSD technique (Figure 1.5) shows neutron/γ separation in *p-terphenyl* using SiPMs. This technique simply takes the amplitude of the signal and compares it to the ratio of the amplitude and the charge (the integral of the waveform). Much more sophisticated techniques may be used to improve the PSD band separation. One of these techniques utilizes machine learning to lower the PSD threshold and lower the false-identification rate [27].

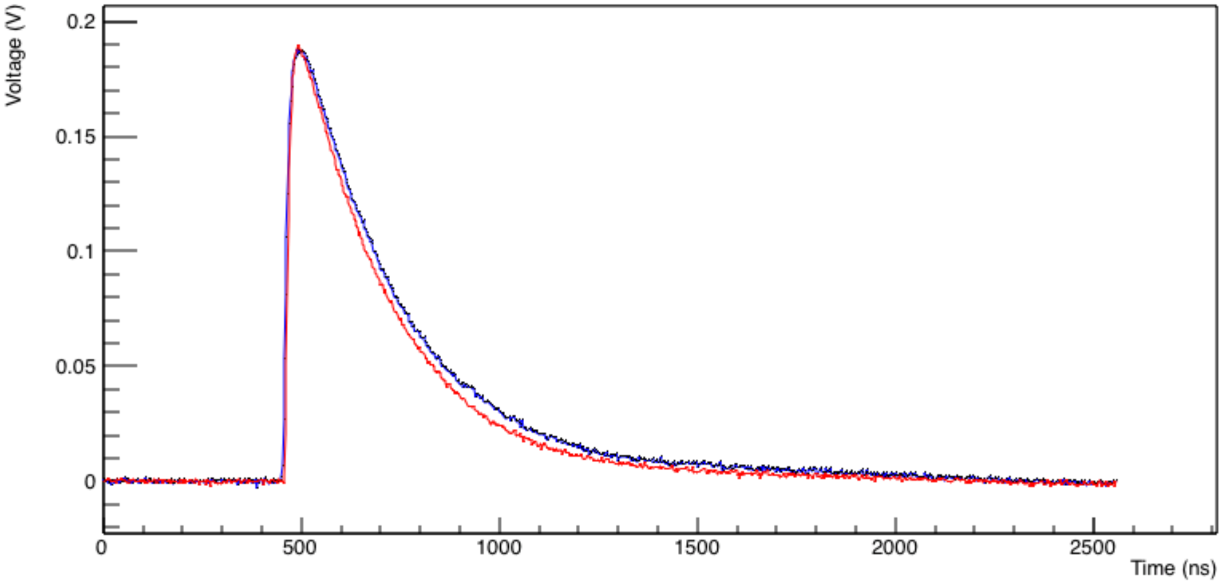

Figure 1.4: Two signals coming from SiPMs. One of the signals comes from a neutron interacting in *p-terphenyl* (blue online) and the second comes from a photon interacting with the *p-terphenyl* (red online). The slightly different waveform tails can be used to perform pulse shape discrimination.

The *goodness* of the PSD is defined in a quantity called the figure-of-merit (FOM). The FOM is simply defined as

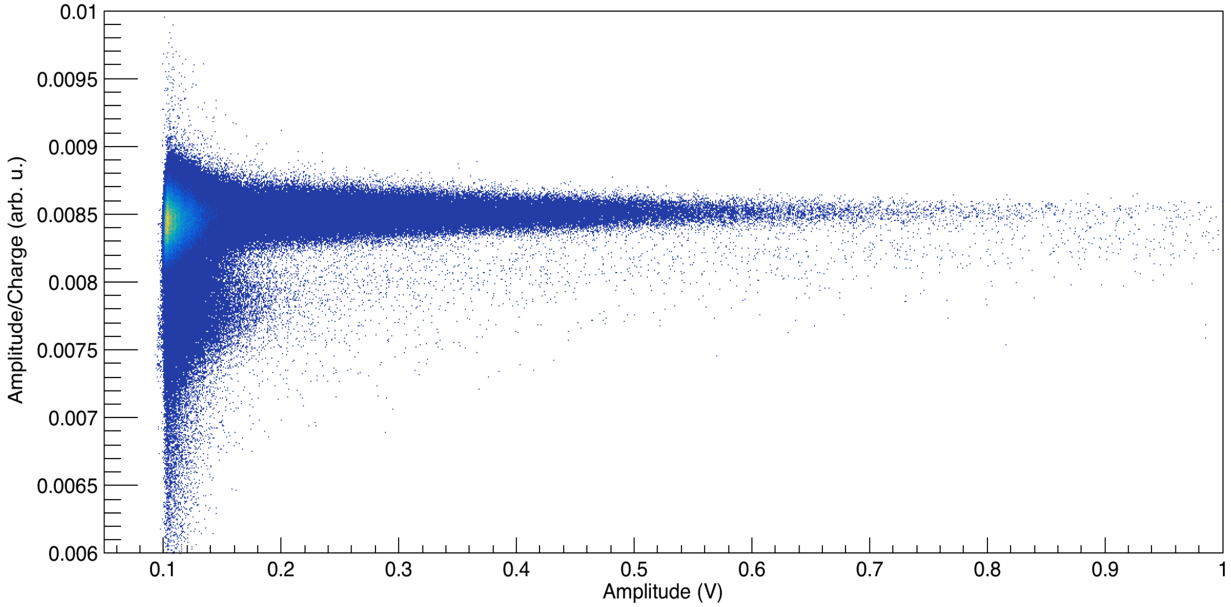

Figure 1.5: A simple type of pulse shape discrimination that shows a neutron (bottom band) and a γ-ray band (top band). This PSD was done with SiPMs and *p-terphenyl*. More advanced techniques can be used to separate the two bands further. Band separation in synonymous with particle identification confidence.

$$FOM = \frac{C_\gamma - C_n}{FWHM_\gamma + FWHM_n} \tag{1.7}$$

where C refers to the centroid of the γ or neutron (n) bands and FWHM is the full-width at half maximum of the bands.

I THE SIMULATION OF A MODULAR NEXT-GENERATION FAST NEUTRON DETECTOR FOR PORTAL MONITORING

2. BACKGROUND

2.1 Detection of Special Nuclear Materials

Special nuclear materials (SNM) such as ^{239}Pu , the main component of weapons-grade plutonium (WGPu), and ^{235}U , the main component of highly-enriched uranium (HEU), present a danger to the international community and should be strictly monitored. While WGPu emits a significant amount of neutrons, making it easier to detect with current methods, HEU is challenging since it has a low neutron emission rate and produces low-energy γ rays that can be easily shielded. Even though detection of these materials is difficult, these SNMs can be identified using γ-ray and neutron detection methods. A combination of the two methods is typically used since it allows for lower detection of natural background radiation and the identification of radioactive materials used in industrial and medical applications. However, the methods are not perfect and the false alarm rates for γ rays is about 1 in 10^2 and for neutrons about 1 in 10^4 due to naturally occurring radioactive materials and electronic noise or failures [28].

Current neutron portal monitoring techniques rely heavily on thermal neutron detectors, of which many require ^{3}He . ^{3}He is used universally with applications in many different fields, but it has a dwindling terrestrial supply [29]. ^{3}He is solely produced via tritium decay and available through only the USA and Russia. Production of ^{3}He corresponds directly with the stockpile of nuclear weapons as it is produced during the tritium cleaning process. As of 2010, the demand of ^{3}He was approximately 65 m^3 while the supply was approximately 20 m^3 [30]. This means that the current supply has become increasingly expensive and difficult to acquire [30, 31]. Due to this, efforts to move away from ^{3}He detectors have been an area of interest for more than a decade.

Thermal neutron detectors rely on moderating fast neutrons, which for SNMs generally average energies of around 1 MeV, to detector them. However, moderation of such low-energy neutrons can make them indistinguishable from ambient thermal neutrons. After moderation, these detectors rely on counting techniques, which are not position sensitive, to identify a source by looking for an increase in the total neutron flux. By detecting solely on a flux deviation, it doesn't allow the detectors to be sensitive to low-emission fissile materials [32, 33, 34]. These techniques may also be prone to high false alarm rates.

Active interrogation techniques can be used to enhance sensitivity to SNMS by inducing fission. Using a low-energy neutron generator, which may use the ^{7}Li(p,n)^{7}Be reaction to produce the neutrons, a beam of neutrons can be created with energies around a 60 keV. These neutrons induce fission in ^{235}U and ^{239}Pu while not inducing fission in other isotopes such as ^{238}U and ^{232}Th. The 60 keV neutron beam produces a small dose and can penetrate bulky materials nearly as well as higher-energy neutrons. These low-energy neutrons also lose their energy primarily from elastic collisions rather than reactions or inelastic scattering, creating an easily identifiable neutron background. Previous studies have shown positive results in the identification of small quantities of ^{235}U , even when shielded by various materials [35, 36, 37]. However, this technique is not usable for thermal neutron detectors as the generated neutrons would be indistinguishable from moderated source neutrons.

2.2 Current Techniques for Next-Generation Portal Monitoring

In an attempt to overcome the limitations of thermal neutron detection methods, various techniques have been tested. In 2012, Hausladen *et al.* [38] prototyped a fast-neutron coded-aperture imager that was made of a segmented array of custom-built liquid scintillator detectors (EJ-309) which backed a rank-19 modified uniformly redundant array coded aperture placed 67.3 cm from the detectors. While this detector was developed with the intention of counting the number of nuclear warheads present, it presents itself as a direct replacement of moderated thermal neutron detectors. To meet the goals of a compact pixelated detector with high efficiency and a workable amount of readouts, the design consisted of an array of 4 x 4 detector modules. Each of the modules consisted of a liquid scintillator volume segmented into a 10 x 10 array of 1 x 1 x 5 cm^{3} optically isolated liquid scintillators, which combined produced an overall detector with a size of 43 x 43 cm and consisted of 1600 pixels. The pixels for each module were read out by a 2.8 cm thick segmented acrylic light guide connected to four 51 mm Hamamatsu R9779 photomultiplier tubes. The PMTs were read out by an XIA Pixie-16 100MS/s waveform digitizer. Waveform amplitudes were used to calculate the pixel of interaction and the overall waveform was used to perform PSD.

The detector prototype was tested with SNMs, including HEU and WGPu, at the Idaho National Laboratory Zero Power Physics Reactor facility. Testing was completed with polyethylene shielded and unshielded ^{240}Pu with a mass of ∼96 g, as well as a 5.25 kg HEU source. Testing concluded that in a half-hours time the moderated and unmoderated ^{240}Pu sources were detectable and identifiable in both the neutron and γ-ray spectra. However, the HEU source was absent in the neutron spectrum and was only visible via γ-ray detection. The authors of the study presumed that it would take about 12 hours of statistics to identify the HEU neutrons with an acceptable signal-to-noise ratio. The result from the HEU is due to the low spontaneous fission rate of the uranium, but the same result was found when using the WGPu source to induce fission in the HEU. Ultimately the testing of the detector was successful for higher-rate neutron emitters such as plutonium but was unable to identify an HEU source in the time scale needed for portal monitoring.

Rose *et al.* (2016) [39] developed a method of spatial imaging utilizing high-energy γ rays ($E_\gamma > 4$ MeV) and fast-neutron active interrogation. Active interrogation is achieved using the ^{11}B(d,nγ)^{12}C reaction to produce a fast-neutron beam. The reaction also yields γ-rays with the energies of 4.438 MeV and 15.1 MeV. The ratio of the cross-sections gives insight on the atomic number for the element being scanned, as $\frac{\sigma_{pe}}{\sigma_C} \sim Z^{3-4}$ [39]. Similarly, the Rose *et al.* method can utilize the two primary γ energies 4.438 MeV, which is dominated by Compton scattering ($\sigma_C \propto Z$), and 15.1 MeV, which is dominated by pair production ($\sigma_{pp} \propto Z^2$), to probe the atomic number of the imaged element. However, a stated downside is that elemental mixtures cannot be adequately identified as it probes a singular effective atomic number. To accurately identify SNMs, they would then have to rely on the decay of the daughter nucleus, such as β-delayed radiation.

Relying on daughter decays, especially when using an active interrogation technique, poses a challenge based on the high intensity of the background. In the case of β-delayed neutrons (E∼0.5 MeV) it becomes difficult to separate from the photon background through methods such as pulse shape discrimination (PSD). While this can be overcome, another issue comes from having produced neutrons of energies around 0.5 MeV. Such low-energy neutrons are also susceptible to being shielded by whatever may surround the SNM.

Hamel *et al.* (2017) [40] proposed another active interrogation-based detector system, which was specifically designed to detect HEU, the most difficult of the SNMs to identify. The system begins with a deuterium-tritium (DT) neutron generator that produces neutrons of energies 14.1 MeV at a rate of $\sim$7x10^7 neutrons per second. The neutron generator induces fission events in the HEU which causes an increase in neutron and γ-ray flux. The study proposed a 'dual-particle imager' (DPI) which, as the name states, independently localizes both neutrons and γ-rays. The DPI uses a stochastic origin ensemble (SOE) statistical technique to perform image reconstruction in order to localize both γ-rays and neutrons [41]. For both Compton scattering and neutron scattering a backprojection cone can be constructed to determine the location of the source. However, a simple backprojection technique only gives a broad cone projection. To improve the resolution of the localization the SOE can be used with only the cone information and the angular resolution of the system.

The detector apparatus consisted of two planes separated 30 cm apart. The first plane is a 4 x 4 grid of EJ-309 liquid scintillators spaced 15 cm apart with each having a thickness of 5.1 cm and a diameter of 7.6 cm. The second plane, located behind the first, consists of mixture of the same EJ-309 liquid scintillators and NaI(Tl) scintillators, with the same thickness as the liquid scintillators, placed in a similar 4 x 4 grid but alternating in a checkerboard pattern spaced 25 cm apart.

Testing of the DPI system was done with a control setup (no SNM), three cases of HEU with different moderation, and a tungsten sphere without moderation. For the cases without the SNM, there was negligible rate change from control. However, with the HEU present, regardless of moderation, clear increases in both the neutron and γ-ray rates were found. Imaging was also done with a control and two HEU cases, one with HDPE moderation and one without moderation. In all three cases, the neutron generator was identified and in the cases with HEU present, localization of the HEU source was obvious in both the neutron and γ-ray images [40]. However, for the test cases, the observation time was on the order of 10 minutes to an hour. At the end of the collection time, it still requires a multi-step analysis to localize the sources.

3. MONTE CARLO SIMULATIONS

3.1 Design

In order to overcome the existing limitations of the current-generation neutron detectors, as well as provide a viable alternative to the ^{3}He-based thermal neutron detectors, a novel direct technique for fast-neutron portal monitoring is being developed. The new technique overcomes the sensitivity limitations of fast-neutron thermalization and can utilize neutron generators for active interrogation. By using small hydrocarbon, *para-terphenyl* or more commonly *p-terphenyl*, organic scintillators in a large array, the detector array is capable of detecting fast neutrons to localize SNMs such as HEU and WGPu. The large array is modular, allowing for different sizes and multiple detector arrays at various locations around a suspect payload.

For this simulation study we have chosen a 4000 *p-terphenyl* crystal array, each crystal having a size of 2.5 x 2.5 x 2.5 cm^3. The array is arranged with a size of 50 x 50 cm^2 in cross-section, relative to the source, and 25 cm deep. The cross-section size was arbitrarily chosen and the depth was specifically chosen as it is approximately two mean free paths of a 1 MeV neutron in *p-terphenyl* (Figure 3.1), which is the mode energy expected from a Watt fission spectrum for the SNMs of interest. For the purposes of the simulations, the crystals are grouped in layers of one crystal in height and have no space between the crystals in the x and y coordinates. Each of the layers is then stacked on top of one another with a spacing of 20 mm between the layers. An exploded view of the detector array is shown in figure 3.2. While a more realistic setup will likely result from the choice of light collection technology, the simulations were conducted with this idealized geometry.

Current testing has lead to the development of *pseudo-bars*, or reconstructed bars of *p-terphenyl* that allow for individual crystal energy and position sensitivity [42]. *Pseudo-bars* consist of 6 crystals with zero gap between them. The bar itself is wrapped with enhanced specular reflective film on the long sides while leaving the ends exposed. Each end is read out by Hamamatsu R1450 PMTs. The development of the *pseudo-bars* allows for the construction of a detector with virtually

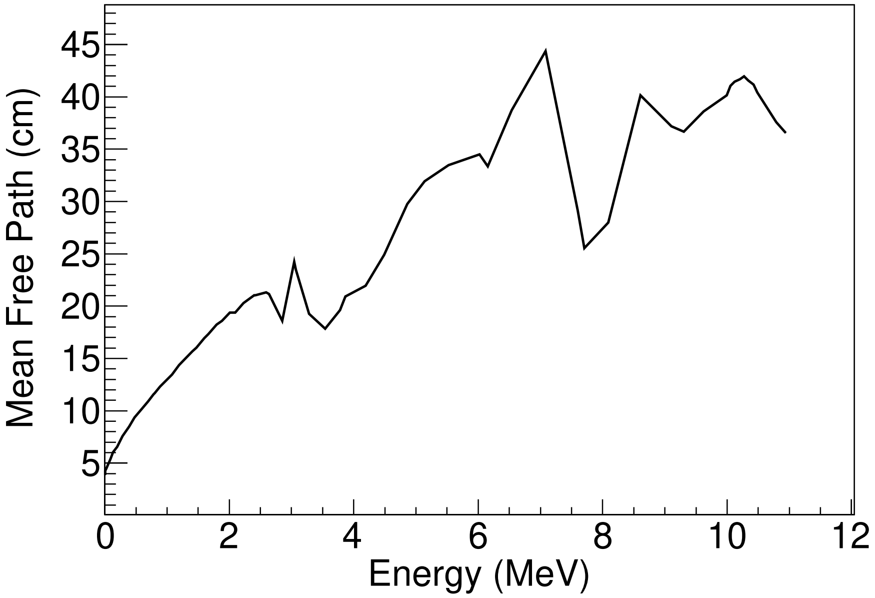

Figure 3.1: The mean free path of neutrons through *p*-terphenyl until the first collision for a range of energies up to approximately 11 MeV. The cross section data were taken from ENDF libraries [2, 3]. At 1 MeV, the mean free path is approximately 12.9 cm.

no gap between the crystals while retaining the position and energy resolution of individual crystals. The pseudo-bar based prototype array has been constructed at Texas A&M University and was commissioned in December of 2021.

3.1.1 Materials

The detector array consists of *p-terphenyl* [$C_{18}H_{14}$] organic crystalline scintillators. Due to its large light output (about 20,000 ph/MeV [24]), excellent time resolution (477(12) ps [43]), fast decay time (14.1 ns [24]), and exceptional pulse-shape discrimination (PSD), *p-terphenyl* has been of high interest in the fast-neutron detection community. These properties give confidence for positive neutron and γ-ray separation, resulting in accurate neutron identification, with good detection efficiency and fast response times. Previous studies have shown PSD for *p-terphenyl* down to about the 100 keVee level [44, 45]. Testing with the *pseudo-bars* has shown position resolution and PSD down to 150 keVee, which is in line with previous measurements of a 100 keVee level PSD threshold.

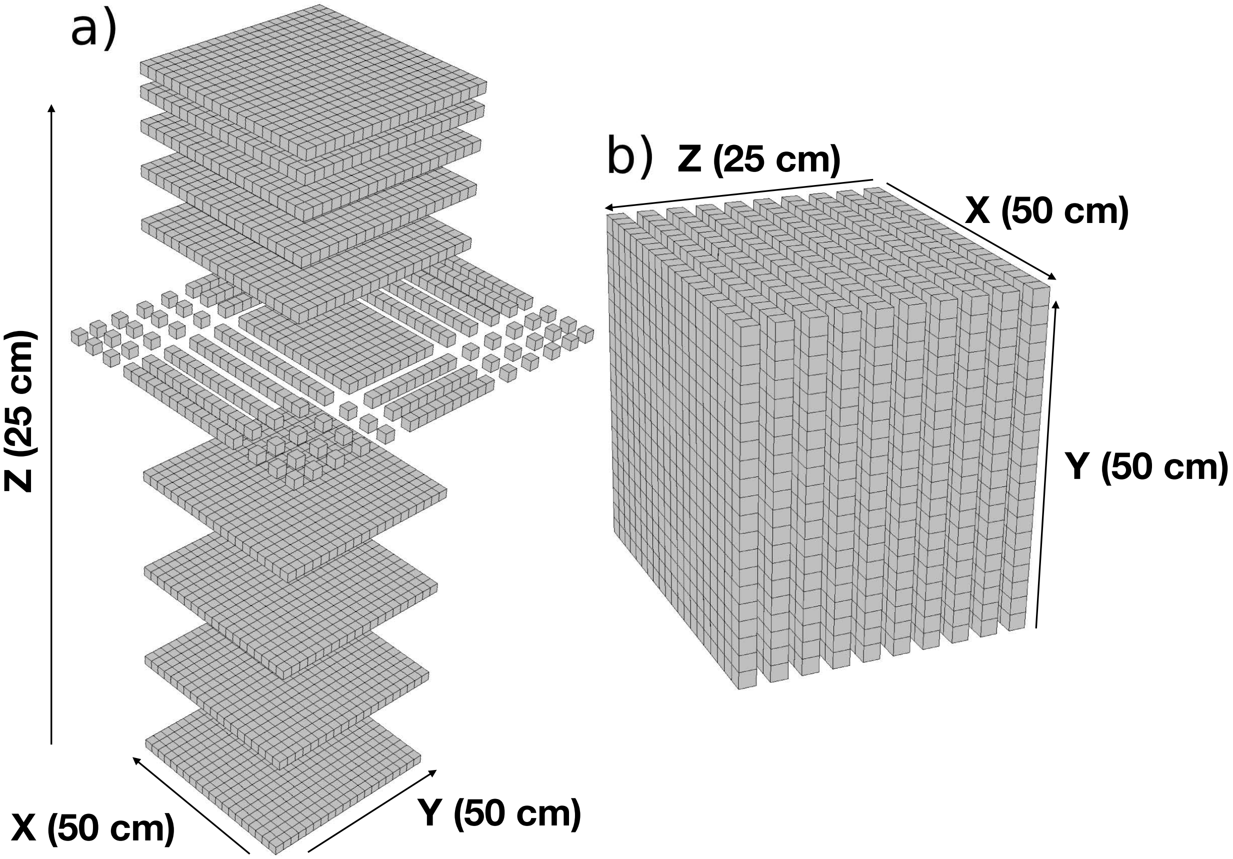

Figure 3.2: a) Exploded CAD drawing of how the scintillators of the proposed device may be distributed. This drawing serves to display the segmentation of the crystals and not the actual geometry of the detector. The cross-sectional face, the side facing the neutron source, is the side facing up. The cross-section is 50 cmx50 cm and the depth is 25 cm. The top third of the drawing shows the compact layer arrangement that the detector would have and the bottom two-thirds of the drawing are blown up to show the individual layers. The middle layer is further exploded to show the orientation of individual crystals. They are tightly arranged in each layer as shown in all other layers. b) A more realistic view of the neutron detector with appropriate spacing. The cross-sectional face, the face closest to the source, is facing to the left of the page.

3.2 MCNP6

MCNP6, or Monte Carlo N-Particle 6, is a simulation software developed for the simulation of single neutron events. However, it can accurately simulate photons, electrons, muons, neutrons, protons, heavy and light ions, as well as others [46]. MCNP6 achieves a large array of simulations due to a mixture of evaluated data libraries and theoretical models to provide a large energy range for each of the particles. Given the accuracy of the single-particle simulations, MCNP6 is widely used in fields such as nuclear engineering where it is possible to simulate small- and large-scale reactors. MCNP6 is also used frequently in radiation therapy situations such as medical physics.

MCNP6 offers a simple input file construction, which is in FORTRAN format. MCNP6 consists of 4 'cards' which contain all of the essential information for the simulation [47]. The cards are a cell card, a surface card, a source card, and a material card. While all four of the cards are directly dependent on each other, it allows for a simplified construction of the simulation. Of most importance is the source card which allows for the definition of the radioactive source which prompts the simulation. The simplicity of the source is determined by the user. Most 'complex' sources are predefined in libraries that allow the user to call and fine-tune the appropriate source.

The prebuilt libraries of MCNP6 allow for the most powerful simulations. MCNP6 has libraries available to accurately recreate the terrestrial neutron and photon backgrounds at various locations around the country and the world [48]. For the continental United States, there are 39 grid points for the terrestrial background. For the purposes of developing the neutron detector at Texas A&M University, the closest grid point at New Orleans, LA was chosen. At the ground level of this data point, the ambient neutron flux is 0.9907x10^{-2} n/cm^2/s. Libraries also exist to reproduce fission and reaction events such as the induced fission of ^{235}U+n. This particular library allows for a Watt fission spectrum to be produced. The Watt fission spectrum reproduces an array of energies, which has a mode of approximately 1 MeV, to accurately reconstruct the spread of neutron energies expected from the actual induced fission of ^{235}U. Implementing the Watt fission source in the source card mainly consists of looking up the correct identifiers to input.

Source definitions in MCNP6 allow for directional and solid angle biases. For example, a ^{252}Cf source can be placed a meter away from the source. Instead of just simulating this source as isotropic, computational power can be conserved by limiting the source particles to be spawned only in the direction and specific solid angle to hit the detector. The isotropic rate can then be recovered after the simulation, but few simulated particles will be wasted.

The output of the MCNP6 simulations can be defined by the user in either counting values, such as dosimetry measurements, or complete particle tracks. Particle tracks give interaction locations and energy deposition throughout the life of the particle before it loses all of its energy or escapes the world.

3.2.1 Simulations

For the simulation of the neutron detector both the ambient neutron background at New Orleans, LA as well as the Watt fission spectrum of ^{235}U+n was chosen to create as accurate a simulation to real life as possible. Given the size of the detector, given in section 3.1, and the ambient neutron flux of $0.9907\text{x}10^{-2}$ n/cm^2/s, it is expected that approximately 100 neutrons/s enter the detector from the background. The number of source neutrons can be defined in relation to the background neutrons in the form of a ratio. For example, one can set a total of 1 million neutrons to be spawned and define that 30% of those are background neutrons and the remaining are source neutrons. Given the known ambient neutron background rate, it is then possible to calculate the real-world time that the simulation occurs.

Various simulations were conducted for both the fast-neutron detector described and a current-generation ^{3}He detector [16]. Source distances and moderation materials were the most frequently changed variables between the simulations. Variations of simulations will be described later as they are used.

Analysis of the neutron tracks included recoil energy calculations [49] and a PSD threshold of approximately 100 keVee was used. Any neutron interactions below this threshold were discarded.

At this point it is also important to point out with the high modularity of the detector, similar analyses to Hamel *et al.* [41] can be used to localize a source using neutron scatterings between two crystals. The time of flight (TOF) for a fast neutron between two crystals may be small, but with the time resolution of around 600 ps for the *pseudo-bar* [42] most double-scattering events may be resolvable (Figure 4.1).

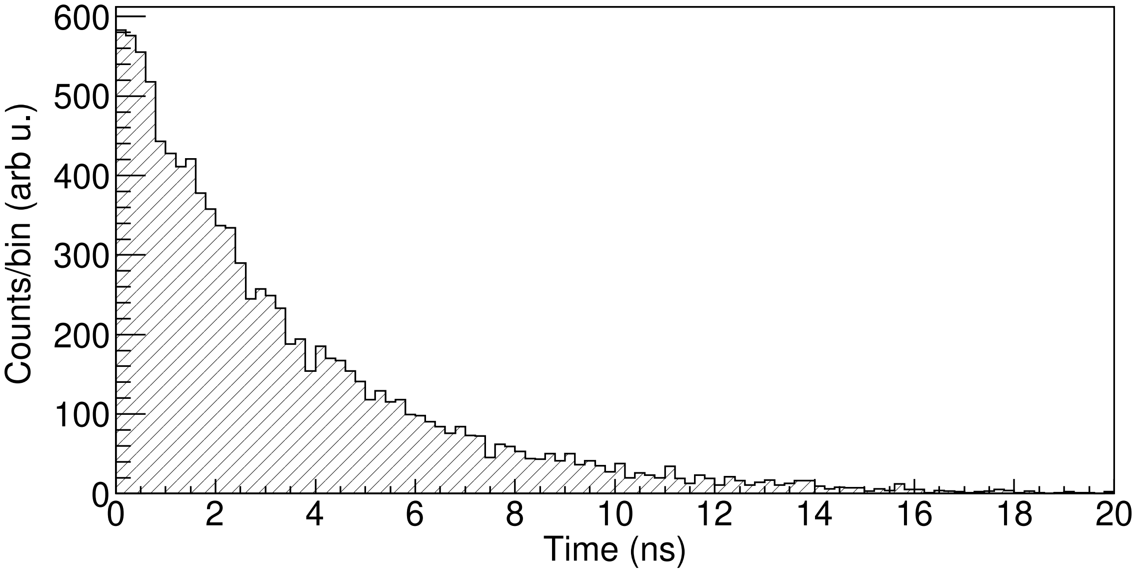

Figure 4.1: The time of flight for a single neutron between two scattering events, where the scatterings happen in different crystals. The total neutrons simulated are arbitrary, the ratio between different bins should be recognized.

Sole reliance on double-scattering events would reduce the efficiency of the detector substantially, but utilization in conjunction with single-scattering events can be used in the future. For this reason, the neutron detector is optimized for single-scattering events. Due to the high segmentation of the array, it is possible to utilize the scattering density in each of the individual crystals to detect and localize a source, especially if multiple arrays are utilized. Crystals closest to the source will show a much larger density of scatterings than crystals further from the source due to attenuation in the detector itself. This effect is the key to the identification and localization of a source. Figure 4.2 shows this effect for a ^{235}U +n source located 100 cm away from the apparatus as well as an ambient neutron background distribution over the entirety of the apparatus.

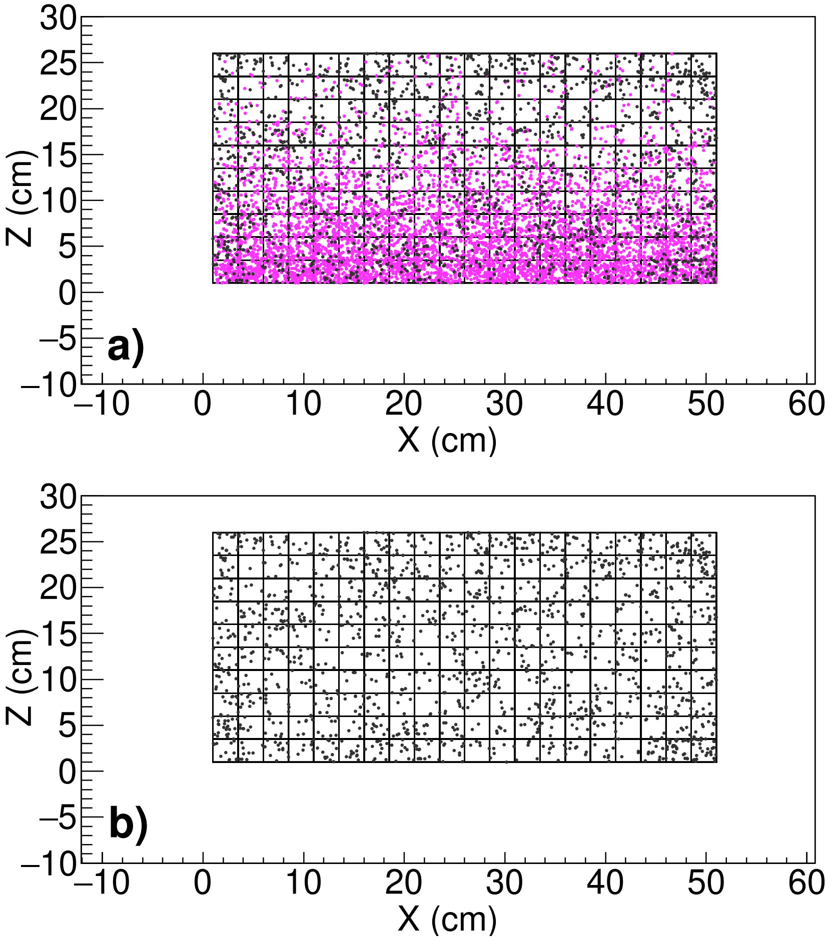

Figure 4.2: Scatterings of neutrons inside of the detector projected on the x-z plane. a) Neutron scatterings are represented as dots due to both source neutrons (gray or magenta online) and ambient background neutrons (black). The ^{235}U +n neutron source is located in the middle of the detector on the x and y axes and at -100cm on the z-axis. b) The black dots are solely from ambient background neutrons.

Due to the chosen depth being approximately two mean free paths for a 1 MeV neutron, source neutrons primarily scatter within the first half of the detector apparatus. Depending on the location of the source the scattering density on the three-dimensional detector array can give localization information on the source in three dimensions as well. Since the ambient neutron background has a homogeneous distribution around the detector apparatus, it is easy to identify an increase in scattering events from the source. Normalization of the ambient neutron background can be well characterized by periodic sampling in each crystal. Comparisons between the scattering rate in the front half of the detector and the back half of the detector can occur in real-time. Figure 4.3 shows the layer dependence of the background and a present ^{235}U +n source. Since the background is homogeneous it gives a parabolic-like shape to the distribution. This is because the interior of the detector array is less likely to see scatterings from the lower energy neutron background. When a neutron source is applied on top of the ambient neutron background then it is easy to identify the source as well as the direction that the neutrons are originating from.

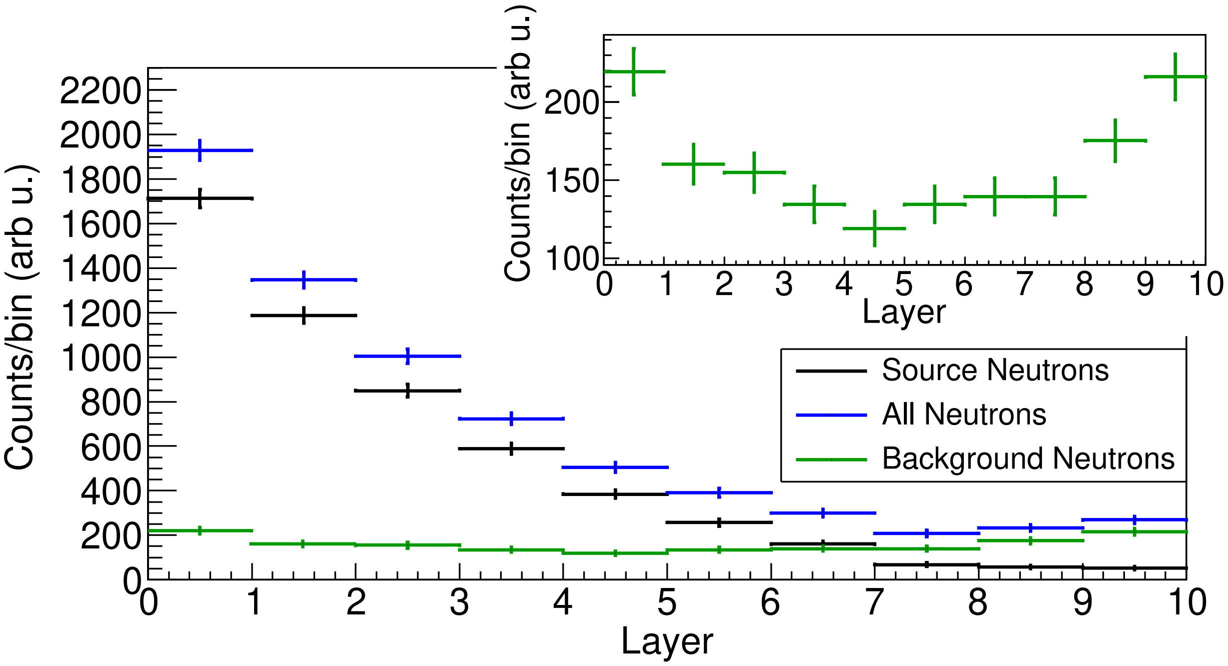

Figure 4.3: Histogram showing the difference between source neutrons and background neutrons from figure 4.2(a) and comparing them to the total neutron count per layer of the detector. The source is positioned closest to layer 0 and furthest from layer 9. The inset plot is a zoomed-in view of the background neutron counts with respect to the layer. The zoomed-in version clearly displays the relatively parabolic shape of the background, which is expected.

4.1 Uniformly Most Powerful Bayesian Tests

The Uniformly most powerful Bayes tests (UMPBTs) [50] were used to determine positive identification of a source. The UMPBTs are derived by assuming that the counts observed in a crystal in the arbitrary coordinate location of (i, j), denoted as y_{ij}, can be described as a Poisson distribution of the form

$$y_{ij} \sim Pois(g(j)\lambda\Delta t) \tag{4.1}$$

with λ being an unknown source intensity, $g(j)$ the average fraction of neutron scatterings per crystal j relative to the ambient neutron background, and Δt the real-world time the simulation encompasses. Naturally, the sum of all $g(j)$ is less than unity ($\Sigma g(j) = 0.244$) and specific values depend on the location of the crystal in the detector. In the real-life settings, these numbers can be directly measured periodically when there is no sample and corrected automatically (if necessary) in real-time. There are then two scenarios that this distribution describes. The first, when λ=λ_0, which is equal to the background intensity. The second, when λ=$\lambda_1 \neq \lambda_0$, or the unknown intensity λ surpasses the ambient background neutron rate of λ_0. In order to determine the minimum unknown λ_1, the UMPBT(γ) methodology is then used. γ, which denotes the evidence threshold, is set such that the Bayes Factor must exceed the chosen γ to provide a positive identification ($BF_{10} > \gamma$). For the purpose of the simulations, γ is set to 10^6, which means that the ratio of likelihoods evaluated at λ_1 and λ_0 is required to exceed 10^6 for detection. The likelihood for some λ can be expressed as

$$L = \prod_{ij} \frac{e^{-g(j)\lambda\Delta t}(g(j)\lambda\Delta t)^{y_{ij}}}{y_{ij}!} \tag{4.2}$$

which is the product sum of the probability mass function. Therefore, the ratio of the likelihoods can then be described as

$$BF_{10} = \prod_{ij} \frac{\frac{e^{-g(j)\lambda_1\Delta t}(g(j)\lambda_1\Delta t)^{y_{ij}}}{y_{ij}!}}{\frac{e^{-g(j)\lambda_0\Delta t}(g(j)\lambda_0\Delta t)^{y_{ij}}}{y_{ij}!}} \tag{4.3}$$

or,

$$BF_{10} = \prod_{ij} e^{-g(j)(\lambda_1-\lambda_0)\Delta t}\left(\frac{\lambda_1}{\lambda_0}\right)^{y_{ij}} \tag{4.4}$$

Then the evidence threshold can be compared to the Bayes factor

$$BF_g > \gamma \rightarrow log\big(BF_{10}(g)\big) > log(\gamma) \tag{4.5}$$

which is can be expanded to

$$\sum_{ij} -g(j)(\lambda_1 - \lambda_0)\Delta t + \sum_{ij} y_{ij} ln\left(\frac{\lambda_1}{\lambda_0}\right) > log(\gamma) \tag{4.6}$$

This can further be simplified to the form

$$\sum_{ij} y_{ij} > \frac{ln(\gamma) + \sum_j g(j)(\lambda_1 - \lambda_0)\Delta t}{ln(\frac{\lambda_1}{\lambda_0})} = f(\lambda_1). \tag{4.7}$$

If a positive identification requires that the Bayes factor for a test exceeds the given γ, then maximizing the probability of a positive identification can be accomplished by assuming the rate through the detector λ_1 [n/s], which is chosen to maximize f(λ_1), or the RHS of equation 4.7. For the purpose of the following calculations, $g(j)$ was averaged over 50 simulations of the ambient neutron background, with 10 million events each. The distribution of the number of counts in each crystal was fit with a Poisson function, providing the average, which was then normalized to the total ambient neutron flux. The function f(λ_1) is minimized with respect to λ_1 for a fixed time (Δt). This would give the minimum source intensity for which identification can be made at the required significance (γ) within a fixed time interval. Conversely, one can determine the minimum amount of time required to identify a source with a given intensity at the required level of significance. The limit is set by equation 4.7, where the sum of events in the detector as a whole, $\sum y_{ij}$, must be greater than f(λ_1). The limit occurs at the point where $\sum y_{ij}$=f(λ_1), inferring that a source can be detected if it emits enough neutrons to satisfy equation 4.7.

The minimization of f(λ_1) is done by varying the value of λ_1 down to just before the limit is reached. When f(λ_1) and λ_1 are plotted against each other, it is clear where the minimum lies for the chosen Δt (Figure 4.4). As expected, the trend is asymptotic at λ_1=λ_0.

Since the UMPBT method gives the number of source neutrons interacting with the detector, the total source neutron rate can be derived if the geometric efficiency is taken into account. The estimated number of source neutrons emitted per second is simply

$$I_{src,det} = (\lambda_1 - \lambda_0), \tag{4.8}$$

$$I_{src} = I_{src,det} \times \frac{4\pi}{\Omega_{sim}}, \tag{4.9}$$

with I$_{src,det}$ being the number of source neutrons detected per second. The intrinsic efficiency of

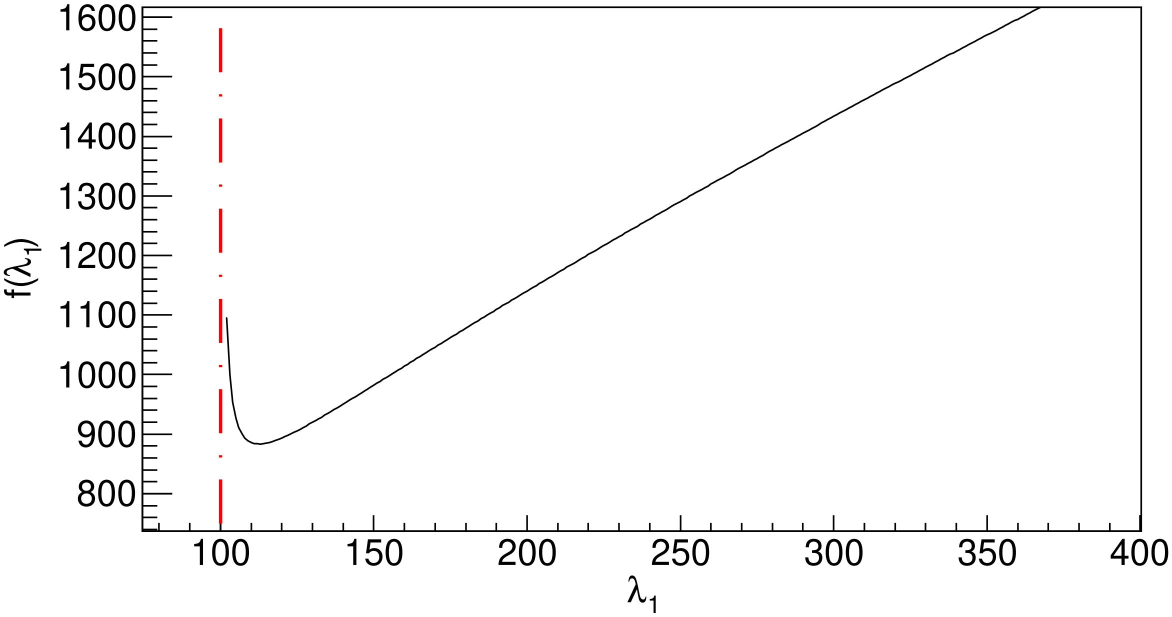

Figure 4.4: Minimization of f(λ_1) (equation 4.7) with respect to λ_1, with Δt=32.13 seconds. The dashed line represents the location of λ_0. The trend of f(λ_1) is asymptotic as it approaches λ_1=λ_0 and is approximately linear as it increases to infinity.

the detector is given by:

$$\epsilon_{sim} = \frac{N_{det,sim}}{N_{tot,sim}} \times \frac{4\pi}{\Omega_{sim}}, \tag{4.10}$$

where $N_{det,sim}$ is the number of neutrons from the source that produce a signal above the threshold in the detector, $N_{tot,sim}$ is the total number of source neutrons in the simulation, and Ω_{sim} is the solid angle encompassed by the detector with respect to the point source in the simulation. The intrinsic efficiency is a function of the energy threshold, which is set to the PSD threshold of *p-terphenyl* to have clean neutron identification.

The time it takes for the detector to identify the source can also be calculated using

$$t = \frac{f(\lambda_1)/\epsilon_{sim}}{I_{src} \times \frac{\Omega}{4\pi}}, \tag{4.11}$$

where Ω is the solid angle from the source position being calculated. The identification time scales with the solid angle and detector efficiency.

5. SIMULATED DETECTOR PROPERTIES

5.1 Comparison to Industry Standards

The standards for radiation portal monitors are set by the National Committee on Radiation Instrumentation (NCRI). In a Pacific Northwest National Laboratory (PNNL) study (Kouzes *et al.*) in 2010, the requirements for a neutron portal monitor are described [16]. The requirements are set with a ^{252}Cf spontaneous fission source placed 2 m away from the detector. It is important to identify a notable conversion, 1 ng of ^{252}Cf corresponds to a neutron rate of 2.1x10^3 n/s. The efficiency requirement set by these standards is 2.5 cps/ng (counts per second per nanogram). The ^{252}Cf source is also required to be moderated by polyethylene with a thickness of 2.5 cm, which is unnecessary for a fast-neutron detector but is required for a ^{3}He detector to moderate the neutron to allow for detection. In the MCNP6 simulations, the ^{252}Cf source emitted a total of 950,000 neutrons over a span of 1.388 seconds. This corresponds to a source mass of 326 ng.

In order to create a comparable scenario between the proposed neutron detector and a current-generation ^{3}He detector, both were simulated in MCNP6 using the same moderation and generic parameters such as distance from the source. The ^{3}He detector simulated is the one described in Kouzes *et al.* [16]. The specific geometry was replicated according to previous MCNP simulations for the detector, described in [28]. A single ^{3}He tube, with a gas pressure of 3 atm, was simulated. The simulations yielded a rate of 597 n/s being detected. This neutron rate corresponds to an efficiency of 1.83 cps/ng. This differs from the quoted 3.0 cps/ng and the discrepancy is likely due to the undefined polyethylene thickness of the real ^{3}He detector.

The same simulation was done with the proposed detector in place of the ^{3}He detector. The simulation yielded a detected neutron rate of 3203.22 n/s after the 2.5 cm thick polyethylene moderator. It should again be noted that the polyethylene is unnecessary for the function of the fast-neutron detector but was included in order to comply with the standards set by the NCRI. The detected neutron rate of 3203.22 n/s corresponds to an efficiency of 9.83 cps/ng. However, this efficiency should be corrected for the size difference of the two compared detectors. Normalization was done by taking the ratio of the two detector volumes, the same method used to scale the efficiencies in Kouzes *et al.* [16]. It should be noted that this method only provides an estimate for the scaling of the efficiency. The total volume of the ^{3}He detector is 170,190 cm^3 (183 cm x 15 cm x 62 cm) [28]. The total volume of the proposed detector is 62,500 cm^3. This leads to a scaled efficiency of the proposed detector of 26.8 cps/ng that is directly comparable to the current generation portal monitors. Table 5.1 shows the comparison of the calculated efficiency of the proposed detector to commercially-available detectors tested in Kouzes *et al.* [16].

Detector Type	Efficiency (cps/ng)
Proposed Detector	26.8
^{3}He proportional detector (1 Tube)	3.0(2)†
BF$_3$ proportional detector (3 tubes)	3.7(2)†
Boron-lined proportional detector	3.0(2)†
Lithium-loaded glass fibers	1.7(6)†
Coated non-scintillating plastic fibers	2.0(1)†

Table 5.1: Comparison of neutron detection efficiency of the proposed detector and commercially-available detectors studied in Kouzes *et al.* [16]. Values marked with a † were taken from Kouzes *et al.*

The above comparison takes the proposed detector as a counting detector and neglects the benefits from using the UMPBT statistical model. In order to make the comparison to the statistical model, positive detection confidence levels were calculated for a ^{252}Cf source (rate of 3112 n/s) located 2 m from the detector for various exposure times. A series of 50 MCNP6 simulations were performed for the ^{3}He detector for each of the chosen times with both a source and no source present. A Poisson average was taken for the sets of simulations to get the average number of neutrons detected from the source, C_{src}, and from the background, C_{BG}. For each exposure time, the error on the background was calculated as

$$\epsilon = \sqrt{C_{BG}}. \tag{5.1}$$

With ϵ, the confidence interval was calculated with

$$x = \frac{C_{Total} - C_{BG}}{\epsilon}, \tag{5.2}$$

with C_{Total} being the sum of C_{src} and C_{BG}. The confidence interval was then used to calculate the confidence level in the form 1 in γ, with

$$\gamma = \frac{1}{1 - Erf(\frac{x}{\sqrt{2}})}. \tag{5.3}$$

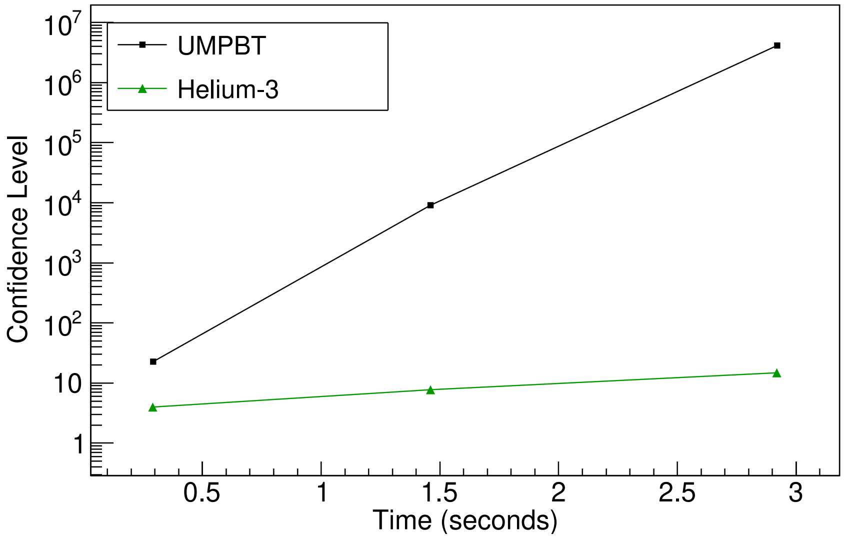

Figure 5.1: Confidence levels γ (i.e. γ=10^6 corresponds to a confidence level of 1 in 10^6) calculated for a ^{3}He detector (triangles and green online) and the proposed detector (squares and black) using the UMPBT model. The confidence levels were derived from sets of 50 MCNP simulations with and without a source present. The confidence levels show a sensitivity comparison of the proposed detector to a standard ^{3}He detector.

The confidence levels were also calculated for the proposed detector using the same data and equation 4.7. Figure 5.1 shows the two sets of confidence levels plotted against each other for the various times chosen. This plot shows the sensitivity advantage that comes from using the UMPBT model with the proposed detector over the current-generation ^{3}He detectors.

5.2 Active Interrogation Technique

One of the major obstacles of SNM detection, specifically HEU, is the low rate of spontaneous fission (7x10^{-9}% for ^{235}U and 5.7x10^{-6}% for ^{239}Pu [51]). Current generation thermal neutron detectors for portal monitoring are not sensitive to HEU due to the incredibly low spontaneous fission rate. Since the proposed detector is using fast neutrons to detect the presence of fissile materials, it becomes possible to use a beam of low-energy ($E_n < 1$ MeV) neutrons from a neutron generator, often referred to as active interrogation. One example of a neutron generator uses the ^{7}Li(p,n)^{7}Be reaction to produce a low-dose beam of 60 keV neutrons at a rate of approximately $5x10^6$ neutrons/s [36]. This particular neutron generator has good efficacy through non-hydrogenous shieldings such as steel and plywood but can struggle with hydrogen-rich shielding. Using ^{235}U as an example, it is possible to use the UMPBT model to estimate the minimum time required to detect a neutron source of a particular intensity. The dependence on time (t, equation 4.11) and the number of neutrons entering the detector array ($I_{src,det}$, equation 4.8) can be visualized by plotting them against one another (Figure 5.2). This provides a sensitivity limitation trend for the detector. Table 5.2 shows a variety of different scenarios and the time it would take the proposed detector to identify the source.

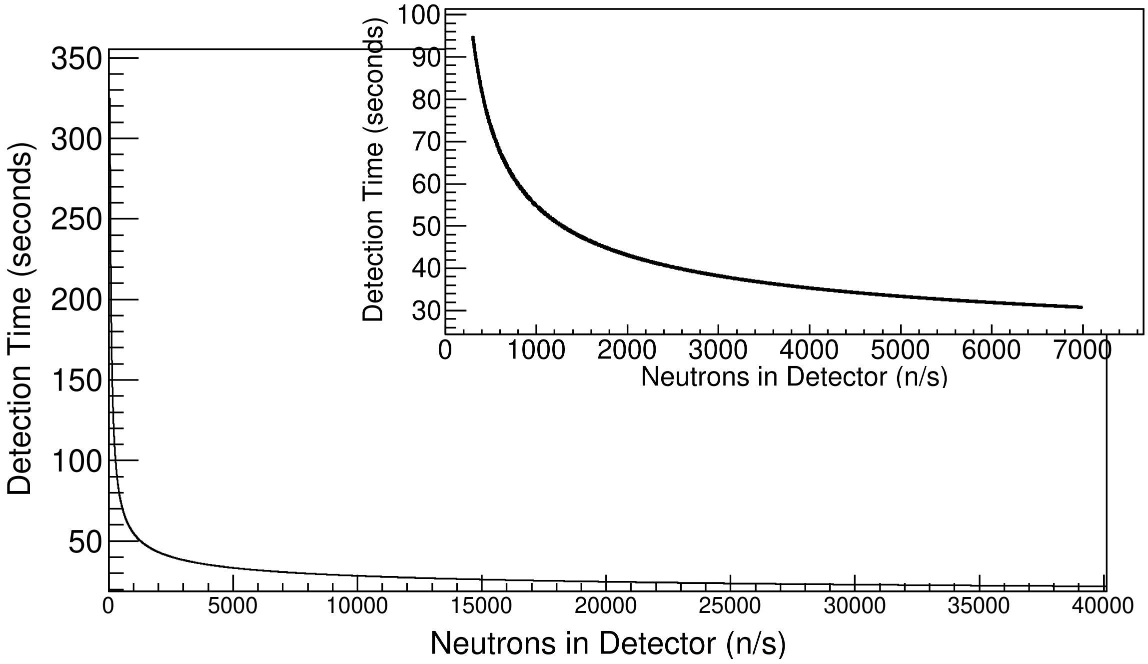

Figure 5.2: Detection time vs source-neutron intensity entering the detector. The overlaid plot is a zoomed-in portion of the main plot to highlight the low-intensity region. The confidence level used is γ=10^6.

It is also possible to convert the source intensities to masses of the SNM. For example, the conversion between mass and spontaneous fission rate for ^{252}Cf is known, as described in section 5.1. In order to do the conversion for ^{235}U, we assume the neutron flux for the 60 keV neutron generator to be $\phi = 5 \times 10^6$ cm $^{-2}$ s^{-1}, as stated in Ref. [36]. The fission cross section, $\sigma \approx 2$ barns [52] at 60 keV, and the prompt neutron multiplicity, $\nu_p = 2.42$ [52], of the $^{235}\mathrm{U} + n$ reaction were used. Using equation 5.4, Avagadro's number, N_A, and the mass $M_{^{235}U} = 235$ g, the conversion was performed to estimate the mass for a range of source neutron intensities (Table 5.3). A similar plot to figure 5.2 was then made with respect to mass (Figure 5.3).

$$M = \frac{I_{src}}{\nu_p N_A \sigma \phi} M_{^{235}U} \tag{5.4}$$

Source Distance (m)	$I_{src,det}$ (n/s)	I_{src} (n/s)	Time (sec)
1	1	50.3	16703
	10	502.7	1477
	100	5027	192
	200	10053	120
	800	40212	60
2	50	10053	331
	200	40212	120
3	22	9953	686
	89	40263	209
5	8	10053	1851
	32	40212	487
10	2	10053	7966
	8	40212	1851

Table 5.2: ^{235}U +n neutron source intensity vs the time needed to identify the source at various distances. The source is centered on the face of the detector, and the distance is the distance of the source relative to the detector. The time was found using the UMPBT statistical model and represents the minimum time, with the assumptions previously stated, that it would take to positively identify a neutron source. The confidence level used is γ=10^6.

$I_{src,det}$ $x10^3$ (n/s)	Mass (g)	Time (sec)
0.01	0.0081	1477
0.1	0.0807	192
0.2	0.161	120
0.8	0.646	59.8
1.5	1.21	47.4
2	1.61	43.1
3	2.42	38.2
4	3.23	35.3
5	4.03	33.4
10	8.07	28.4
25	20.2	23.7

Table 5.3: Source-neutron intensity entering the detector, with a source distance of one meter, and the mass conversion for ^{235}U . The detection time found for the various masses at one meter from the detector is also displayed. The confidence level used is γ=10^6.

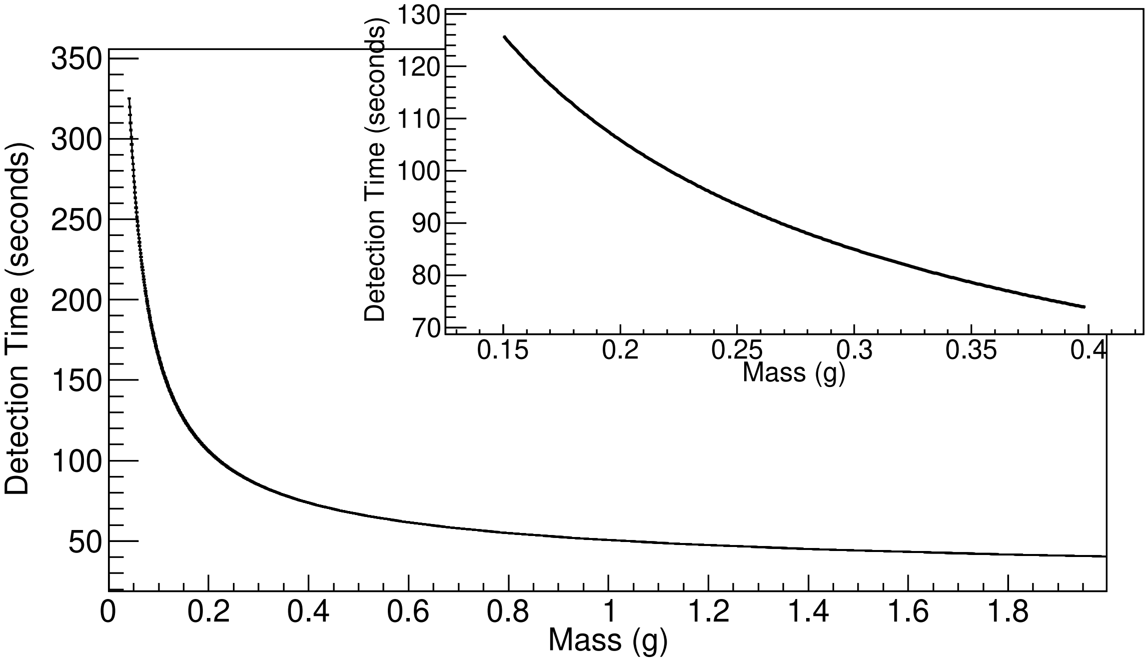

Figure 5.3: Similar to figure 5.2, but in terms of the mass of ^{235}U instead of source-neutron intensity. The overlaid plot is a zoomed-in portion of the main plot to highlight the low mass region. The confidence level used is γ=10^6.

6. CONCLUSION

The current-generation neutron portal monitors generally rely on ^{3}He and neutron thermalization. ^{3}He has a finite terrestrial supply with only the United States and Russia producing the isotope. However, the production rate is negligible compared to the demand throughout the world. As a result, the terrestrial supply is decreasing rapidly and the prices have skyrocketed, driving an effort for next-generation neutron detectors that can replace ^{3}He dependent detectors. Neutron thermalization is also a disadvantage to the current-generation neutron portal monitors. Neutron thermalization makes it impossible to use active interrogation techniques which makes it nearly impossible to detect non-spontaneous fissioning SNMs such as HEU. Neutron thermalization relies on counting as the main detection method which doesn't allow for source localization.

The analysis discussed provides an answer to the call for next-generation neutron portal monitors. The proposed detector vastly outperforms current-generation neutron portal monitors with and without active interrogation, as well as with or without the use of the UMPBT statistical model. Using MCNP6 simulations the limitations for the detector array were studied. Without moderation, any fissile source one meter from the detector, emitting $\sim$500 n/s, isotropically, can be positively identified in just under 25 minutes. Similarly, a source emitting $\sim$5000 n/s can be detected in about 192 seconds. For the case of ^{235}U, these neutron emission rates correspond to approximately 8.1 mg and 80.7 mg, respectively assuming the use of the active interrogation technique described in the previous section.

Using the standards set by the National Committee on Radiation Instrumentation (NCRI), the proposed detector was directly compared to current-generation neutron portal monitors described in Kouzes *et al.* [16]. These comparisons were discussed in table 5.1. The limitations set by the NCRI resulted in a minimum required detector efficiency of 2.5 cps/ng (counts per second per nanogram). The proposed detector surpasses both the requirements set by the NCRI as well as the performance of current-generation neutron portal monitors. The proposed detector boasts an efficiency of 26.8 cps/ng, after taking into account inflation due to the differences in the volumes of the detectors in the comparison. The efficiency calculated was without the utilization of the UMPBT statistical model, taking the detector array as a single counting detector rather than utilizing the modularity of the array. Since the efficiency is not affected by the use of the model a straight comparison with the UMPBT model and the current-generation portal monitors would not yield a different result as described above. Instead, a comparison of confidence levels was made in order to determine the effectiveness of the statistical model. As shown in figure 5.1, the UMPBT model provides a sensitivity advantage over the counting techniques, particularly the ^{3}He detector.

The times probed scale linearly with the solid angle of the detector with respect to the source. Ideally, an array of multiple detectors can be used in various positions to further increase the detection and identification efficiencies found. Multiple detectors will also reduce the time needed to positively identify a source and increase the sensitivity of the setup.

The MCNP6 simulations, along with the abundance of analyses done, provides a strong basis for the development of the next-generation neutron portal monitor described. Utilizing advancements such as the development of the *pseudo-bar* [42] allows for a compact detector array with optimal position and energy resolutions. The eventual construction and testing of a full-scale detector array will hopefully perform similarly to what the simulations have revealed, providing the community with an answer to the call for non-^{3}He next-generation neutron portal monitors. This work has been compiled into a manuscript that has been published in the *Nuclear Science and Techniques* journal.

II THE DEVELOPMENT OF THE TEXAS CsI ARRAY FOR ASTROPHYSICAL MEASUREMENTS (TexCAAM)

7. ORIGIN OF ELEMENTS

It is widely accepted that the Big Bang theory describes the origin of the universe. This theory was proposed by Georges Lemaître after his 1927 work on the continual expansion of the universe [53]. The synthesis of elements occurred during and shortly after the birth of the universe, as discussed by Peebles [54] in 1966. Through big-bang nucleosynthesis, the composition of the beginning of the universe was nearly 100% helium and hydrogen along with infinitesimal amounts of lithium and beryllium [55].

Shortly after the discovery of the mass of a helium atom in 1920, Atkinson (1936) proposed the fusion of two hydrogen nuclei into deuterium [56]. In 1938 Bethe and Critchfield showed that the fusion of deuterium (p+p reaction) produces energy similar to that produced in the Sun [57]. In the same year Weizsacker discovered that the CNO cycle produces similar energy to that of other stars [58]. Hoyle in 1946 and later in 1954 proposed the theory of nucleosynthesis [59, 60]. In 1952 Salpeter suggested that ^{12}C could be produced in stellar environments through the ^{8}Be+α capture reaction, or commonly known as the triple-α process [61].

The birth of modern nuclear astrophysics occurred in 1957 with the publication of *Synthesis of Elements in Stars* [62] and *Nuclear Reactions in Stars and Nucleogenesis*[63]. These works explained the energy generation in stars and the origin of elements through nucleosynthesis.

7.1 Stellar Evolution

The formation of stars begins with interstellar matter, which comprises of elemental gases and *dust*, pre-stellar metallic grains formed in prior nucleosynthetic events. The interstellar matter undergoes gravitational contraction, forming a spherical molecular cloud. As it collapses, the density increases and so does the temperature. The density of this molecular cloud is heterogeneous, with the core being significantly denser. The core releases energy which is absorbed by the gaseous envelope surrounding it and radiated away as infrared light. During the gravitational contraction, the core of the star will steadily increase in temperature, eventually becoming hot enough to overcome the Coulomb repulsion and fuse hydrogen [4, 17].

During the formation of stars, their fate is determined. Stars can be plotted on the Hertzsprung-Russell diagram, which is a luminosity vs temperature plot of known stars (Figure 7.1). Their position on the Hertzsprung-Russell diagram is primarily determined by the mass of the star. The vast majority of stars lie along the main sequence branch where they undergo hydrogen-burning through the proton-proton (pp) chain and the Carbon-Nitrogen-Oxygen (CNO) cycle. As main sequence stars run out of fuel for hydrogen burning, most (including the sun) will become red giants (RGB), shedding their layers. The core contracts as the pressure from the nuclear reactions subside, increasing the temperature of the star dramatically. The star will then start its helium-burning phase producing carbon and oxygen. A thermonuclear runaway will occur due to the cyclic fusion of these elements and the star undergoes a core helium flash, expanding the core and subsequently expanding the hydrogen-burning shell, entering the horizontal branch. The core will collapse creating two discrete burning regions, the core burning helium and the shell burning hydrogen, that are separated by helium. The core will continue to undergo thermonuclear runaway and pulsing. This will heat the shell and hydrogen burning in the shell will once again be the primary energy source of the star. The hydrogen layer of the star will get ejected and once the star's surface gets hot enough, it will radiate ultraviolet light which will ionize the ejecting layer, now referred to as planetary nebula. The remaining core is called the planetary nebula nucleus, eventually becoming inert, becoming much less luminous, and transitioning into a white dwarf [17].

With respect to the solar mass, $M_\odot$, the star types, initial branches, and initial stages are listed for various masses of stars in table 7.1. The initial stage of most stars is hydrogen burning, however it is segmented into two regimes: stars with masses less than 1.5 $M_\odot$ and stars with greater masses than 1.5 $M_\odot$. In the first regime, the stars start with the pp chain and in the second the stars can go straight into the CNO cycle.

Mass ($M_\odot$)	Star Type	Initial Branch	Initial Stage
0.013-0.08	Brown Dwarf	–	–
0.08-0.4	Red Dwarf	Main Sequence	Hydrogen Burning (pp)
0.4-1.5	Low Mass Star	Main Sequence	Hydrogen Burning (pp)
1.5-2	Low Mass Star	Main Sequence	Hydrogen Burning (CNO)
2-11	Intermediate Mass Star	Main Sequence	Hydrogen Burning (CNO)
11-100	Massive Star	Main Sequence	Hydrogen Burning (CNO)

Table 7.1: A table of the evolution of stars. This table is adapted from one found in [17].

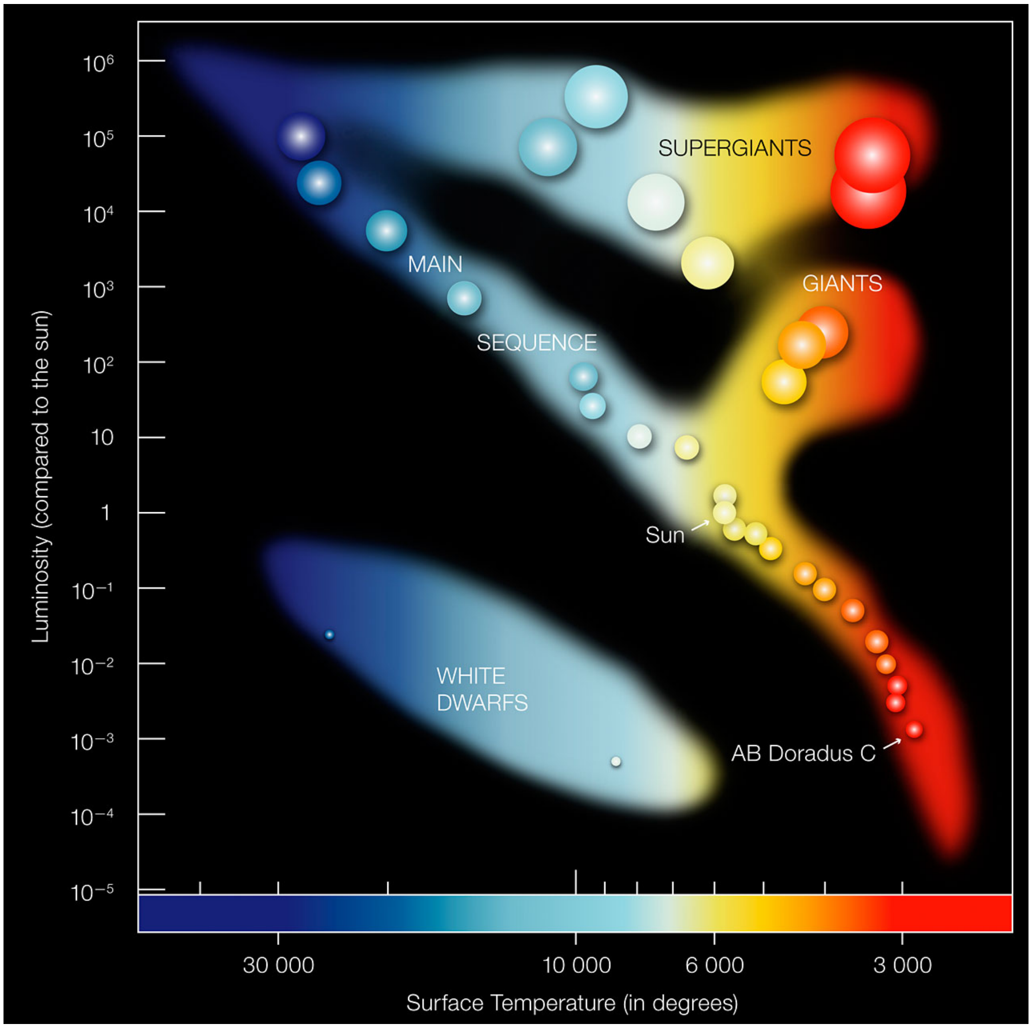

Figure 7.1: Hertzsprung-Russell diagram showing the evolution of stars. The central band, or the main sequence band, is where stars live during their pp chain and CNO cycle stages. (via European Southern Observatory (ESO) /eso.org)

7.1.1 Stellar Populations and The First Stars

Stellar populations were first proposed in 1944 by W. Baade [64]. In a detailed analysis of stars in the Andromeda galaxy, two stellar populations were identified: population-I (pop-I) and pop-II. Pop-I stars were grouped as highly luminous O- and B-type stars and those in open clusters, or those that are characteristic of the spiral arm. Pop-II stars were grouped as short-period Cepheids[1] and globular clusters, or those characteristic of the spaces between the spiral arms.

More commonly, observed stars are categorized in the two populations where pop-I stars are the youngest most metal-rich stars in the universe and pop-II stars are the oldest observed and are metal-poor [2]. In the Hertzsprung-Russell diagram most are pop-I stars with only a few being pop-II stars [65].

7.1.1.1 Population-III Stars

While observed stars are segregated into the two stellar populations, a theoretical pop-III stellar grouping exists [66]. Pop-III stars are the first stellar formations after the Big Bang. Having only a composition of hydrogen and helium, these stars are called zero-metal stars. Pop-III stars are the key to the transition from a hydrogen/helium-dominated universe to the very complex, metal-rich universe that we observe today.

In the early part of the universe, in the Cosmic Dark Ages, the universe consisted of gaseous hydrogen and helium clouds. Gravitational clustering of the gaseous clouds formed proto-galaxies. Gravitation contraction, Jeans instability [67], began the formation of the first stars, but gravitational contraction alone would be too strong to create the hydrostatic equilibrium required to form stars. Thermal energy is believed to be radiated during this contraction through the production of H_2 through charge exchange reactions [68].

Through numerical fragmentation of primordial gas clouds and numerical simulations, pop-III stars are believed to be mainly very massive ($M \geq 100\ M_\odot$) and have very short lifetimes, which

---

[1] Cepheid [variable]: A radial-pulsating star with a well-defined period of luminosity variation. Cepheid stars evolved off of the main sequence into the ‘Cepheid instability strip’

[2] As this is astronomy, anything more massive than helium is considered a metal.

were on the scale of a million years [69]. However, very low-mass low-metallicity stars have been observed. One, in particular, was found in 2002 with a metallicity of [Fe/H]=-5.3 and a mass of 0.8 $M_\odot$ [70]. It is theorized that low-mass low-metallicity stars could undergo a similar formation process through cooling of deuterium hydride instead of H_2 [71].

It is believed that supernovae of pop-III stars are the cause of the initial metal enrichment in the intergalactic medium [69]. In massive zero-metal stars, pair-instability supernovae (PISN) may also occur. PISN occurs when the internal pressure is disrupted by collisions of pair-produced electrons and positrons and atomic nuclei. The internal pressure may decrease significantly enough to cause a gravitational collapse [72]. An interesting consequence of PISN is the possibility of the core being destroyed, leaving no remnant [73].

The age of pop-III stars ended due to radiative feedback [69]. Radiative feedback from soft UV photons, from already established stars, could photo-disintegrate the H_2 molecules in the collapsing proto-stellar gas clouds, preventing the clouds from cooling enough for the stars to form. The age of pop-III stars could have also been ended due to the heavy element enrichment from the supernovae. In this case, we would observe a transition from pop-III stars to pop-II stars.

7.2 Nucleosynthesis

Nucleosynthesis falls in one of the two main categories - quiescent and explosive, with further sub-categories, such as stellar nucleosynthesis, supernovae, novae, neutron star collision, black hole accretion disk nucleosynthesis, and cosmic-ray spallation. In the early universe, after Big Bang nucleosynthesis had produced the building blocks of the universe, the formation of the first stars would have opened the possibility for both, quiescent and explosive nucleosynthesis (supernovae and novae). The first stars provided a bridge between the Big Bang and the vastly diverse universe that we observe today.

7.2.1 Big Bang Nucleosynthesis

After the Big Bang, the universe rapidly expanded and cooled. Once the universe reached a temperature $\sim$7.5x10^9K, the neutron to proton ratio stagnated at 1:7. As the universe cooled even further to 1x10^9K deuterons and heavier elements were able to form. As the temperature continued to decrease, T≪1x10^9K, the neutrons, whose lifetimes are finite, either β^- decayed or coupled with protons to form deuterium. The majority of the primordial deuterium became ^{4}He through d(p,γ)^{3}He and ^{3}He(n,γ)^{4}He reactions. Charged particles then stopped forming as the thermal temperature was below that required to overcome the Coulomb barriers [5].

Big Bang nucleosynthesis calculations can predict hydrogen, helium, and lithium abundances shortly after the Big Bang with unprecedented precision [74]. However, isotopic abundances in population II dwarfs and other old metal-poor stars have suggested that the abundance of lithium is greatly lower than predicted (a factor of 2 or 3 lower) [75, 76]. Some have theorized that the cosmological lithium discrepancy is due to diffusion theory, where the lithium diffuses deep into the star creating lithium-free superficial layers [74]. More recent studies of the ^{3}He$(\alpha,\gamma)^7$Be reaction have seen an increase in the reaction rate and have better constrained the uncertainty. Baryon density studies, which have increased the discrepancy further, anticipate a lithium abundance between 2 and 5 times higher than observed [77]. While nuclear astrophysics is not expected to be the cause of the cosmological lithium discrepancy, reactions such as the ^{7}Be$(\alpha,\gamma)^{11}$C reaction have been proposed, and dismissed, to have an impact on the abundance of lithium [78]. Constraining the ^{7}Be$(\alpha,\gamma)^{11}$C reaction rate can further prove its irrelevancy in the cosmological lithium problem.

7.2.2 Stellar Nucleosynthesis

Most main sequence stars undergo two processes during the hydrogen-burning phase of their lifetime. First is the proton-proton chain which starts with the fusion of hydrogen which begins at ∼5x10^6 K [4]. The second is the Carbon-Nitrogen-Oxygen (CNO) cycle, which doesn't begin its hydrogen-burning until ∼15x10^6 K. [4]. The overlapping region, shown in figure 7.2, comes as the temperature rises and sufficient ^{12}C is produced to support the CNO cycle. The ^{12}C abundance in pop-I stars depends on the ^{12}C abundance in the proto-stellar environment. Massive stars with a significant abundance of ^{12}C can reach CNO temperatures during their formation and can bypass the pp-chain (table 7.1).

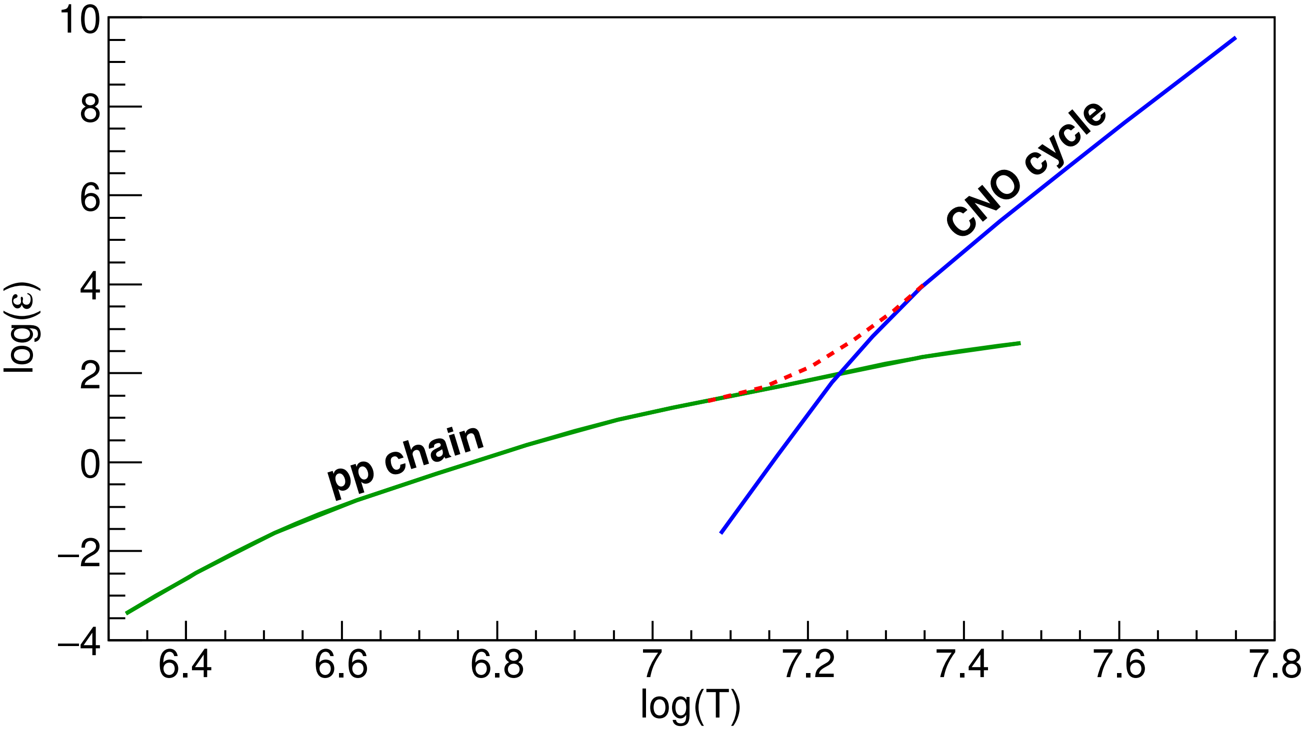

Figure 7.2: The relationship between stellar temperature (T) and relative energy output (ε) for the pp chain (green online) and the CNO cycle (blue online). The shift from the pp chain to the CNO cycle is represented by the red dashed line. As the temperature of the star increases it shifts from the pp chain into the CNO cycle. At the transition point the pp chain will become insignificant to the CNO cycle. This figure was reproduced from the one found in [4].

7.2.2.1 Proton-proton Chain

It is commonly accepted that the pp chain has multiple stages that encompass proton fusion to the production of ^{8}B through proton capture (Figure 7.3). The primary route of the pp chain is proton-proton fusion then immediate β decay into ^{2}H. The ^{2}H then picks up a proton to form ^{3}He. The ^{3}He particles can fuse forming ^{4}He + 2p. The two protons are then free to restart the pp chain. As the abundance of ^{4}He increases, it is more likely to fuse with ^{3}He forming ^{7}Be and later ^{7}Li or ^{8}B, which may capture an α particle to form ^{12}C via the triple-α process.

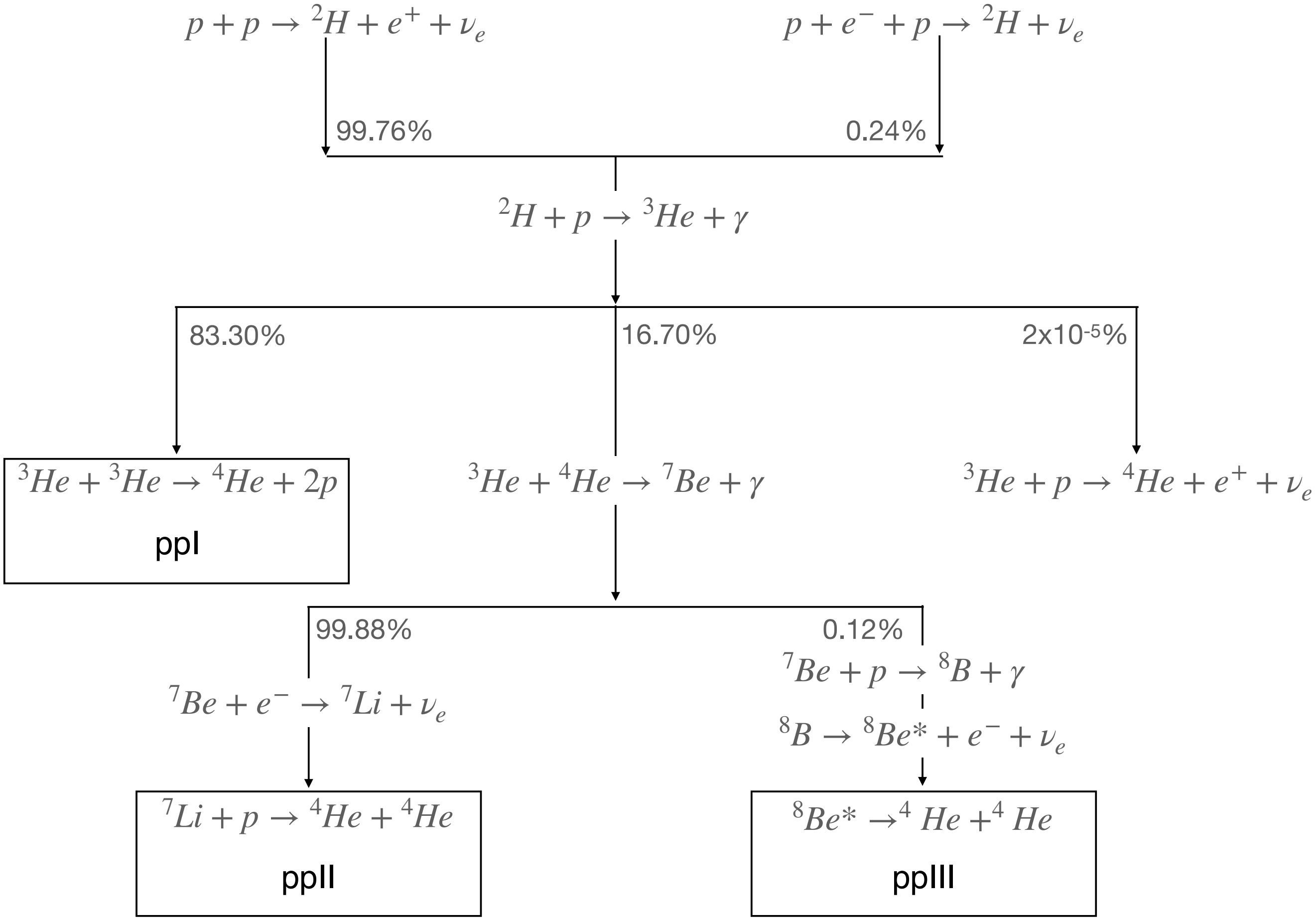

Figure 7.3: The proton-proton chain, which is the primary reaction chain for low-temperature main sequence stars. The chain starts with the fusion of two protons to form deuterium. The deuterium can then fuse with another proton to form ^{3}He. The ^{3}He then feeds the ppI, ppII, and ppIII chains that produce ^{4}He. This diagram is adapted from the one found in [5]

7.2.2.2 Carbon-Nitrogen-Oxygen Cycle

Once enough ^{12}C has been produced in the late reactions of the p-p chain, main sequence stars will kick off the CNO cycle. The CNO cycle consists of a group of reactions that are split into four groups: CNO1, CNO2, CNO3, and CNO4 (Figure 7.4). Each of these groups represents a circular chain of reactions where the final reaction produces the element needed for the initial reaction. The point of these cycles is to produce helium from four hydrogen atoms, producing substantial amounts of energy.

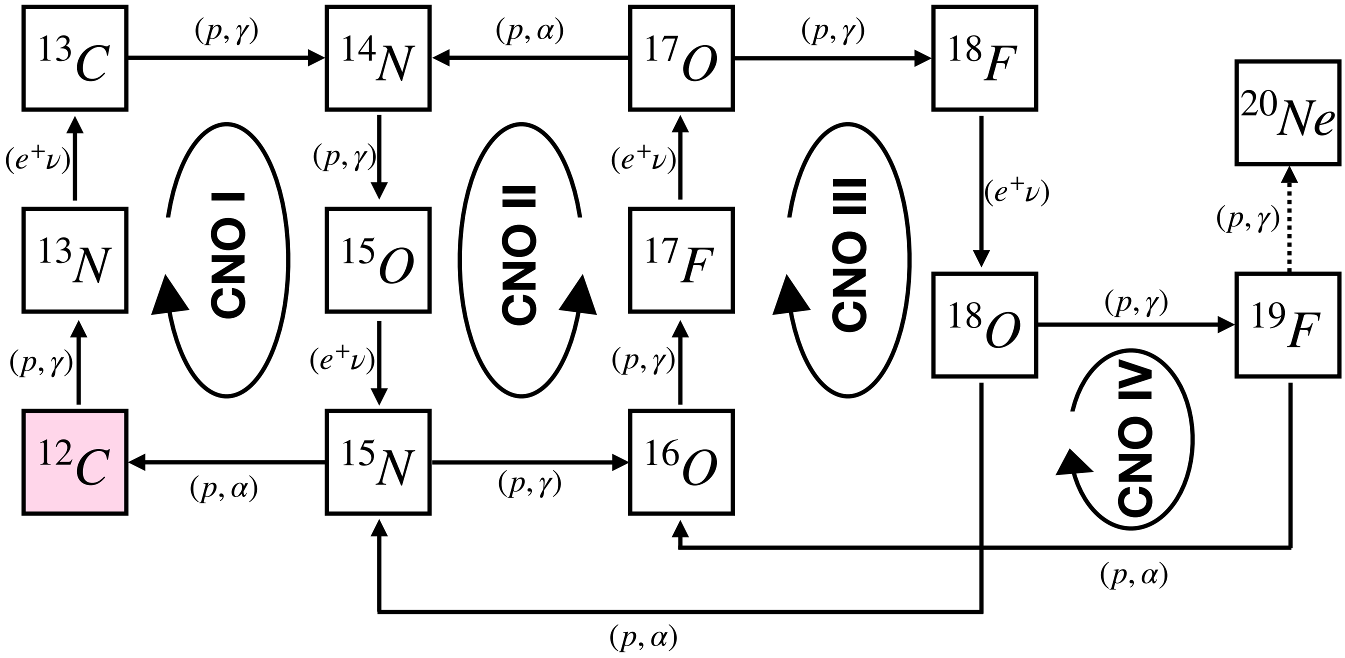

Figure 7.4: The CNO cycle, which picks up after the production of ^{12}C after the proton-proton chain. The gray (pink online) square marks the location of ^{12}C, which is the start of the CNO cycle. The four CNO cycles are shown along with the reactions required to step forward in each of the cycles. The $^{19}F(p,\gamma)^{20}Ne$ reaction is a possible material loss reaction as well as a possible link to the NeNa cycle [5]. This diagram is adapted from the one found in [5].

7.2.3 Alternate ^{12}C Production in Zero-Metal Main Sequence Stars

The formation of ^{12}C is the crucial step to kick off the CNO cycle. The creation of ^{12}C through the triple α process requires temperatures around 10^8K [79]. The triple-α process is primarily temperature dependent, predicting that the time in which it begins depends on the mass of the star. Figure 7.5 shows the temperature and density dependence on the processes that occur in zero metal stars. It describes a distinct transition from the pp chain into the CNO cycle.

For low mass pop-III stars the triple-α process takes place towards the very end of the H-burning phase. For the lowest mass, zero-metallicity stars, M ≤ 0.8 M$_\odot$, the triple-α process may not be able to produce enough ^{12}C before the star inevitably collapses on itself [6].

For massive pop-III stars, in the regime of M ≥ 20 M$_\odot$, the triple-α process may begin before the pp-chain terminates. However, some studies claim that supermassive zero-metal stars will not undergo thermonuclear explosions before they collapse on themselves. Since the triple-α process is such a slow reaction, it may not be able to produce enough CNO nuclei in the very short timeframe before the star collapses [80]. With enough CNO nuclei during the collapse of a supermassive low metallicity star, the hot CNO cycle can prevent the collapse of the star into a black hole.

Without the crutch of pre-stellar metals, the triple-α process cannot solely prevent the collapse of some of the first generation stars. There may be an alternative to the triple-α process that can produce ^{12}C in pop-III stars. R. Mitalas in 1985 [81] suggested an extension to the pp chain which is now commonly known as the hot-pp chain. It was hypothesized that minor constituents of the pp chain could react to create ^{12}C through two primary chains:

^{7}Be(α,γ)^{11}C(p,γ)^{12}N(β^{+},ν)^{12}C

^{11}B(p,γ)^{12}C

With the theoretical calculations presented in R. Wagoner [82], they found that the reaction rates for these processes were small, and if there aren't high densities, the alternate ^{12}C production methods were insignificant. The reaction rate data published by Harris *et al.* [83] did slightly increase the calculated abundance of ^{11}C in the system resulting in a similar shift in the ^{12}C abundance. The conclusion of this study was that high densities were needed in pop-III stars in order for an alternative ^{12}C production method to be significant against the triple-α process.

In 1989, Wiescher *et al.* [7] performed a study on hot pp chains. Now, instead of a direct chain

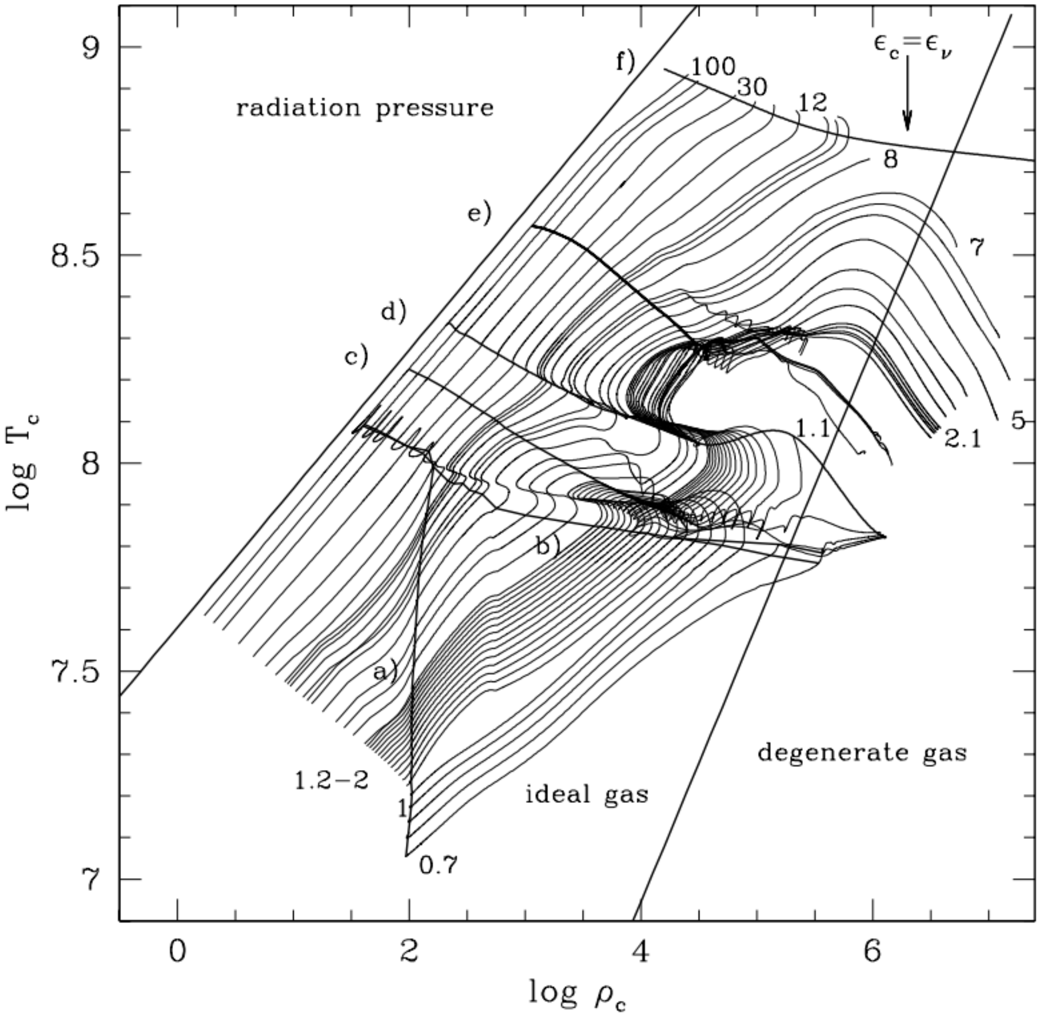

Figure 7.5: Temperature vs density plot for zero-metal stars. The lines represent: (a) onset of central H-burning, (b) onset of 3-α and hence start of the CNO-cycle, (c) end of core H-burning, (d) onset of central He-burning, (e) end of core He-burning, (f) energy balance between carbon burning and neutrino losses [6]. P. Marigo *et al.*, A&A, 371, 152, 2001, reproduced with permission ©ESO.

to produce ^{12}C to kick off the CNO cycle, the paper looks at processes that link the pp chain and the rapid proton capture (rp) process or alpha capture process to circumvent the triple-α process. These reaction chains are named the rap-processes and shown in Table 7.2. Figure 7.6 shows a density vs temperature plot that shows where the rap-processes lie. The new processes, that are proposed in Wiescher *et al.*, provide an alternate ^{12}C production method that could solve the issue of the direct collapse of supermassive zero-metal stars into black holes.

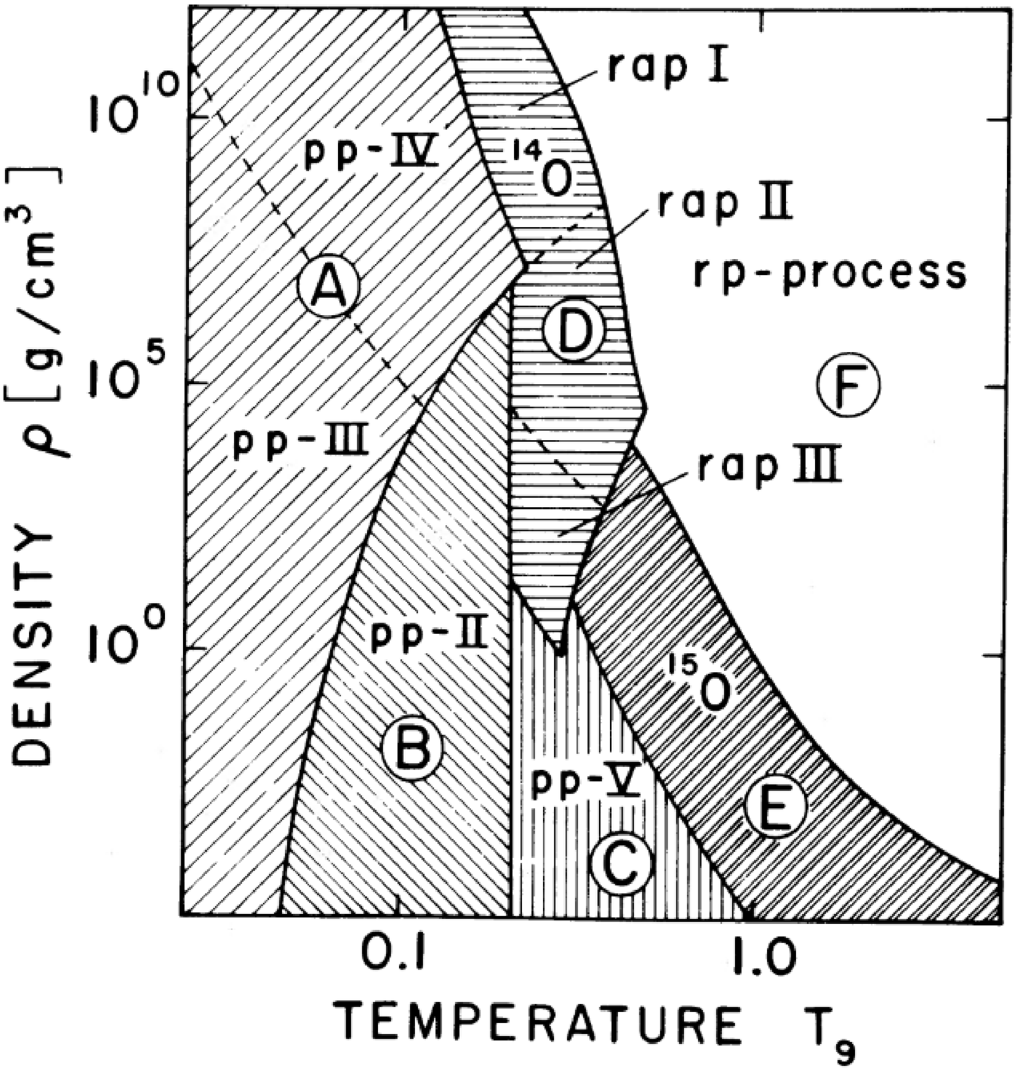

Figure 7.6: Density vs temperature plot proposed in Weisher *et al.* [7] that shows the prevalent processes and the breakout regions to the rp-process. The rap processes provide a link between the traditional pp chain and the rp or α-capture processes. This figure was reproduced with permission from [7] ©AAS.

7.3 Important Reactions to Study with TexCAAM

7.3.1 The ^{7}Be($^{6}Li, d\gamma$)^{11}C Reaction

The ^{7}Be$(\alpha, \gamma)^{11}$C reaction is the reaction in common between the different proposed alternatives of ^{12}C production. The primary study of this reaction was by Hardie *et al.* in 1984 where they aimed to determine the reaction rate of this process. This study was performed in forward

Chain/Process	Reaction Sequence
pp-III	$^{7}\mathrm{Be}(p,\gamma)^{8}\mathrm{B}(\beta^{+}\nu)^{8}\mathrm{Be}(\alpha)^{4}\mathrm{He}$
pp-IV	$^{7}\mathrm{Be}(p,\gamma)^{8}\mathrm{B}(p,\gamma)^{9}\mathrm{C}(\beta^{+}\nu)^{9}\mathrm{B}(p)^{8}\mathrm{Be}(\alpha)^{4}\mathrm{He}$
pp-II	$^{7}\mathrm{Be}(e^{-},\nu)^{7}\mathrm{Li}(p,\alpha)^{4}\mathrm{He}$
pp-V	$\boldsymbol{^{7}\mathrm{Be}(\alpha,\gamma)^{11}\mathrm{C}}(\beta^{+}\nu)^{11}\mathrm{B}(p,2\alpha)^{4}\mathrm{He}$
rap-I	$^{7}\mathrm{Be}(p,\gamma)^{8}\mathrm{B}(p,\gamma)^{9}\mathrm{C}(\alpha,p)^{12}\mathrm{N}(p,\gamma)^{13}\mathrm{O}(\beta^{+}\nu)^{13}\mathrm{N}(p,\gamma)^{14}\mathrm{O}$
rap-II	$\boldsymbol{^{7}\mathrm{Be}(\alpha,\gamma)^{11}\mathrm{C}}(p,\gamma)^{12}\mathrm{N}(p,\gamma)^{13}\mathrm{O}(\beta^{+}\nu)^{13}\mathrm{N}(p,\gamma)^{14}\mathrm{O}$
rap-III	$\boldsymbol{^{7}\mathrm{Be}(\alpha,\gamma)^{11}\mathrm{C}}(p,\gamma)^{12}\mathrm{N}(\beta^{+}\nu)^{12}\mathrm{C}(p,\gamma)^{13}\mathrm{N}(p,\gamma)^{14}\mathrm{O}$
rap-IV	$\boldsymbol{^{7}\mathrm{Be}(\alpha,\gamma)^{11}\mathrm{C}}(\alpha,p)^{14}\mathrm{N}(p,\gamma)^{15}\mathrm{O}$
rp	$^{14}\mathrm{O}(\alpha,p)^{17}\mathrm{F}(p,\gamma)^{18}\mathrm{Ne}(\beta^{+}\nu)^{18}\mathrm{F}(p,\alpha)^{15}\mathrm{O}(\alpha,\gamma)^{19}\mathrm{Ne}(p,\gamma)^{20}\mathrm{Na}$

Table 7.2: A table of the processes for the hot-pp chain, rap process, and the rp processes. The bold reaction is the main reaction of interest and is further described in section 7.3.1. This table is adapted from the one found in [7].

kinematics, leading to technical difficulties in producing a ^{7}Be target. ^{7}Be was electrophoretically deposited onto a platinum disc, causing solids of light elements to form on the disc. The total amount of ^{7}Be is quoted to decay to half of the original amount at the time of the experiment. The inhomogeneities and thermal diffusion of the target may have lead to distortions of the resonance shapes. While not well constrained themselves, the Γ_α (alpha partial widths) of the states of interest were found and helped constrain the reaction rate (Figure 7.7).

In 1995, the data from Hardie *et al.* was used by P. Descouvemont [8] in a microscopic three-cluster theoretical model to determine their contributions to the total reaction rate for $^{7}\mathrm{Be}(\alpha,\gamma)^{11}\mathrm{C}$, and the analog $^{7}\mathrm{Li}(\alpha,\gamma)^{11}\mathrm{B}$ reaction, up to temperatures of 10^{9} K. The theoretical model in this paper failed to observe the $\frac{5}{2}^{-}$ state at 8.4 MeV and the $\frac{3}{2}^{-}$ state at 8.1 MeV (Figure 7.7). With this along with the very weak Γ_α in Hardie *et al.* 's work, P. Descouvemont claimed that these two states were intruder states. Calculations continued to the $\frac{3}{2}^{+}$ sub-threshold state at 7.4997 MeV (-44 keV below the α threshold). Interestingly, the contribution of this sub-threshold state was found to significantly influence the reaction rate in the hot-pp/rap chain temperature regime. Figure 7.8 shows that at lower temperatures the non-resonant contribution substantially changes the reaction rate compared to previous studies.

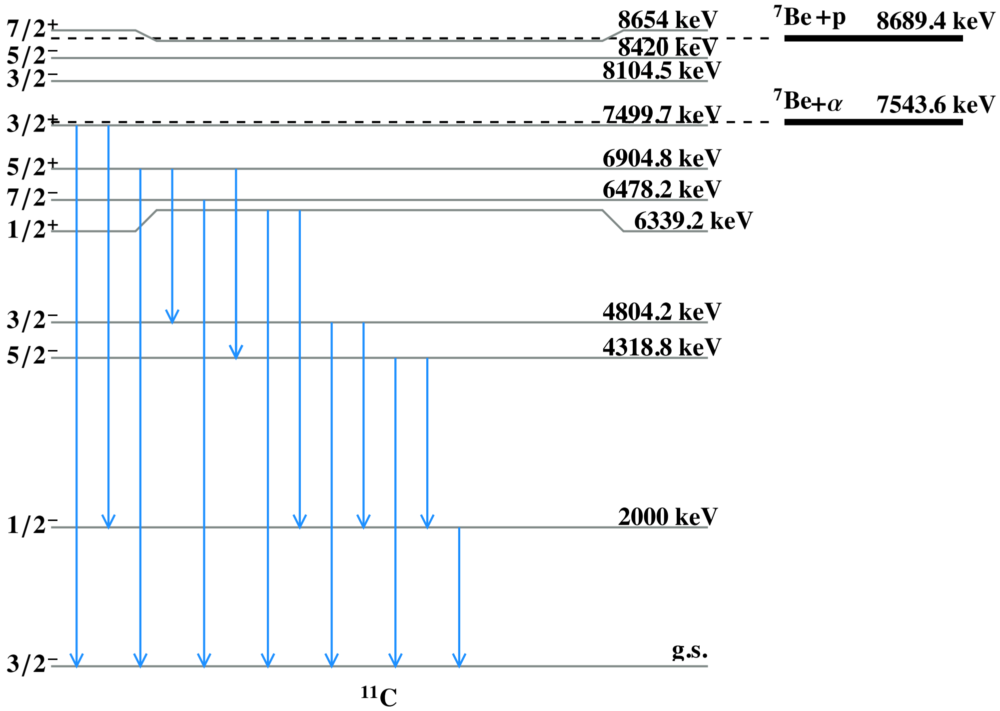

Figure 7.7: Level scheme of ^{11}C . The alpha threshold is at 7.5436 MeV. The two states that were studied by Hardie *et al.* are the $\frac{5}{2}^{-}$ state at 8.4 MeV and the $\frac{3}{2}^{-}$ state at 8.1 MeV. This level scheme is cut short because states above the proton threshold have little contribution to this study therefore could be omitted.

7.3.2 The ^{7}Li(^{6}Li, $d\gamma$)^{11}B Reaction

The ^{7}Li$(\alpha,\gamma)^{11}$B reaction is an analogue reaction to the ^{7}Be$(\alpha,\gamma)^{11}$C reaction. As shown in figure 10.4, the structure of ^{11}B is analogous to ^{11}C . The analogue state to the $\frac{3}{2}^{+}$ state at 7.499 MeV in ^{11}C is the $\frac{3}{2}^{+}$ state at 7.9778 MeV in ^{11}B . By doing the same reaction with a ^{7}Li beam, instead of a ^{7}Be beam, the $\frac{3}{2}^{+}$ state in ^{11}B can be probed and the properties for the analogue state in ^{11}C can be inferred.

Hardie *et al.* [84] studied the ^{7}Li$(\alpha,\gamma)^{11}$B reaction alongside with the ^{7}Be$(\alpha,\gamma)^{11}$C reaction. The target produced for the ^{7}Li$(\alpha,\gamma)^{11}$B reaction didn't see the same defects that the previous target had. Resonance strengths as well as γ and α partial widths were found for the $\frac{5}{2}^{-}$ at 8.92 MeV, $\frac{7}{2}^{+}$ at 9.19 MeV, $\frac{5}{2}^{+}$ at 9.27 MeV states in ^{11}B. However, just like the ^{7}Be$(\alpha,\gamma)^{11}$C reaction, the $\frac{3}{2}^{+}$ sub-threshold state was not observed, nor could it have been. This sub-threshold state is also

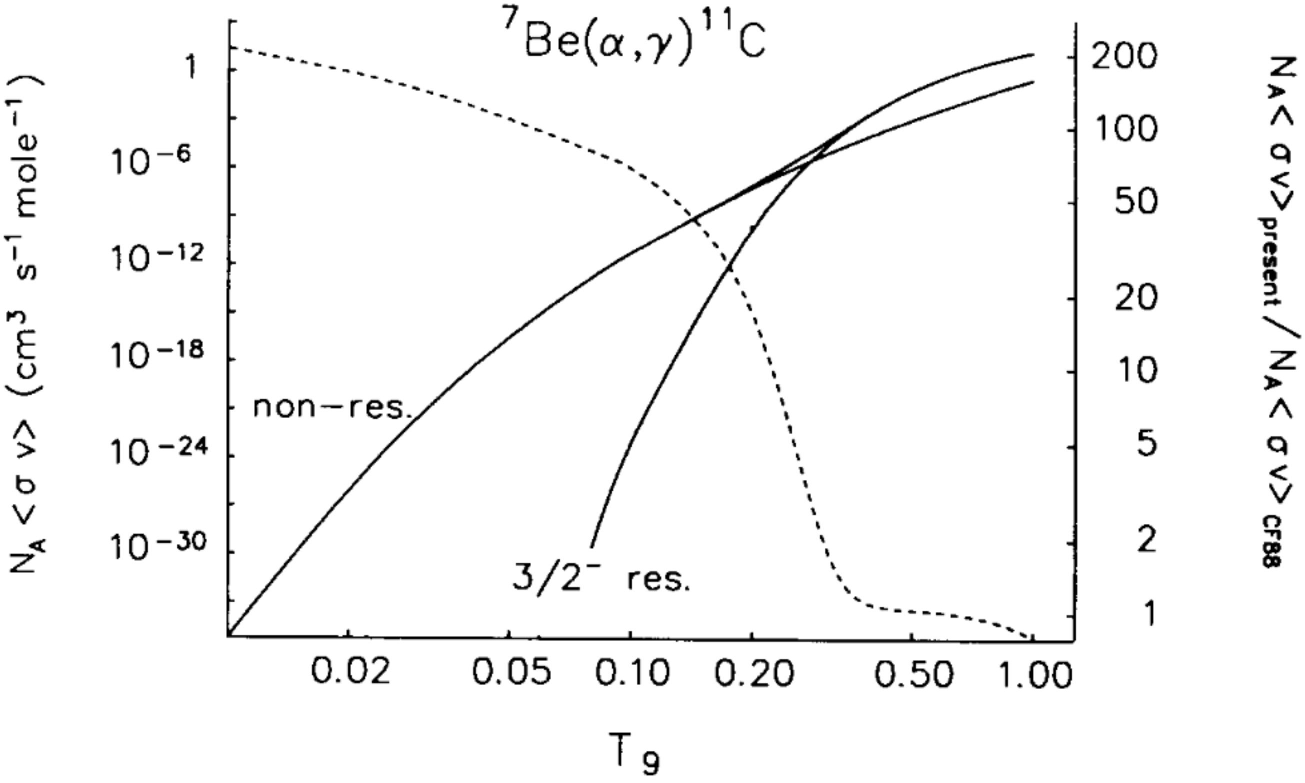

Figure 7.8: The reaction rate contribution from the states studied in [8]. The solid lines are the calculated reaction rates and they use the left scale. The dashed line is the ratio of the contribution compared to Caughlan and Fowler [9] and uses the right-hand scale. Reprinted from Nuclear Physics, Section A, vol. 584, no. 3, P. Descouvemont, "The 7Be(α, γ)11C and 7Li(α, γ)11B reactions in a microscopic three cluster model", pp.532-546 (1995) with permission from *Elsevier*.

predicted to have a significant contribution to the reaction rate at lower temperatures [8].

Norbeck *et al.* [85] studied the ^{7}Li+^{6}Li reaction using a 2 MeV beam of ^{7}Li. The products of the reaction were: ^{11}C+2n, ^{12}B+p, and ^{12}C+n. These products have the Q-values of 2.2, 8.34, and 20.92 MeV, respectively. While the reactions to ^{12}B and ^{12}C have high Q-values neither have observed γ-rays that may compete with the $\frac{3}{2}+$ state of interest in ^{11}B [86].

Similarly, if the same reactions occurred for ^{7}Be+^{6}Li, the products of the reaction would be ^{12}C+p and ^{12}N+n. They have a Q-value of 15.07 and 4.45 MeV, respectively. As in the ^{7}Li case, ^{12}C does not have any observed γ-rays that may compete with the $\frac{3}{2}+$ state of interest in ^{11}C.

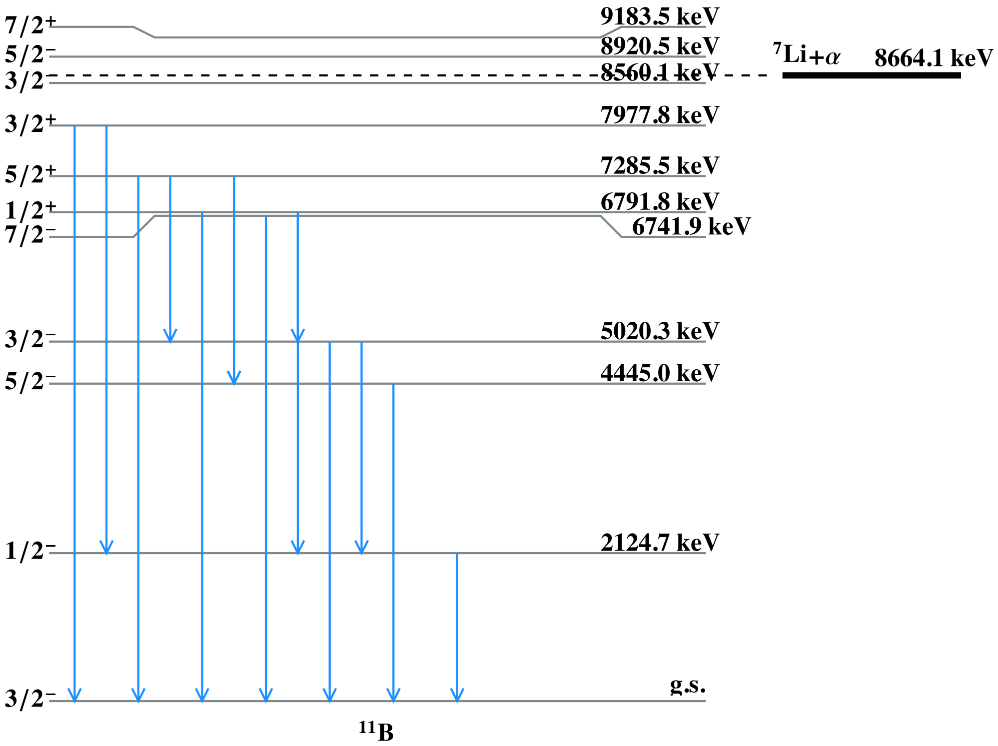

Figure 7.9: Level scheme of ^{11}B. The α threshold is at 8.6641 MeV. The analogue state to the $\frac{3}{2}^{+}$ state at 7.4997 MeV in ^{11}C is the $\frac{3}{2}^{+}$ state at 7.9778 MeV (-686.3 keV below α threshold) in ^{11}B. The level scheme is truncated to exclude higher states above 9.1835 MeV since these higher energy excited states will not contribute in the analysis. The γ-ray cascades are only shown for states with energies below that of the initial beam energy.

7.3.3 The ^{12}C(^{6}Li, $d\gamma$)^{16}O Reaction

The ^{12}C(^{6}Li, $d\gamma$)^{16}O reaction has been well studied, particularly with the same methodology proposed with TexCAAM. In particular, the 2^{+} state at 6.92 MeV and the 1^{-} state at 7.12 MeV in ^{16}O have been well studied. The ANCs for these states were found to be C^2=(1.24 $\pm$ 0.24)x10^{10} fm^{-1} and C^2=(4.33 $\pm$ 0.84)x10^{28} fm^{-1}, respectively [87, 88]. The ^{12}C(^{6}Li, $d\gamma$)^{16}O reaction would further prove the viability of TexCAAM, as well as further constrain its efficiency.

7.3.4 Resonance Reactions

TexCAAM is also well designed to perform resonance reactions such as (p, p') and (α, α'). One interesting reaction is the ^{7}Be(p, p') reaction to probe the structure of ^{8}B. ^{8}B is one of the heaviest elements created in the pp chain and understanding the structure is crucial to understanding the bridge between A=8 (pp chain) elements and heavier elements. ^{8}B β decay is also responsible for the majority of neutrinos above 1 MeV and understanding its structure is crucial in understanding the ^{8}B solar neutrino flux. ^{8}B does not have any bound excited states [89]. It is also believed that the 2^+ ground state is a proton halo state, which would make it the only known proton halo ground state. The ^{8}B halo ground state can be imagined as a ^{7}Be+p system with a ^{7}Be core and extended proton wavefunction. Therefore, proton capture reactions can illuminate the structure of ^{8}B [89].

Previous studies of the proton elastic scattering on ^{7}Be have observed evidence for an array of resonance states in ^{8}B. Gol'dberg *et al.* [90] observed a 1^- or 2^- resonance state at 3 MeV, a 1^+ resonance state at 2.8(15) MeV, and a 3^+ resonance state at 2.32(20) MeV. Rogachev *et al.* [91] provided evidence for the existence of a broad 2^- resonance state at 3.5(5) MeV. Yamaguchi *et al.* [92] confirmed a 2^- resonance state at 3.2(3) MeV, and suggested a 1^- resonance state at 5.0(4) MeV, and a 3^+ resonance state somewhere near 7 MeV. Mitchell *et al.* [93] observed a 0^+ state at 1.9 MeV as well as a 2^+ state at 2.55 MeV. Paneru *et al.* [94] also observe a 0^+ state at 1.9 MeV and a 2^+ state at 2.21 MeV. This work also determined the scattering length for the 2^- state at 3.5 MeV. A low-lying 1^+ resonance state at 770(3) keV has also been observed [95]. Additionally, a 0^+ resonance at 10.6 MeV has been observed through the ^{11}B(^{3}He,^{6}He)^{8}B reaction [96]. Understanding the full structure of ^{8}B is necessary to constrain the ^{7}Be$(p,\gamma)^8$B reaction rate. Using TexCAAM, a high statistics measurement of the ^{7}Be(p,p') excitation function can confirm the 0^+ and 2^+ states observed in Mitchell *et al.* and Paneru *et al.*

Similar resonance reactions can be performed with TexCAAM as well. The structure of ^{11}N can be probed via the ^{10}C+p scattering to verify previously observed states, and to search for new states. The structure of ^{12}N can be studied via the ^{11}C+p. Another important study is the structure of ^{18}Ne via the ^{17}F+p scattering to determine the spin and parity assignments for the 5 MeV and 5.1 MeV states, among others. The structure of ^{18}Ne is important for both the ^{17}F$(p,\gamma)^{18}$Ne reaction rate and the ^{14}O$(\alpha,p)^{17}$F reaction rate [97]. Determining the nuclear structure of ^{18}Ne is of importance for the hot CNO cycle, in particular the ^{14}O$(\alpha,p)^{17}$F$(p,\gamma)^{18}$Ne$(\alpha,p)^{21}$Na chain [98, 99].

8. SUB-COULOMB ALPHA TRANSFER REACTIONS

As described in detail in the previous chapter (chapter 7), some of the most interesting reactions to be studied with TexCAAM are sub-Coulomb α transfer reactions. In fact, the primary purpose of the development of TexCAAM was the ability to study these reactions with rare isotope beams, which has not been possible until now at Texas A&M University.

The ^{7}Be($^{6}\mathrm{Li}, d\gamma$)^{11}C reaction (Figure 8.1), and other α-transfer reactions, typically rely on an incident beam bombarding a ^{6}Li (deuteron ejectile) or a ^{7}Li (triton ejectile) target. The lithium will transfer an α particle to the incident beam forming a heavy product nucleus and eject the light ejectile particle (the deuteron or triton). This product nucleus may be excited, which would lead to the nucleus decaying via γ-ray emission.

The cross section for sub-Coulomb α-transfer reactions provides crucial information on the α-cluster properties of the near and sub-threshold resonances, constraining the α-capture reaction rates.

8.1 Cross Section

The cross section for low energy (sub-barrier) fusion or capture reaction is a result of the transmission probability through the Coulomb barrier. The transmission probability quantity, P, is defined as [5]:

$$P = e^{-2\pi\eta}, \tag{8.1}$$

where η is defined as the Sommerfeld parameter (in Gauss system of units)

$$\eta = \frac{Z_1 Z_2 e^2}{\hbar\nu}, \tag{8.2}$$

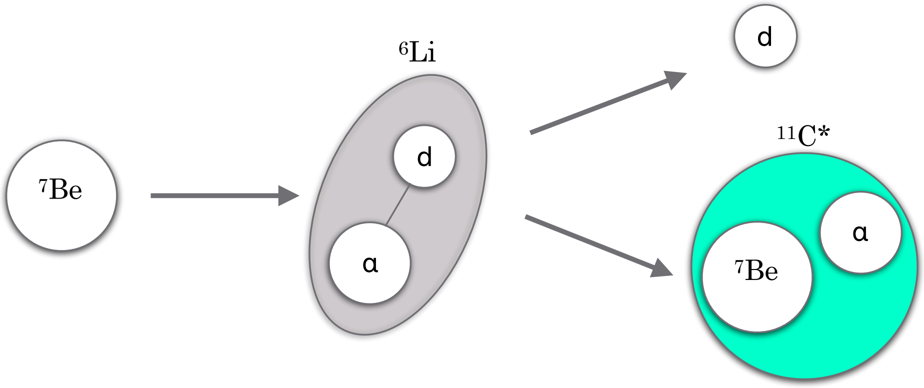

Figure 8.1: A diagram depicting the ^{7}Be(^{6}Li$, d\gamma)^{11}$C reaction. A ^{7}Be beam is produced through MARS and bombards a ^{6}Li target. For ease of visualization, the ^{6}Li can be thought of as an α-deuteron cluster. The ^{7}Be beam will pick up the α particle from the ^{6}Li leaving behind the deuteron. The deuteron is ejected from the reaction, taking away energy from the system. The ^{7}Be and the α particle combine to form a ^{11}C nucleus, which may be left in an excited state. An excited ^{11}C nucleus will deexcite via γ-ray emission. The ^{11}C nucleus may come out of the α-transfer reaction with kinetic energy, contributing a doppler shift to the emitted γ rays. Eventually, the ^{11}C (T$_{1/2}$=20.364(14) min [10]) will ε or β^{+} decay to ^{11}B.

where ν is the particle velocity. In terms of particle energy, E, the Sommerfeld parameter is

$$\eta = \alpha Z_1 Z_2 \sqrt{\frac{\mu c^2}{2E}}, \tag{8.3}$$

where α is the fine structure constant ($\sim \frac{1}{137}$) and μ is the reduced mass. Since the cross section is just a definition of the reaction probability, it makes sense to suggest that the cross section, σ, is proportional to the tunneling probability, P (i.e. $\sigma(E) \propto e^{-2\pi\eta}$). However, additional terms are required to account for physical effects. The first is accounting for the particle wavelength, i.e. the de Broglie wavelength $\frac{1}{E}$. The second accounts for the remaining nuclear effects and is just defined as the astrophysical *S*-factor, $S(E)$. Therefore, we can define the total cross section as

$$\sigma(E) = \frac{1}{E} e^{-2\pi\eta} S(E) \tag{8.4}$$

The astrophysical *S*-factor is generally the term that is investigated and determined experimentally. The major benefit of using the astrophysical *S*-factor, opposed to using the cross section, is that the *S* factor varies smoothly and gradually with respect to the c.m. energy unless a resonance is encountered. This makes it favorable when extrapolating to the lower energies, observed in astrophysical environments [5].

8.2 Reaction Rate

The rates at which reactions take place in stellar environments heavily influence how stars evolve and the final abundance of elements. In the case of the specific reactions of interest, the reaction rate can be compared to the reaction rate of the triple-α process to determine the contribution of the specific hot-pp chains to the total ^{12}C abundance in zero metallicity stars, therefore giving insight on when the CNO cycle kicks off.

The reaction rate is defined as:

$$N_A < \sigma\nu >= \int_0^\infty \sigma(\nu)\Phi(\nu)\nu d\nu, \tag{8.5}$$

where $\sigma(\nu)$ is the cross section, $\Phi(\nu)$ is the Maxwell-Boltzmann distribution, and ν is particle velocity. In terms of the center-of-mass energy, $E = \frac{1}{2}\mu\nu^2$, we can rewrite it as:

$$N_A < \sigma\nu >= \left(\frac{8}{\pi\mu}\right)^{1/2} \frac{1}{(kT)^{3/2}} \int_0^\infty \sigma(E)Ee^{\frac{-E}{kT}}dE \tag{8.6}$$

When substituting the astrophysical *S*-factor into the reaction rate, it becomes

$$N_A < \sigma\nu >= \left(\frac{8}{\pi\mu}\right)^{1/2} \frac{1}{(kT)^{3/2}} \int_0^\infty S(E)e^{-\frac{E}{kT}-\frac{b}{E^{1/2}}}dE, \tag{8.7}$$

where b, which arises from the barrier penetrability, is

$$b = \sqrt{2\mu}\pi e^2 \frac{Z_1 Z_2}{\hbar} \tag{8.8}$$

The Gamow energy is defined as $E_G = b^2$. The Gamow energy is used to determine the tunneling through the Coulomb barrier which is $\propto e^{-\sqrt{E_G/E}}$. A combination of the Coulomb barrier penetration and the Maxwell-Boltzmann distribution ($\propto e^{-\frac{E}{kT}}$) leads to the Gamow peak (Figure 8.2). The integrand of equation 8.7 comes from the Gamow peak formulation, hence the area under the Gamow peak determines the reaction rate. The Gamow peak is maximal about the energy $E_0 = \left(\frac{bkT}{2}\right)^{2/3} = 1.22(Z_1^2 Z_2^2 \mu T_6^2)^{1/3}$ keV with T_6 as the temperature in 10^6 Kelvin or one MK (Mega-Kelvin). E_0 is the effective mean energy for thermonuclear fusion reactions at the temperature T. The full-width half-maximum (FWHM) of the Gamow peak is defined as $\Delta E = \frac{4}{3^{1/3}}(E_0 kT)^{1/2} = 0.749(Z_1^2 Z_2^2 \mu T_6^5)^{1/6}$ keV.

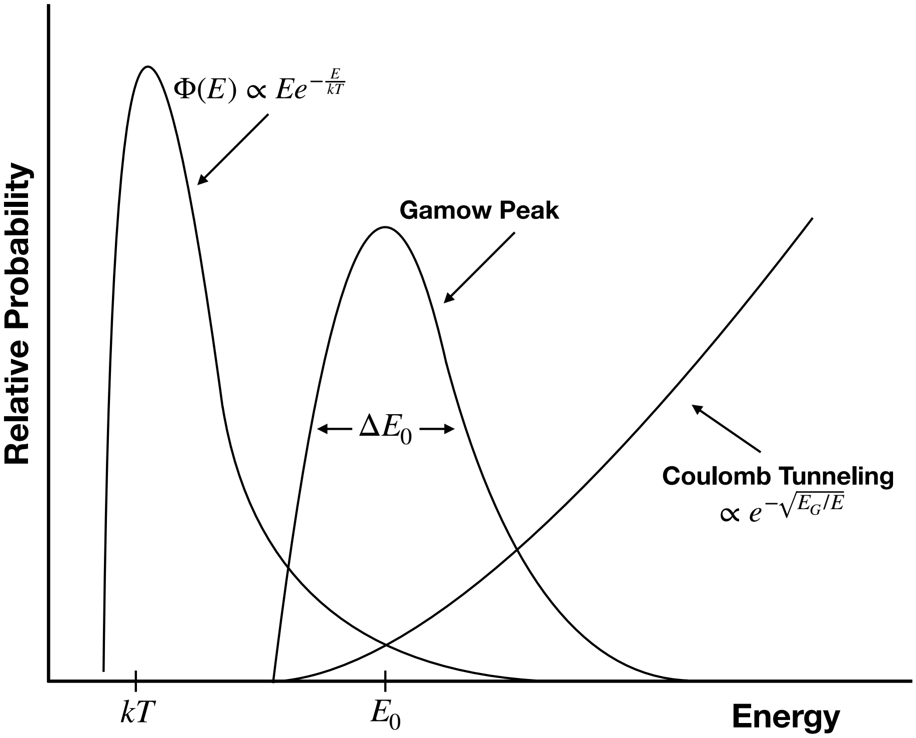

Figure 8.2: A realtive probability vs. energy plot to show how the Gamow Peak is formed from the Maxwell-Boltzmann distribution ($\Phi(E)$) and the Coulomb tunneling terms. E_0 is the effective mean energy for thermonuclear fusion reactions and is the point where the Gamow peak is maximal. This figure was adapted from one found in [5].

Additionally, the reaction rate can take another form under the approximation of narrow resonances. The approximation produces a reaction rate in the form of

$$N_A < \sigma\nu >_r = \frac{1.539x10^{11}}{(\mu_{A-a,a} T_9)^{3/2}} e^{-11.605E_r/T_9} (\omega\gamma)_r, \tag{8.9}$$

where $\mu_{A-a,a}$ is the reduced mass ($\mu_{A-a,a} = \frac{m_{A-a}m_a}{m_{A-a}+m_a}$), E_r is the resonance energy, T_9 is the temperature in MK, and $(\omega\gamma)_r$ is the resonance strength defined as

$$(\omega\gamma)_r = \frac{2J_r + 1}{(2J_{A-\alpha}+1)(2J_\alpha+1)} \frac{\Gamma_\alpha \Gamma\gamma}{\Gamma}, \tag{8.10}$$

where J_α is the spin of the α cluster, $J_{A-\alpha}$ is the spin of the $A-\alpha$ cluster (see Figure 8.3, α is x in the figure), J_r is the spin of the narrow resonance, Γ_α is the α width, and $\frac{\Gamma_\gamma}{\Gamma}$ is the γ-decay branching ratio [100, 101].

8.2.1 Optical Model Potentials

Theoretical analysis of nuclear reaction cross sections often involves optical model potential, which I introduce in this chapter. The optical model has been shown to successfully describe the interaction between two nuclei, even heavy ions such as uranium. Apart from a possible spin dependence, the interaction between the two nuclei is assumed to depend only on the distance between the center of masses [102]. For the analysis of scattering experiments, the widely used form of optical model potentials (OMPs) is described as

$$U(r) = -Vf(r,R,a) - iWf(r,R',a') - iW_D g(r,R',a'), \tag{8.11}$$

where f is the Woods-Saxon form factor

$$f(r,R,a) = (e^{\frac{r-R}{a}} + 1)^{-1}, \tag{8.12}$$

where a is the diffuseness, R=1.25$A^{1/2}$ fm, V is the real component and W is the imaginary component of the particle potential, W_D is the imaginary surface potential depth, and g is defined as

$$g(r, R', a') = 4a\frac{d}{dr}f(r, R', a') \tag{8.13}$$

The Woods-Saxon form factor is 1 at the origin ($f(r{=}0){\approx}1$) and $\frac{1}{2}$ at $r = R$. The potential dies off quickly as the Woods-Saxon form factor will fall almost 90% over a range of $4.4a$ centered at $r = R$ [102]. To account for particle spin, a spin-orbit term (U_{so}) can be added with the form

$$U_{so} = g_{so}(r)\overrightarrow{l} \cdot \overrightarrow{s}, \tag{8.14}$$

where

$$g_{so}(r) \propto \frac{1}{r}\frac{d}{dr}f(r, R_{so}, a_{so}) \tag{8.15}$$

Commonly used potential terms in the optical model are the Coulomb term ($V_c(r)$), a real volume term ($-V_R f_R(r)$), an imaginary volume term ($-iW_S f_S(r)$), a real surface term ($4a_D V_D \frac{df_D(r)}{dr}$), an imaginary surface term ($i4a_D W_D \frac{df_D(r)}{dr}$), a real spin-orbit term ($V_{so}\big(\frac{\hbar}{m_\pi c}\big)^2 g_{so}(r)(\overrightarrow{l} \cdot \overrightarrow{s})$), an imaginary spin-orbit term ($iW_{so}\big(\frac{\hbar}{m_\pi c}\big)^2 g_{so}(r)(\overrightarrow{l} \cdot \overrightarrow{s})$), and for charged particles with $l > 0$ a centrifugal barrier term ($V_{cf}(r) = \frac{l(l+1)\hbar^2}{2\mu r}$) [12].

Solving Schrödinger equation with the potential of the form given above leads to a good description of elastic scattering and many other experimental data over the large range of energy and masses.

8.2.2 Distorted-Wave Born Approximation

The scattering amplitude for some wave function $\chi(\mathbf{r})$ with a fixed potential $V(\mathbf{r})$ can be determined by solving the Schrödinger equation

$$\Big[-\frac{\hbar^2}{2m}\nabla^2 + V(\mathbf{r})\Big]\chi(\mathbf{r}) = E\chi(\mathbf{r}), \tag{8.16}$$

where E is the particle energy. If a plane wave is chosen for $\chi(\mathbf{r})$, then the scattering amplitude for the outgoing scattered wave is

$$f(\theta,\phi) = -\frac{1}{4\pi}\int e^{-i\mathbf{k'}\cdot\mathbf{r'}}U(\mathbf{r'})\chi(\mathbf{k},\mathbf{r'})d\mathbf{r'} \tag{8.17}$$

The Born approximation assumes a weak potential (V), which will weakly interact with the initial plane wave, and takes the unknown $\chi(\mathbf{r'})$ as the initial plane wave. Therefore the Born approximation is just

$$f_{BA}(\theta,\phi) = -\frac{1}{4\pi}\int e^{-i\mathbf{q}\cdot\mathbf{r'}}U(\mathbf{r'})d\mathbf{r'}, \tag{8.18}$$

where $\mathbf{q} = \mathbf{k} - \mathbf{k'}$ and represents the change in momentum of the scattered particle. The scattering amplitude depends on θ, as $q^2 = k^2 + k'^2 - 2kk'cos(\theta)$. Since $U(\mathbf{r})$ is spherically symmetric, the integral becomes

$$f_{BA}(\theta,\phi) = -\frac{1}{q}\int sin(q\mathbf{r'})U(\mathbf{r'})\mathbf{r'}d\mathbf{r'} \tag{8.19}$$

Similarly, the distorted-wave Born approximation (DWBA) assumes that the potential U is the sum of two potentials U_1 and U_2. The DWBA scattering amplitude is

$$f_{DWBA}(\theta,\phi) = f_1(\theta,\phi) - \frac{1}{4\pi}\int \chi_1^{(-)}(\mathbf{k'},\mathbf{r'})U_2(\mathbf{r'})\chi_1^{(+)}(\mathbf{k},\mathbf{r'})d\mathbf{r'}, \tag{8.20}$$

where $f_1(\theta,\phi)$ is the scattering amplitude from the potential U_1, $\chi_1^{(-)}(\mathbf{k},\mathbf{r})$ is the ingoing scattered wave, and $\chi_1^{(+)}(\mathbf{k},\mathbf{r})$ is the outgoing scattered wave. This approximation can be used to address multiple interactions, such as U_1 accounting for elastic scattering and U_2 accounting for interactions that induce non-elastic transitions [102]. The differential cross section for some A(a.b)B reaction is

$$\frac{d\sigma}{d\Omega} = \frac{\mu_\alpha\mu_\beta}{(2\pi\hbar^2)^2}\frac{k_\beta}{k_\alpha}|T|^2, \tag{8.21}$$

where the $|T|^2$ term is the transition amplitude and α, β denote the entrance and exit channels, respectively. For DWBA, this transition amplitude can be described as

$$T^{DWBA} = \int \chi^{(-)}(\mathbf{k}_\beta, \mathbf{r}) F(\mathbf{r}) \chi^{(+)}(\mathbf{k}_\alpha, \mathbf{r}) d\mathbf{r}, \tag{8.22}$$

where $F(r)$ is defined as

$$F(r) = \int \Psi_B^* \Psi_b^* V \Psi_A \Psi_a d\tau', \tag{8.23}$$

where τ' just represents all variables to be integrated over.

For most transfer reactions, the first-order DWBA transition amplitude is used (equation 8.22). An assumption that the reaction is zero range is used to simplify the integral, reducing it to a single vector coordinate. We can take the reaction A+a → B+b, where A is the projectile, a is the target that consists of the ejectile nucleon(s) b and the transferred nucleon(s) x (a=b+x), and the product nucleus B which consists of A and x (B=A+x). Relative distance vectors $\mathbf{R}$ and $\boldsymbol{\rho}$ can be used to define the distance between A and x, and b and x, respectfully (Figure 8.3). Relative vectors that connect A to a and B to b can be defined as $\mathbf{r}_\alpha = \mathbf{R} - (b/a)\boldsymbol{\rho}$ and $\mathbf{r}_\beta = (A/B)\mathbf{R} - \boldsymbol{\rho}$.

The variables of integration can be converted from $\mathbf{R}$ and $\boldsymbol{\rho}$ to $\mathbf{r}_\alpha$ and $\mathbf{r}_\beta$ via $d\boldsymbol{\rho} d\mathbf{R} = J d\mathbf{r}_\alpha d\mathbf{r}$. J is a Jacobian defined as

$$J = \frac{\partial(\boldsymbol{\rho}, \mathbf{R})}{\partial(\mathbf{r}_\alpha, \mathbf{r}_\beta)} = \left(\frac{a}{x}\frac{B}{A+a}\right)^3 \tag{8.24}$$

The DWBA transition amplitude becomes

$$T_{\alpha\beta}^{DWBA} = J \int \chi_\beta^{(-)*}(\mathbf{k}_\beta, \mathbf{r}_\beta)(\Phi_B \Phi_b | V_\beta - U_\beta | \Phi_A \Phi_a) \chi_\alpha^{(+)}(\mathbf{k}_\alpha, \mathbf{r}_\alpha) d\mathbf{r}_\alpha d\mathbf{r}_\beta, \tag{8.25}$$

where U_β is the optical potential for the exit channel, V_β is the two-nucleon interaction for the exit channel, and $(\Phi_B \Phi_b | V_\beta - U_\beta | \Phi_A \Phi_a)$ is the nuclear overlap function [11]. Following equation 8.21, the DWBA differential cross section is

$$\left(\frac{d\sigma}{d\Omega}\right)_{DWBA} = \frac{\mu_\alpha \mu_\beta}{(2\pi\hbar^2)^2} \frac{k_\beta}{k_\alpha} |T_{\alpha\beta}^{DWBA}|^2 \tag{8.26}$$

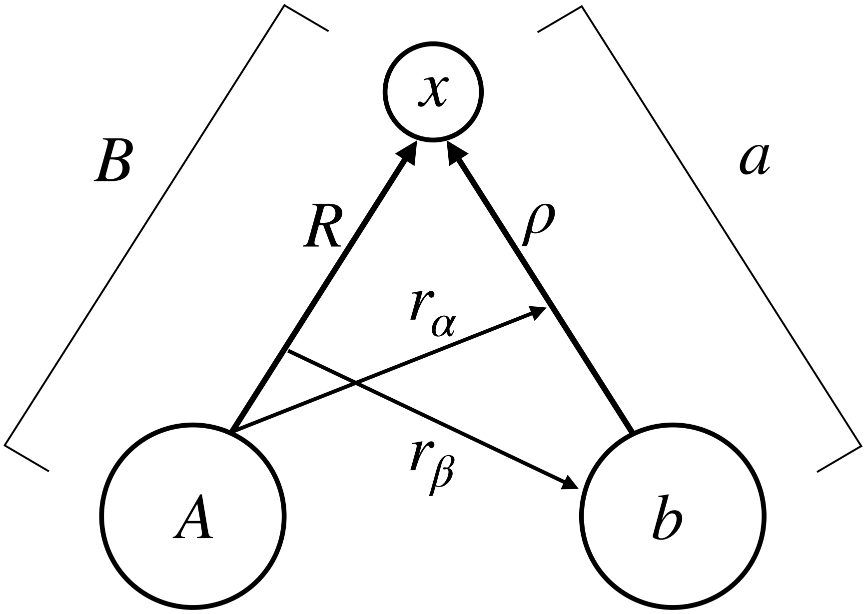

Figure 8.3: Finite-range interaction for a transfer reaction. A is the projectile nucleus, a is the target (a=b+x), B is the product nucleus (B=A+x), b is the ejected particle, and x is the transferred nucleon or nucleon group. This figure is modified from the one found in [11].

The DWBA differential cross section relates to the experimental differential cross section via

$$\frac{d\sigma}{d\Omega}\Big|_{exp} = S_\alpha S_\beta \frac{d\sigma}{d\Omega}\Big|_{DWBA}, \tag{8.27}$$

where S_i is the spectroscopy factor for $i = \alpha$ or β.

8.2.3 FRESCO

FRESCO [103], similar to other programs such as DWUCK [104], can be used to determine differential cross sections via DWBA calculations. FRESCO can perform calculations for nearly any reaction that can be described in coupled-channel form. Physics inputs, such as excited states and spins and parities, are required along with OMPs, overlap functions, and couplings. Calculated differential cross sections are often given as a ratio to the Rutherford differential cross section

$$\left.\frac{d\sigma}{d\Omega}\right|_{Ruth} = \left(\frac{Z_1 Z_2 \alpha \hbar c}{4E sin^2\frac{\theta}{2}}\right)^2, \tag{8.28}$$

where α is the fine structure constant and E is the particle energy.

The effective Coulomb barrier is needed to determine the beam energy at sub-Coulomb energies to input into FRESCO calculations. The effective Coulomb barrier can be found via

$$V_C \approx \alpha \hbar c \frac{Z_1 Z_2}{r_0(A_1^{1/3} + A_2^{1/3})}, \tag{8.29}$$

where $r_0 \approx 1.25\ f$m and $\hbar$c=197.3 MeV fm.

An example of a FRESCO calculation for a sub-Coulomb α-transfer reaction can be seen in Figure 8.4. This is an example of an output from FRESCO using OMPs from [12]. Further work will need to be done for future analyses to properly calculate the OMPs for this specific reaction in order to determine the exact differential cross section.

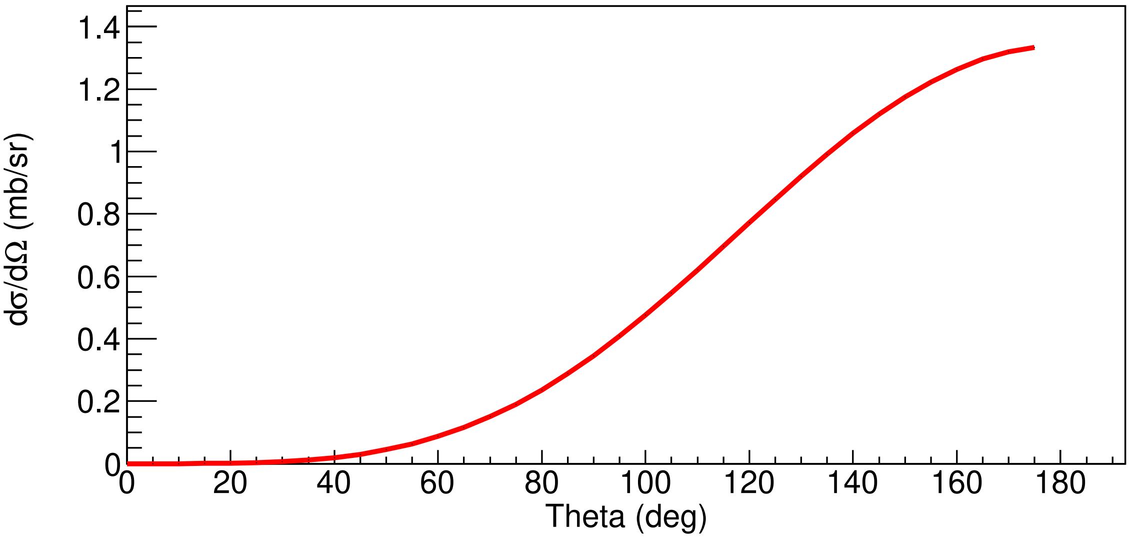

Figure 8.4: An example of a FRESCO differential cross section output. This is for the ^{7}Li(^{6}Li,dγ)^{11}B transfer reaction. The effective Coulomb barrier for this interaction is ∼2.41 MeV. For this output, the interaction occurs at a beam energy of 2.25 MeV. The total cross section from FRESCO is 17.66 mb. The FRESCO calculations were done with estimated OMPs for a ^{7}Li beam, which were taken directly from [12]. Further work should be done to incorporate the proper OMPs.

8.2.3.1 Effective Target Thickness

In conjunction with FRESCO calculations, the effective target thickness needs to be estimated. Since the target is thick and the beam ions are stopped inside the target the effective target thickness will be different of each interaction energy bin. It is inversely proportional to the specific energy losses of the beam ions which can be accurately calculated using SRIM code and experimentally verified. The effective target thickness can be used to determine the experimental cross section.

8.2.4 Asymptotic Normalization Coefficients

When considering the overlap function, nuclear interactions are negligible at large r. At sub-Coulomb energies, only the asymptotic part of the overlap function is important and only influences the overall normalization of the asymptotic wave function [19]. For Li-induced α transfer reactions at very low energies, slightly negative Q-values mean that the outgoing ejectile particle will also be sub-Coulomb in energy. Since interaction potential at low (sub-Coulomb) energies is almost Coulomb potential, the calculated cross sections are essentially model independent [87]. Hence, asymptotic normalization coefficients (ANCs) are nearly independent of optical model parameters. Moreover, since ANCs only depend on the asymptotic of the wave function, the ANCs are independent on the number of nodes and the details of interaction potential for the DWBA form-factor wave function. All this is not true for spectroscopic factors. The overlap function for the bound state wave functions for A,a, and x (described in Figure 8.3) is

$$I_{ax}^{A} = \langle \phi_a(\zeta_a)\phi_x(\zeta_x)|\phi_A(\zeta_a,\zeta_x : \mathbf{r}_{ax})\rangle \tag{8.30}$$

where ϕ_i is the bound state wave function for a nucleus i, ζ_i are the internal coordinates for a nucleus i, and $\mathbf{r}_{ax}$ is the relative coordinate of the center of mass of nuclei a and x. Generally the overlap function can be described by the spectroscopic factor and the bound state wave function, however the asymptotic normalization coefficient can be found, defining the amplitude of the tail of the radial overlap function

$$I^A_{axl_Aj_A}(r_{ax}) \xrightarrow{r_{ax}>R_N} C^A_{axl_Aj_A}\frac{W_{-\eta_A,l_A+1/2}(2\kappa_{ax}r_{ax})}{r_{ax}}, \tag{8.31}$$

where R_N is the nuclear interaction radius between a and x, $W_{-\eta_A,l_A+1/2}(2\kappa_{ax}r_{ax})$ is the Whittaker function, $\kappa_{ax} = \sqrt{2\mu_{ax}\epsilon_{ax}}$ is the wave number of the bound state A, μ_{ax} is the reduced mass of a and x, $\eta_A = \frac{Z_aZ_x\mu_{ax}}{\kappa_{ax}}$ is the Coulomb parameter for the bound state A, and $C^A_{axl_Aj_A}$ is the asymptotic normalization coefficient. The Whittaker function describes the asymptotic behavior of the bound state wave function of two charged particles [105]. The ANC can also be related to the single-particle ANC ($b^A_{axl_Aj_A}$) via the spectroscopic factor

$$(C^A_{axl_Aj_A})^2 = S_{axl_Aj_A}(b^A_{axl_Aj_A})^2 \tag{8.32}$$

According to equation 8.27, this implies the relationship between experimental and DWBA differential cross sections

$$\frac{d\sigma}{d\Omega}\bigg|_{exp} = \frac{(C^A_{ax})^2(C^B_{bx})^2}{(b^A_{ax})^2(b^B_{bx})^2}\frac{d\sigma}{d\Omega}\bigg|_{DWBA} \tag{8.33}$$

ANCs can also be related to *R*-matrix reduced widths (γ_i^2) via

$$C_i^2 = \frac{2\mu a}{\hbar W^2(a)}\Big(\frac{\gamma_i^2}{1+\gamma_i^2\frac{dS}{dE}}\Big) \tag{8.34}$$

where μ is the reduced mass, a is the channel radius, and $S(E)$ is the shift function with the condition that the channel radius, a, is equal to $S(E_i)$, where E_i is the bound state energy. The α partial width, for the sub-Coulomb α-transfer reactions of interest, can be calculated from the ANC. Partial particle widths relate to the particle widths via

$$\Gamma = 2P_l(E)\gamma^2, \tag{8.35}$$

where P_l is the penetrability according to the particle energy E [101]. The narrow resonance reaction rate can then be found using the particle width with equation 8.9.

To summarize, the α ANC for the near α-threshold state can be extracted from the sub-Coulomb α-transfer reaction cross section on an almost model independent basis. This ANC can be linked to the α reduced widths of the state, which in turn determine the cross section for the α-capture reactions through the near α-threshold state in question.

9. DETECTOR DESIGN AND SETUP

9.1 Momentum Achromat Recoil Separator Spectrometer

The Momentum Achromat Recoil Separator (MARS) spectrometer can produce rare isotope beams in the low mass and low energy regime. Stable ions are produced in an ECR source [106] via a gaseous or metallic source. The ionized nuclei are funneled out of the ECR source and injected into the K150 or the K500 cyclotron, where the nuclei are accelerated in beam ‘packets’. The accelerated beam is guided to MARS through a series of bending and focusing magnets. The beam reacts with the gas chamber of MARS to produce a rare isotope beam cocktail. The secondary beams are typically produced through reactions in inverse kinematics. The gas target may consist of a variety of gasses and is kept at LN_2 temperatures ($\sim$ 77 K) to maximize the target density while keeping thin windows to minimize energy loss [107]. A solid target ladder may also be used in MARS to supply a broad range of rare isotope beams.

The stable beam from the cyclotron enters the MARS cave through the SW1 magnet (Figure 9.1). The beam is focused through a quadrupole magnet before being directed into the gas target via the SW2 magnet. The reaction inside of the gas target produces a secondary rare isotope beam that goes through the SL1 solid-angle collimating slits. The D1 dipole magnet will direct the beam towards the SL2 horizontal momentum selection slits. The beam passes through the SL3 vertical slits to limit ions with a large vertical recoil component from being bent into the velocity filter via the D2 dipole magnet. The velocity filter is a Wien filter that selectively allows ions to pass through via $v_{pass} = \frac{E}{B}$. The electric and magnetic fields are set to allow a specific velocity to pass through while velocities greater or less than v_{pass} will be bent into the filter. After the velocity filter, the beam is bent vertically via the D3 dipole magnet and focused through the Q4 and Q5 quadrupole magnets. The remaining two slits, SL4 and SL5, limit the solid angle of the secondary beam and set a mass to charge filter, respectively [107].

One of the primary research interests in the development of MARS includes the determination

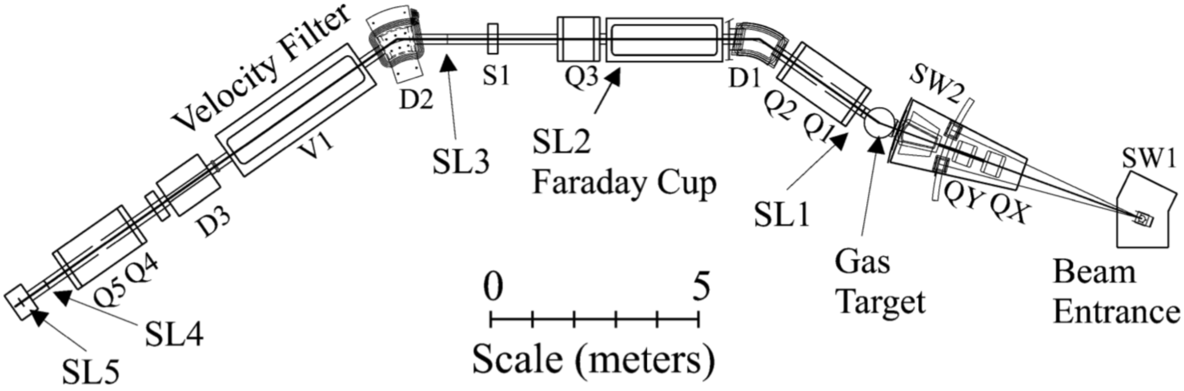

Figure 9.1: The Momentum Achromat Recoil Separator. The beam enters from the right and is directed by a series of dipole and quadrupole magnets. The beam either interacts with the gas target or the solid target ladder to produce a secondary rare isotope beam cocktail. The cocktail is filtered to the isotope of interest through the remaining slits, magnets, and the velocity filter. The experimental apparatus (TexCAAM) is attached to the end of the MARS arm.

of the ANCs for astrophysically-motivated nuclei at stellar energies. In particular, ANCs for the ^{7}Be+p reaction have been measured. MARS was able to deliver the ^{7}Be beam at 12 MeV/u with a purity $>$99.5% [107].

In order to study the $^{7}\text{Be}(^{6}\text{Li}, d\gamma)^{11}\text{C}$ reaction, a ^{7}Be beam at much lower kinetic energies (8 MeV total) is required. MARS was able to produce an almost completely pure beam of ^{7}Be with a beam rate of approximately 4200 counts/nA of primary beam for a total of 10^{5} pps (Figure 9.2). It was produced through the $^{1}\text{H}(^{7}\text{Li},^{7}\text{Be})n$ reaction.

Background radiation is a concern for this experiment. During the beam development period, TexCAAM was placed inside of the MARS cave (not connected to the MARS beamline) and covered in a layer of lead bricks. Measurements of γ rays were performed with the beam on and with the beam off to study the latent radiation in the vault as well as any prompt emission produced during operation. It was found that for all channels combined, the background rate was approximately 2 events per hour in the energy region of interest.

For the ^{11}Be β-decay study, a ^{11}Be beam of approximately 91% purity was delivered on target, where the remainder of the beam was ^{8}Li contamination. The beam rate at the detector, which was

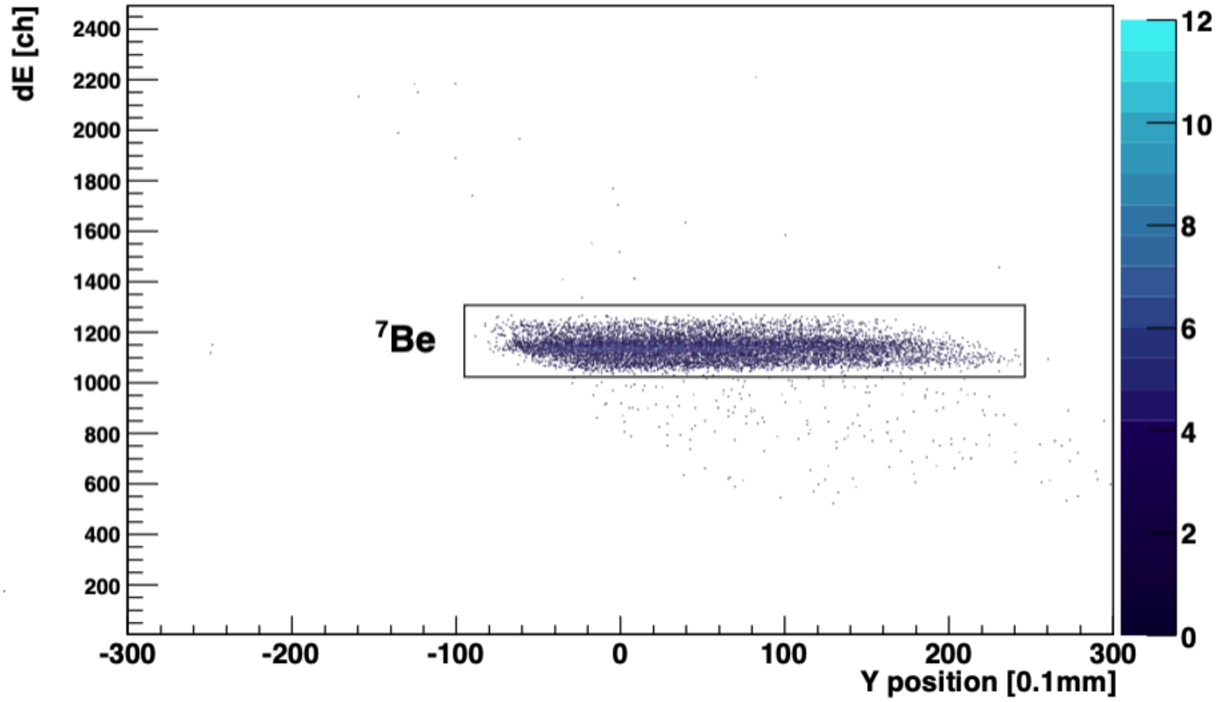

Figure 9.2: Particle identification of the beam produced by MARS during the ^{7}Be beam development. The beam was almost entirely composed of ^{7}Be and had very few contaminants.

severely limited by what the detector could handle, was between 100 and 800 events per second.

9.2 Texas CsI Array for Astrophysical Measurements (TexCAAM)

In order to measure the sub-α threshold state, especially in a region with multiple states with similar energies, γ-ray spectroscopy is required. To accomplish maximal detection efficiency, a novel γ-ray detector array was designed and constructed. The Texas CsI Array for Astrophysical Measurements (TexCAAM) consists of 32 CsI(Tl) detectors surrounding a ^{6}Li target (95% enriched) (Figure 9.4 and 9.5). CsI detectors were chosen to reduce costs as the detectors were repurposed from other projects. The solid angle coverage of the CsI is $\sim$90.5% of 4π. The ^{6}Li was backed by a single 1500 μm Micron Si detector. The Si detector was then backed by a veto that consists of a small array of 10x10x10 mm^3 EJ-200 plastic scintillators which were coupled to an array of Hamamatsu S13360 multi-pixel photon counters (also referred to as Si photomultipliers (SiPMs)). SiPMs were chosen because traditional PMTs cannot withstand the vacuum environment. The bond between the photocathode and the PMT housing can leak during the stress of vacuuming. As a result, the PMT will not function properly and eventually break. SiPMs are not affected by vacuum, which makes them ideal for light collection in vacuum environments.

TexCAAM as a whole is enclosed in a grounded $\frac{1}{8}$"-thick aluminum box in an effort to suppress light pollution and DAQ noise (Figure 9.4). To reduce the background from natural radiation, cosmic rays and also beam-induced background, TexCAAM was enclosed in a layer of lead bricks. Since the Momentum Achromat Recoil Separator (MARS) cannot support the weight of both TexCAAM and the lead bricks, a support structure was designed and built to support the total weight (Figure 9.3).

9.2.1 CsI for γ-ray Detection

The core function of TexCAAM is γ-ray spectroscopy. Maximal solid angle coverage is required and to achieve this, an array of 32 CsI detectors were assembled in a box shape that covers $\sim$90.5% of the total solid angle with respect to the target. Each CsI detector has an integrated preamplifier that produces a signal that is routed to one of two patch boards for cable management purposes. The mapping of the CsI detectors is shown in Figure 9.6. The patch boards relay the signals to a transition board that is designed to circumvent the need for openings in the aluminum shielding. The transition board was originally developed for use with the Texas Active Target (TexAT) [108] and was repurposed for use with TexCAAM. The signals are further routed to the data acquisition system.

9.2.2 Target Arm

A ^{6}Li target poses logistical issues as it can oxidize very quickly. The target must be mounted on the target arm and placed in the beam pipe with little to no oxidation in the lithium. Therefore, the target arm was designed to allow easy and quick installation as well as to support the Si and SiPM detectors behind the target, creating a singular array of the detectors and the target (Figures 9.7 and 9.8). The detectors are biased and readout via two vacuum-grade SHVs and one vacuum-grade BNC connector located in the target arm flange.

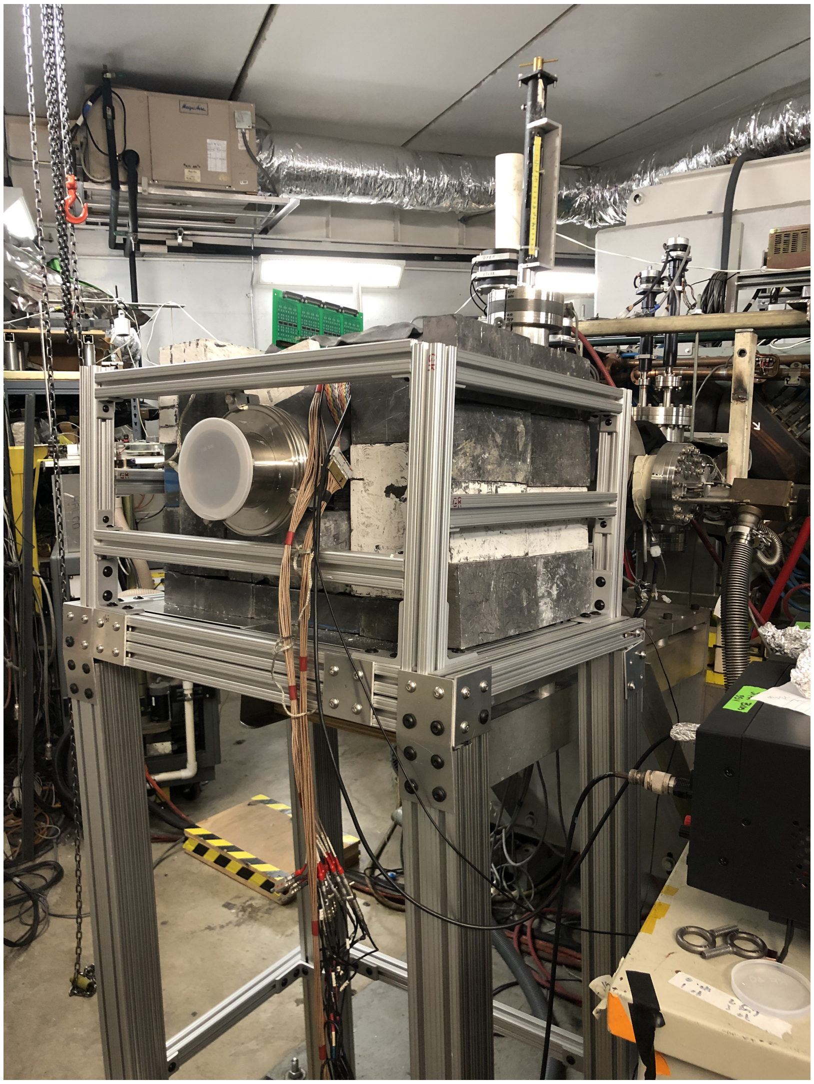

Figure 9.3: MARS is unable to support the weight of TexCAAM with the addition of the lead brick shielding. In order to attach TexCAAM to MARS, a custom support was designed and built to hold TexCAAM during experiments. Depicted is the support system constructed for TexCAAM. Here, TexCAAM is installed on the end of MARS and is surrounded by the lead bricks.

9.2.3 ^{6}Li Target

Creating the ^{6}Li target is non-trivial. Lithium oxidizes rapidly, which can easily combust in large quantities. Extra precaution should be taken to transport and work with the target in pure nitrogen or argon environments.

The target thickness, ~ 50 μm, was specifically chosen to stop the beam in the back third of

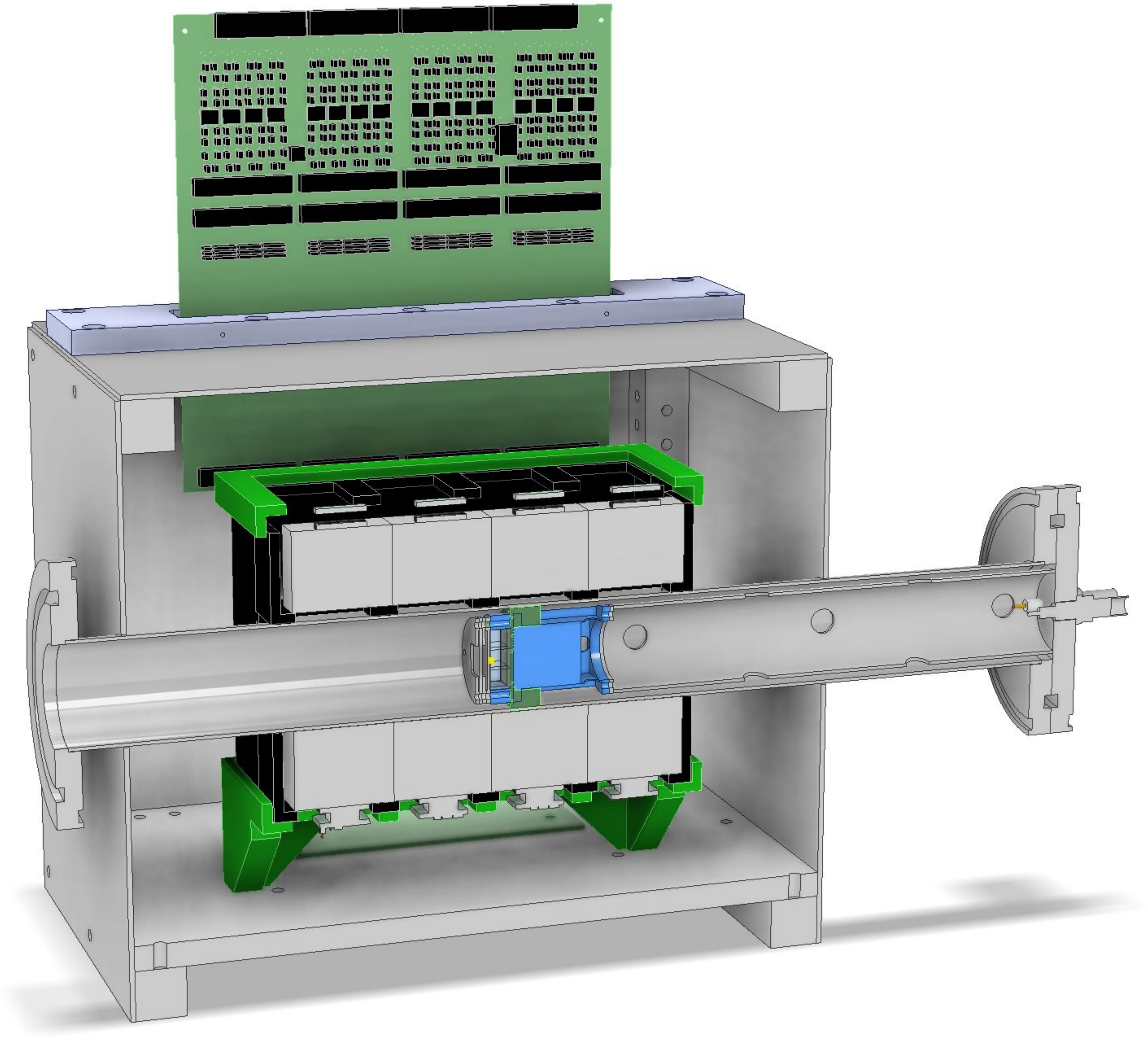

Figure 9.4: A cut-away CAD drawing of TexCAAM that reveals its inner structure. The 32 CsI detectors are tightly grouped around the beampipe and are held together via 3D-printed support structures. The beampipe intersects TexCAAM and holds the target arm. The end of the target arm sits in the center of the CsI array, maximizing the solid angle coverage of the CsI detectors. The target arm consists of the target, the Si detector, and the SiPM/scintillator array.

the target. In order to make the target, a 90% pure rock of ^{6}Li is taken and rolled into a foil. The lithium is held up by a sandwich of machined metal supports. In order to work with the ^{6}Li in a

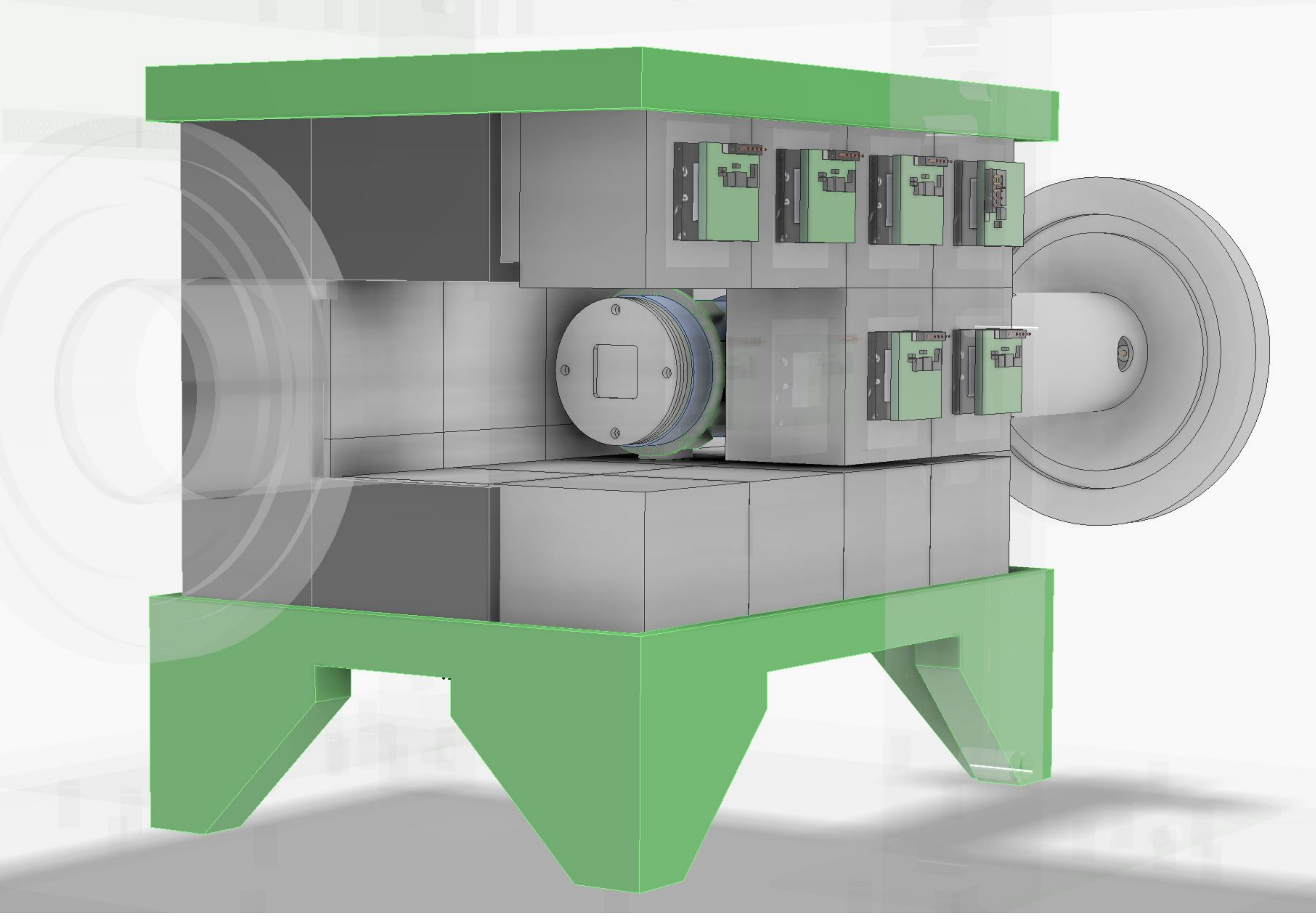

Figure 9.5: A second CAD drawing showing an alternative view of the inside of TexCAAM. The beampipe, the aluminum box, and two CsI detectors are transparent to show how the target sits inside of the CsI array.

pure nitrogen or argon environment, all work was conducted in a glovebox. The target was then installed into TexCAAM in a portable glovebox.

9.2.3.1 Target Thickness Calculations

In order to determine the appropriate thickness of the target, Stopping and Range of Ions in Matter (SRIM) (more specifically Transport of Ions in Matter (TRIM)) calculations [109] and

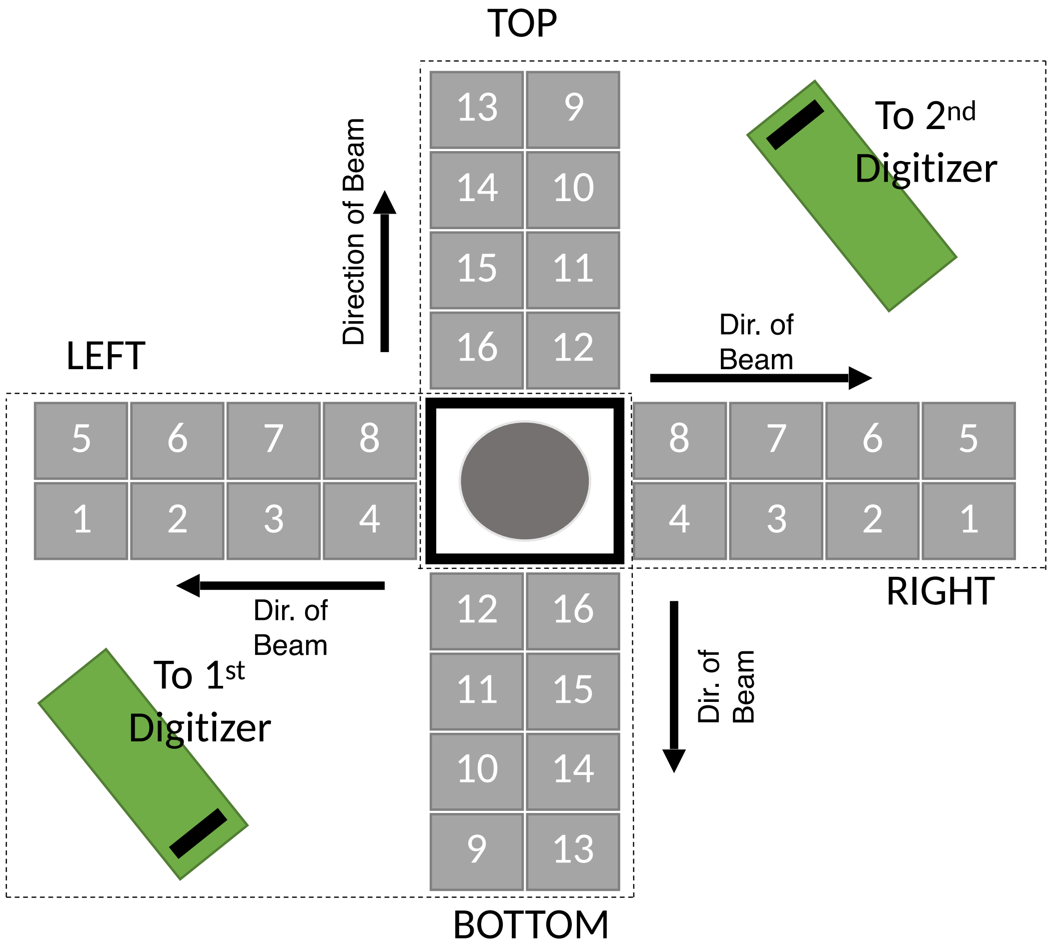

Figure 9.6: A schematic showing the orientation of the CsI detectors in TexCAAM. It also shows the two patch boards which transfer the CsI signals to the transition board.

LISE++ calculations [110] were conducted. LISE++ calculations were used to determine the appropriate beam energy for the reaction of interest. The desired beam energy was used in SRIM to determine the appropriate target thickness. The target thickness is specifically chosen to be thick enough to stop the beam (ideally in the last third of the target, Figure 9.9) while being thin enough to allow product deuterons to pass through (Figure 9.11) without large energy losses or angular straggling (Figure 9.10). In general, the target thickness is usually calculated to be on the order of 50 μm.

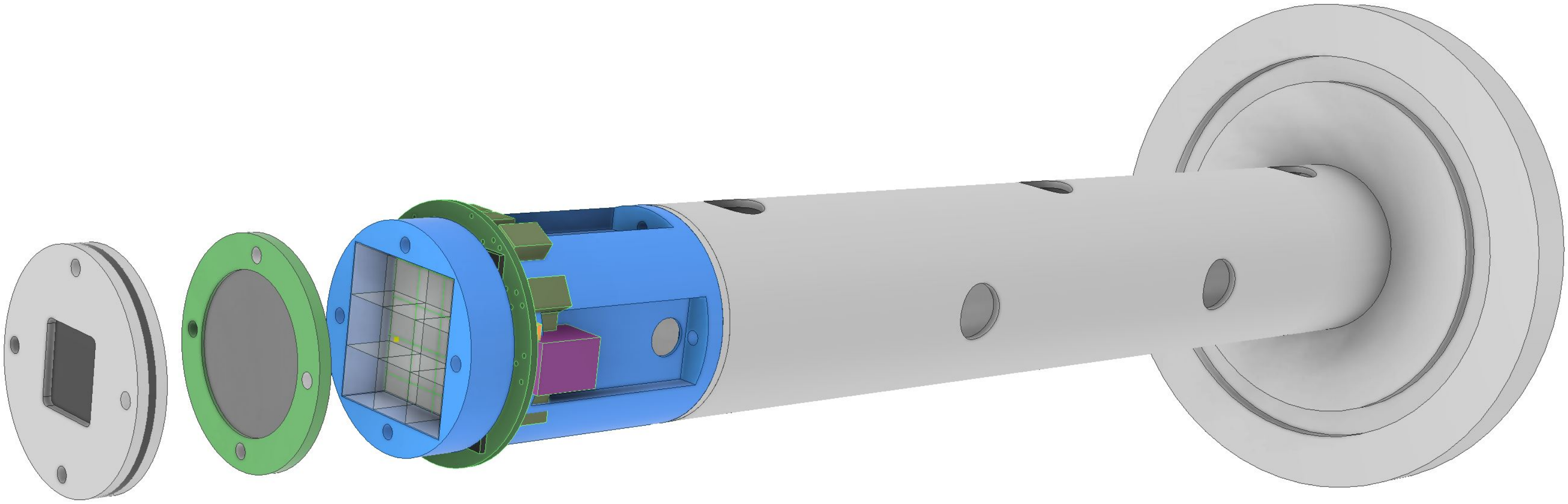

Figure 9.7: A CAD drawing of the target arm. The drawing is ‘blown up’ to clearly show each of the components of the assembly. The target ‘sandwich’ holds the lithium target and is directly backed by the Si detector. Behind the Si detector sits the scintillator array which is coupled to the array of SiPMs. Each part of the assembly is secured to the target arm prior to installation, allowing for quick installation in order to preserve the lithium target.

9.2.3.2 Production of ^{6}Li targets:

In order to make a ^{6}Li target of the desired thickness (around 50 μm) an array of items is required. The required items are a glovebox, a 99%+ pure N_2 or argon gas source, a metal roller (a 130MM Flat ULTRA Series X-DRIVE Direct Drive Rolling Mill), a scientific scale (Figure 9.12), a solvent (petroleum ether), ^{6}Li rock (Cambridge Isotope Laboratories LLM-827), thin high-density metal such as titanium, diffusion oil, calipers or a precise ruler, a portable glovebag (Figure 9.13), and a variety of tools such as plastic knives and tweezers. Purging should be done gradually as air may be trapped in places such as electronics (wire insulation) and poorly sealed containers. Ideally, this process should span 24 hours. If the glovebox isn’t fully purged, the lithium will oxidize.

Once fully purged, it is then safe to cut the ^{6}Li rock into small, thin pieces. Pure ^{6}Li is easily malleable and can be cut with a blade or a knife. The small pieces of ^{6}Li should be sufficiently coated in diffusion oil before continuing. The original coat of oil that the lithium is shipped with

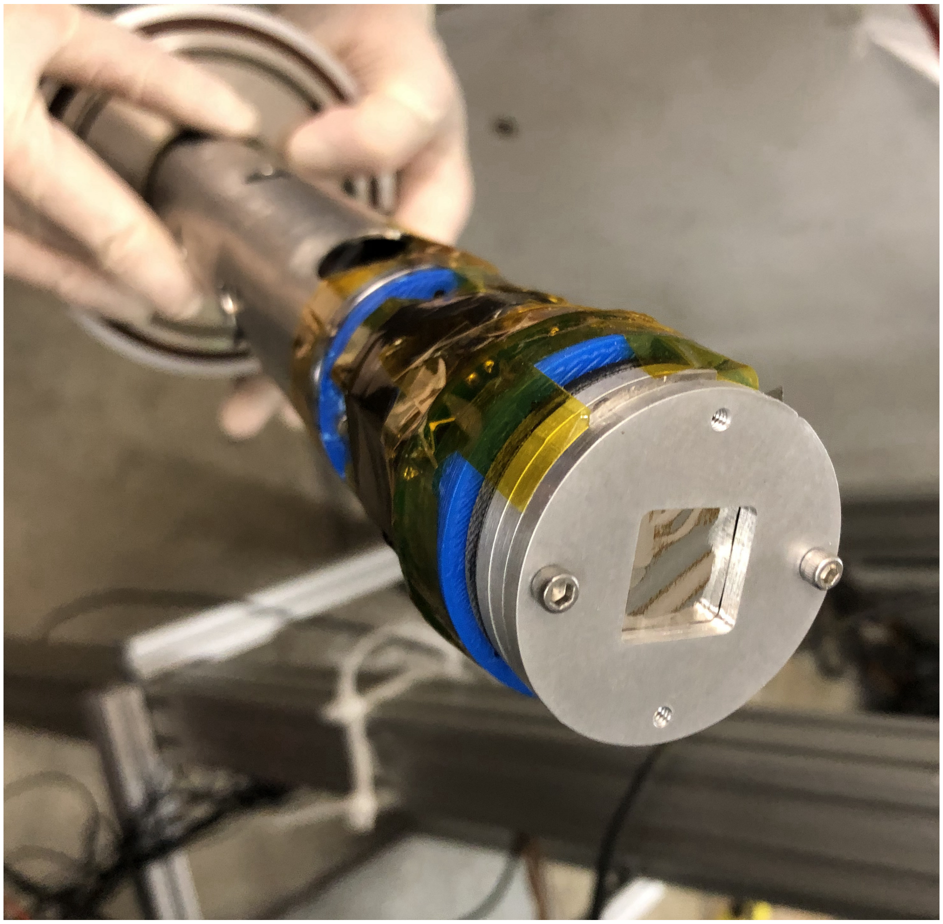

Figure 9.8: Image of the completed target arm assembly. Various parts are reinforced with Kapton tape to assure nothing moves while out gassing. The top most part of the assembly is a degrading window which reduces the energy of the beam to the desired energy. Just behind is the lithium target that is backed by the Si detector and scintillator/SiPM arrays.

may not be sufficient and more may need to be applied. The coated sliver of ^{6}Li should be placed inside of the dense metal sandwich. The sandwich can be run through the metal roller, starting at a very coarse setting that compresses the sandwich minimally. The rollers should be incrementally tightened very slowly. As the sandwich compresses, the lithium inside will want to stick to the metal sheet surrounding it. In order to prevent this as much as possible, the lithium should be frequently coated in diffusion oil.

In order to estimate the thickness of the lithium, the surface area of the ^{6}Li should be measured as precisely as possible. Cutting the lithium into easy-to-measure square pieces may be beneficial.

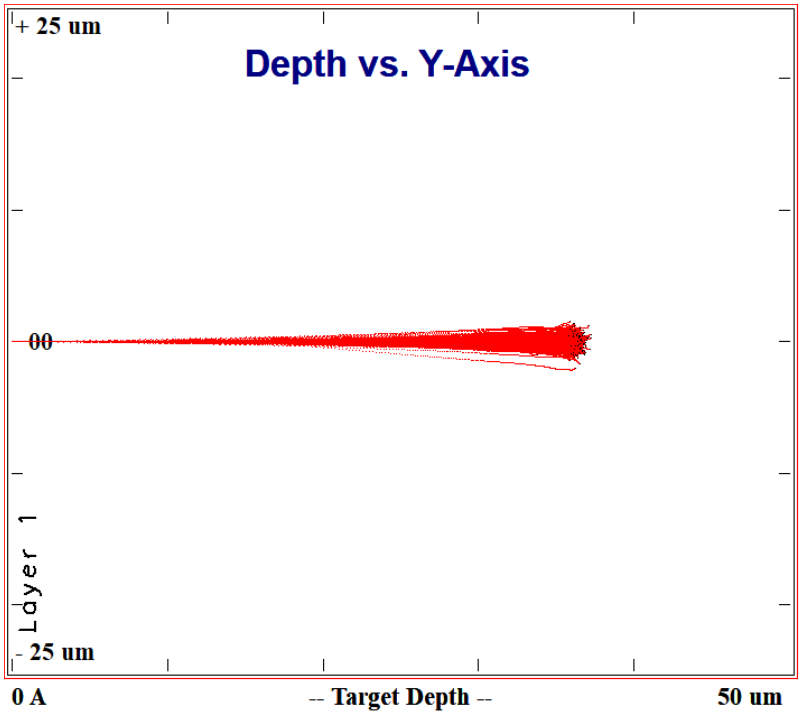

Figure 9.9: SRIM simulation for a ^{7}Be beam in a ^{6}Li target. This particular reaction primarily occurs in the last third of the target with only a small amount of angular straggling. The target in this simulation is set to 50 μm which is designed to stop the beam ($T_{beam} = 8$ MeV) well before the end of the target while thin enough to allow product deuterons to pass through the remainder of the target and enter of the Si detector located behind.

After removing the diffusion oil from the ^{6}Li, it can be weighed with the scientific scale. Since the density of lithium is known, the two pieces of information can be used to determine the average thickness of the target produced. The thickness of the target will not be completely uniform, but the thickness at a given location cannot be probed inside of the glovebox and would require energy-loss measurements to accurately determine. Once the target thickness is acquired, the targets must be kept in the nitrogen or argon environment to prevent oxidation (Figure 9.14 a). The lithium film will also be fragile so it is safest to store the target with diffusion oil between two glass slides.

The same diligence is required while transporting the target to TexCAAM. Since the target is produced in an inert gas environment, the target should also be transported in the same gaseous environment. Ideally, the target can be transported in a mobile glovebag. Prior to transportation, the target may be placed inside of its frame (Figure 9.14 b). At the location of TexCAAM, the target

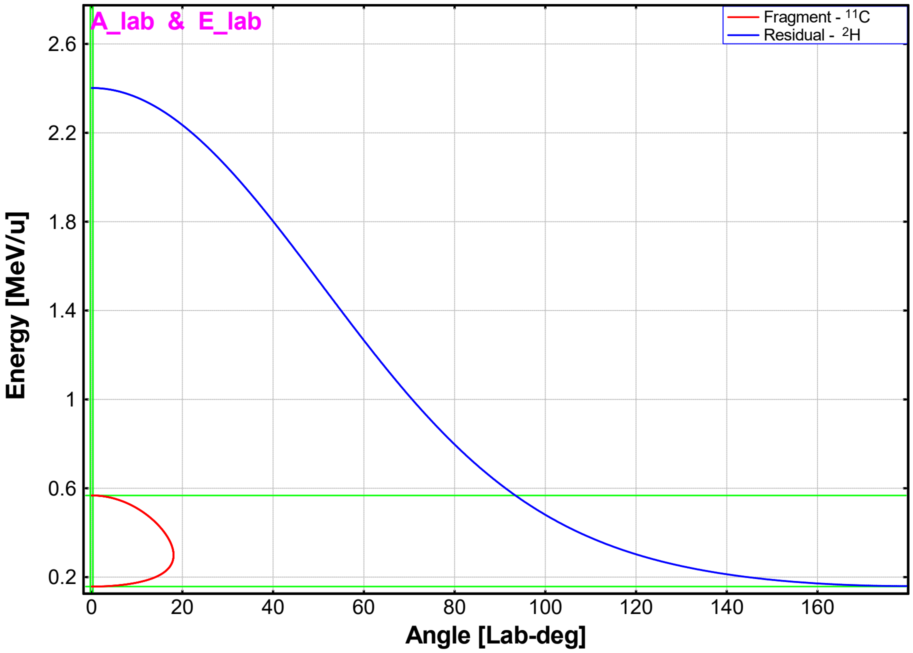

Figure 9.10: LISE++ reaction kinematics calculations for the products of the ^{7}Be(^{6}Li,dγ)^{11}C reaction, specifically feeding the $\frac{3}{2}^{+}$ state at 7.4997 MeV. The (blue online) line is the product deuteron which is very forward angled and has a significant amount of energy after the reaction. The heavy ion product (^{11}C) is completely focused at forward angles and maintains a significant amount of energy as well.

can be installed on the target arm. This installation should be done inside of a glovebag, which should be connected to the beamline and backfilled with nitrogen coming from the beamline. Once installed on the target arm, the entire target arm can be installed into the beamline.

Pin-holing effects can be substantial and need to be probed with the beam. By slowing the production process and insuring adequate diffusion oil, pin-holing can be minimized. Targets have been produced with few enough pin-holes to produce a few counts per second entering the Si detector from a 10^6 pps beam.

9.2.3.3 Si Detector and Veto

Due to the likelihood of being overwhelmed with background radiation producing an undesirable trigger rate when the CsI detectors are used alone, the target is backed with a Si detector and an array of plastic scintillators coupled to an array of SiPMs. Deuterons are expected to be forward

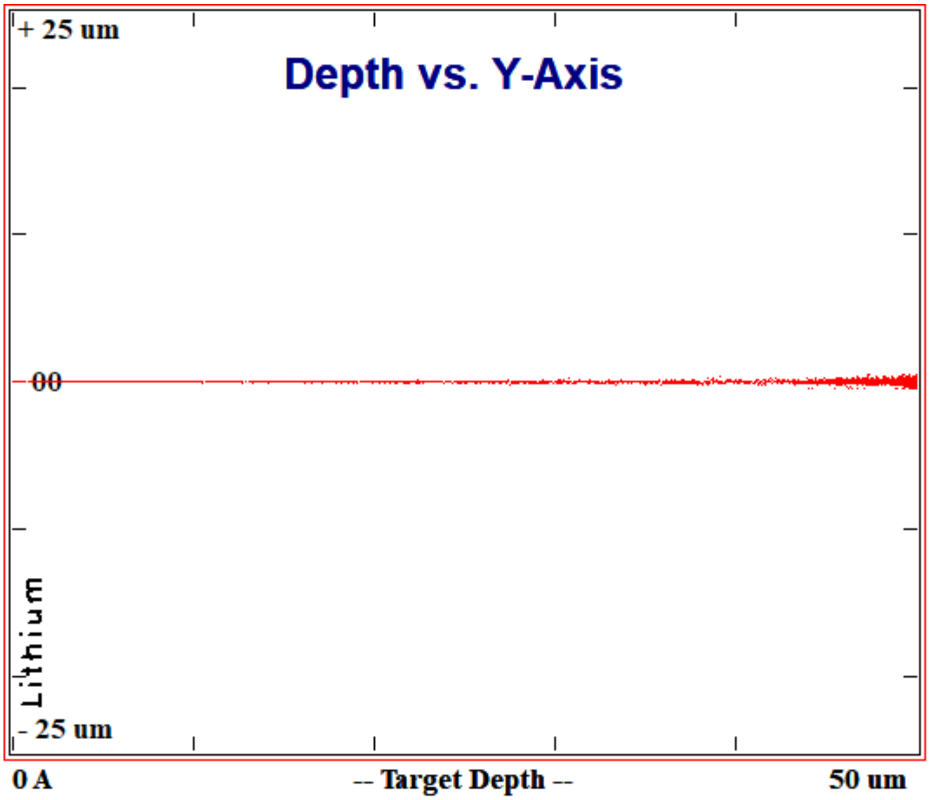

Figure 9.11: SRIM calculations for the energy loss of product deuterons passing through the target. While it may only see a small section of the target, a large target thickness was used to determine if a deuteron can pass through in the case that the reaction occurred immediately.

angled (Figure 9.10), pass through the remainder of the target, and be detected by the Si detector. Since the energy of the deuterons coming off the reaction for the specific state of interest does not exceed certain maximum value (6 MeV for the 7.5 MeV state) and are limited by the very small cross section at low energies, the energy range of deuterons can be used as a gate for the γ-rays. Moreover, once the reaction is identified using a γ ray, fixing the reaction Q-value, the energy of a deuteron in the Si detector indicates the beam energy at which the reaction was produced and hence the c.m. energy of interaction. Therefore, the Si detector can be used as a gate for the γ rays. Higher-energy deuterons and protons are expected to enter the Si detector from various other reactions. While the Si detector is thick, 1500 μm, it is expected that protons and higher energy deuterons will punch through.

In order to remove the events where particles punch through the Si detector, the Si detector is

Figure 9.12: An image of the interior of the glovebox. At the top is the scientific scale and at the bottom is the electric metal roller used to create the lithium film target.

backed by an array of plastic scintillators to act as a veto. Any signals that enter the veto detector will be rejected in the analysis.

9.2.4 GEANT4

GEANT4 simulations were carried out to estimate the experimental data. The TexCAAM geometry was recreated in GEANT4 (Figure 9.15). For α-transfer reactions, a rare isotope beam was produced. The initial beam position was randomly sampled to give an accurate beamspot according to what was achieved in MARS during beam development. The simulation includes both the β decay of implanted beam ions and the α-transfer reactions between the incident beam and the target. All energetically allowed excited states in the heavy product were included and the states


Figure 9.13: An image of the portable glovebag that is essential to the transportation and installation of the target into the beamline and TexCAAM.

were populated randomly with equal probabilities. PENELOPE libraries in GEANT4 were used to handle the γ ray physics.

Simulations were constructed in GEANT4 to estimate the γ-ray efficiencies for the ^{11}Be β decay. A ^{11}Be isotope was produced at the target location of TexCAAM and the β-decay branches were modeled. The states of ^{11}B were accurately filled and the γ-ray cascades were accurately reconstructed. The β-decay simulations were conducted to compare to experimental ^{11}Be β decay data and confirm the γ-ray efficiency curve for high energy γ rays.

Monoenergetic γ-ray simulations were also conducted in GEANT4 to determine the γ-ray efficiency of TexCAAM. A series of energies were simulated between 1 and 9 MeV (the energy

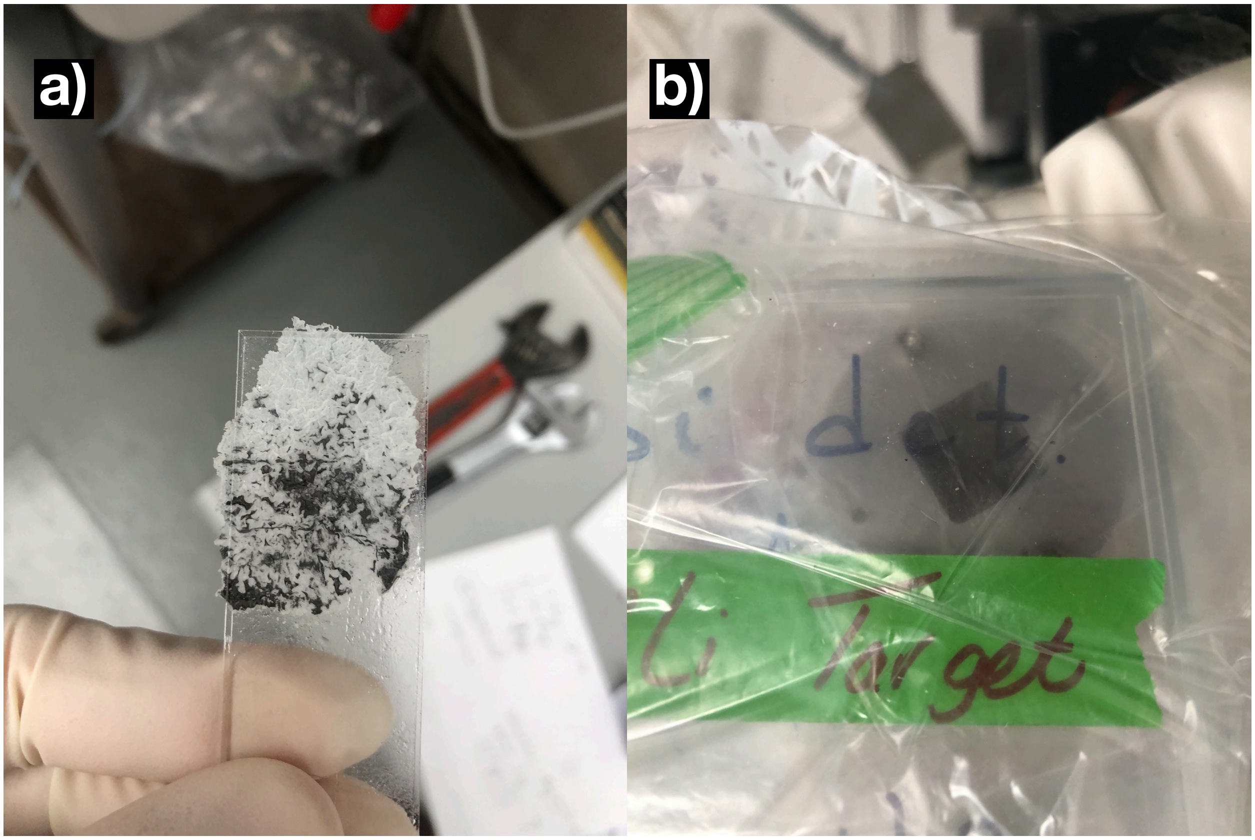

Figure 9.14: a) An image of an improperly stored lithium target that has undergone oxidation inside of the glovebox. Any exposed part of the lithium outside of the confinement of the slides will allow oxidation creep in and react with the entirety of the target. b) An image of a target that was produced and installed in the ‘target sandwich’. The target is stored in a clear plastic box and multiple press-seal bags, awaiting transportation and installation.

region of interest for TexCAAM) to determine the γ-ray efficiency for each energy chosen. The monoenergetic γ-ray source was produced at the target location of TexCAAM and emitted γ rays isotropically.

Along with the monoenergetic γ-ray simulations, a Geant4 simulation was created to simulate a ^{60}Co source. The source was placed at the target location and the γ-ray cascades were reproduced. These simulations were conducted to estimate the effect of anisotropy from the ^{60}Co source and compare to experimental data to determine the γ-ray efficiencies at 1.1 and 1.3 MeV.

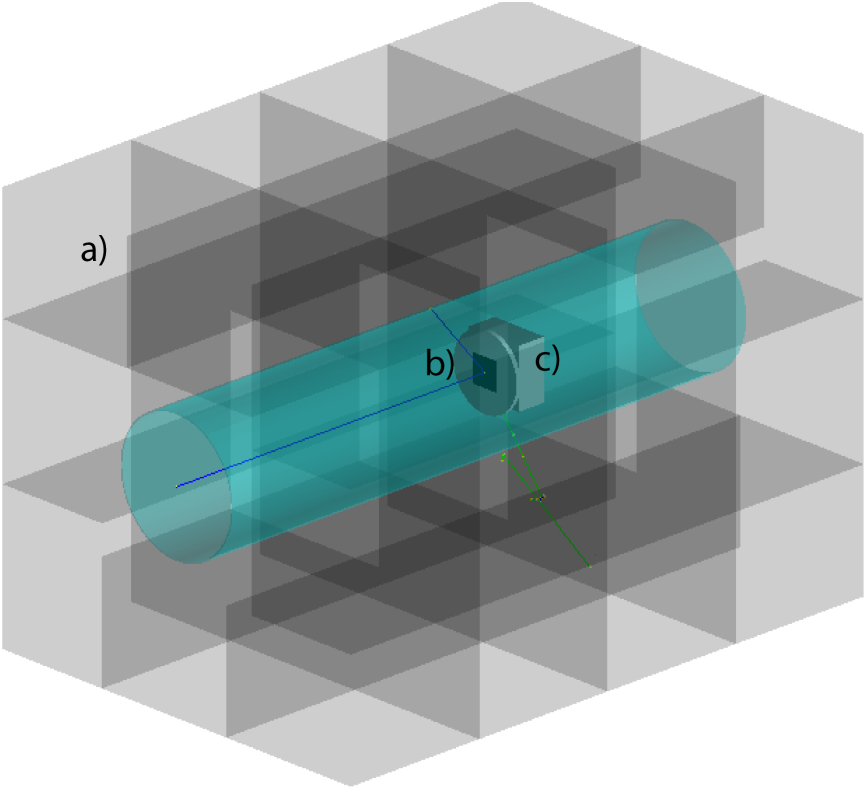

Figure 9.15: A screenshot of the Geant4 simulation of TexCAAM for the ^{7}Be(^{6}Li, $d\gamma$)^{11}C experiment. a) The semi-opaque cubes represent the CsI scintillators used for γ-ray spectroscopy. b) The ^{6}Li rolled target inside of the frame. c) Both the Micron Si detector and the plastic scintillators that back the Si detector.

9.3 Data Acquisition

The data acquisition system (DAQ) consists of three 16-channel STRUCK SIS3316 digitizers which are read out via CycApps software. Two of the STRUCK digitizers were fed via the transition board and read out all 32 of the CsI channels. The third digitizer read out the Si detector and the SiPMs. The three STRUCK digitizers were controlled by a STRUCK SIS3104 controller. The data was recorded in GOOSY format [111]. Data acquisition live time was determined using an external CAEN V830 scaler and an Ortec 448 research pulser.

The three SIS3316 digitizers were coupled via a front panel low-voltage differential signaling (LVDS) bus to synchronize operation between the digitizers. The digitizer clocks were synchronized along with trigger/vetos, timestamp clears, and sample controls. Sample logic busy and address threshold flags were shared as well. Coupling the three digitizers allows the user to synchronize the clocks, which is necessary to determine timing gates for β-γ, γ-γ, and β-γ-γ coincidences, as well as the time of flight between the Si detector and the SiPMs.

9.3.1 STRUCK Moving Average Window Trapezoidal Filter

The STRUCK DAQ is able to determine the pulse amplitude and timing for each of the detector signals. STRUCK takes the raw waveform and applies a moving average window (MAW) trapezoidal filter in order to determine the amplitude and timing. The trapezoidal MAW filter rises according to the *peak timing* parameter and plateaus according to the *gap timing* parameter. Normally, the trapezoidal filter is asymmetric about the time axis, however, a decay time, τ, correction can be applied to form a symmetric trapezoidal MAW, like the one shown in Figures 9.16 and 9.17. The trigger threshold determines the trigger start time. The trigger gate has a variable width which is set as a STRUCK parameter. The energy pickup index is determined by the *peak timing* parameter and half of the *gap timing* parameter. The energy pickup index determines the pickup energy, i.e. the energy at the half-*gap* width rather than the max energy. At the full *gap* timing the max energy is recorded [112]. For TexCAAM, the max energy is read out.

STRUCK digitizers can also record full waveforms with a maximum sampling rate of up to

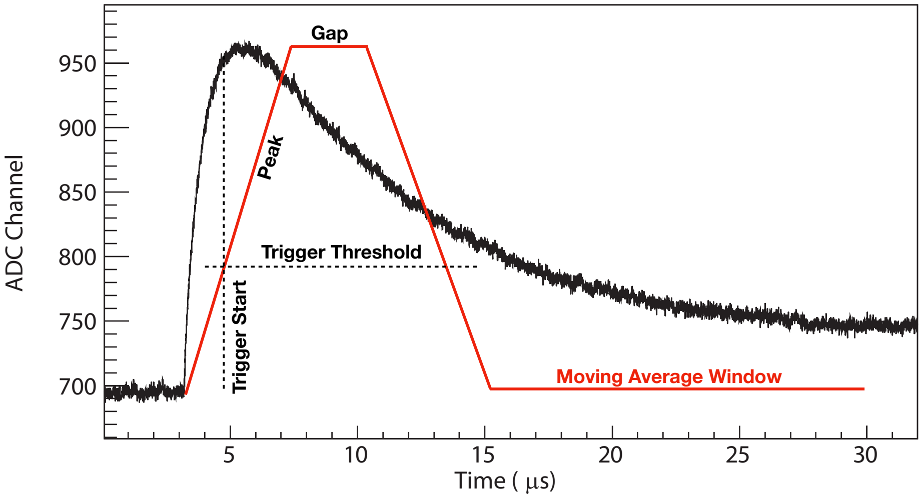

Figure 9.16: A CsI waveform recorded with STRUCK with a trapezoidal MAW filter superimposed (red online). The trapezoidal filter serves as a visual guide and is not the actual filter applied to the signal. The *peak* and *gap* components of the MAW filter are labeled. The trigger threshold is shown and the trigger start time corresponds to the apex of the signal.

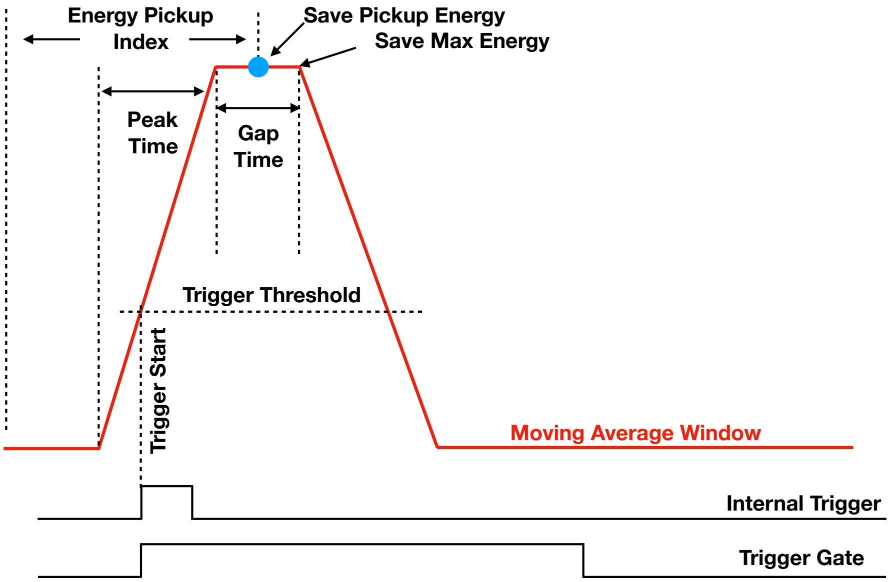

Figure 9.17: The trapezoidal MAW filter from Figure 9.16 is broken down even further. The internal trigger, along with the trigger gate, are shown in relation to the trigger starting point on the MAW filter. The energy pickup index is determined by the *peak timing* parameter and one-half of the *gap timing* parameter. At the end of the energy pickup index, STRUCK saves the pickup energy (blue dot online). At the end of the full *gap timing* gate, the maximum energy is recorded.

250 MHz (4 ns timing resolution). Saving the full waveforms allows for more complex offline analyses, such as PSD in the Si detector.

10. DATA ANALYSIS AND DETECTOR CHARACTERIZATION

10.1 TexCAAM Analysis Tools

TexCAAM analysis tools is a package that allows TexCAAM users to easily work with the data that is taken during experiments. TexCAAM analysis tools has three functions: data reduction, theoretical calculations, and GEANT4 simulations (Figure 10.1). The main function of TexCAAM analysis tools is analyzing raw data taken by TexCAAM. The analysis tools will automatically reduce raw data and copy it to the online server where the reduced GOOSY [111] files will be converted to histograms. Histogram creation utilizes a number of techniques including addback reconstruction, β-γ-γ coincidences, and Si PSD.

10.1.1 Reaction Location Reconstruction

Using reaction kinematics, the reaction location can be reconstructed. Since the γ-rays and the light product particles are directly detected and their energies are found, the reaction location can be deduced. In practice, the location inside of the target is varied and the energy loss of the beam is found for each of the locations. At each location, the beam energy is then used to determine the heavy and light product particle energies. Once the detected light product particle energy is reconstructed, the reaction location is determined (Figure 10.2).

10.1.2 Doppler Correction

For the reactions of interest, the light ejectile particle (deuteron) and the heavy recoil ion are comparable in mass. Therefore, the deuteron will not take all of the kinetic energy from the reaction and heavy recoil ion will not be stationary after the reaction. The motion of the heavy recoil ion will contribute a Doppler shift to the de-excitating γ-rays that are emitted. Determining the kinetic energy of the heavy recoil ion allows for Doppler corrections in the γ-ray energies. The center-of-mass (COM) energy of the reactants can be found from the beam energy, the associated reaction Q-value, and the excitation energy of the heavy recoil ion. With the heavy recoil kinetic energy, the relativistic velocity can be found (β=v/c). The relativistic Doppler effect can be calculated and a

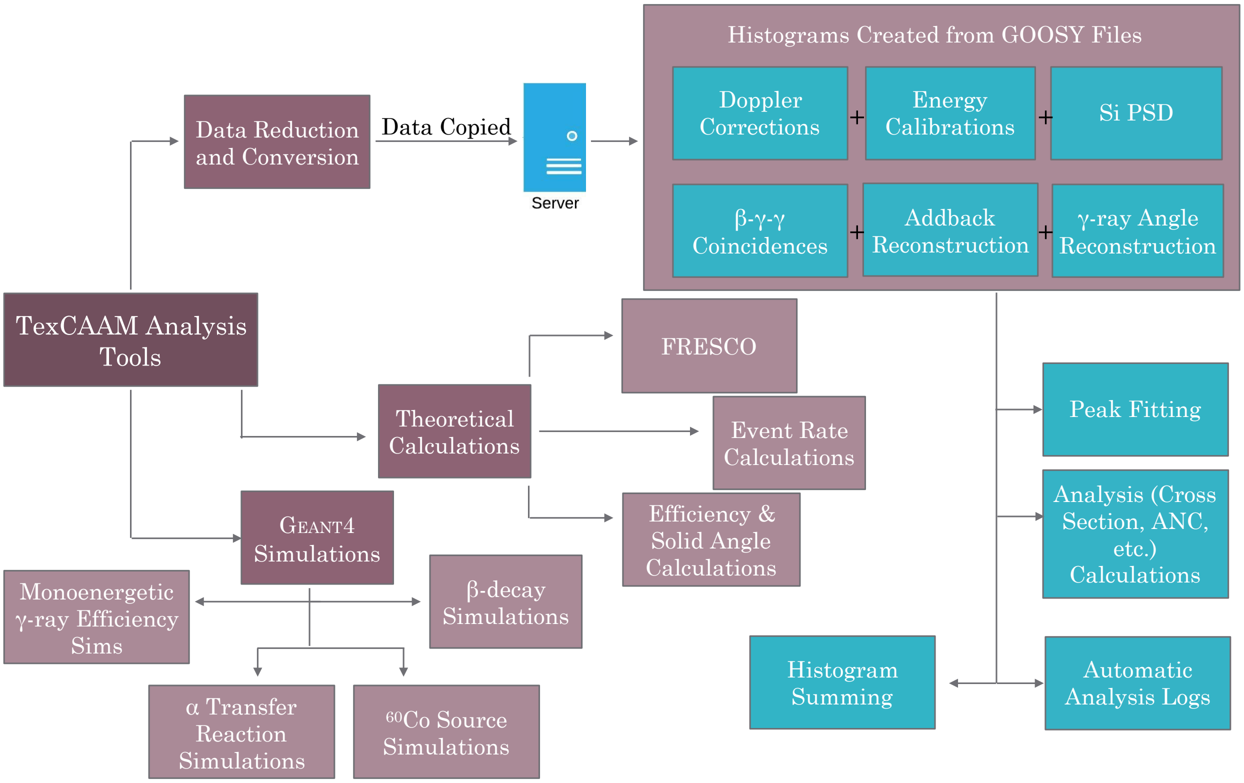

Figure 10.1: A flow chart of the capabilities of TexCAAM analysis tools. There are three main branches of the tool system: data reduction and conversion, theoretical calculations, and Geant4 simulations. The Geant4 simulations branch contains all necessary Geant4 simulations for TexCAAM including β-decay, α-transfer, ^{60}Co source, and monoenergetic γ-ray simulations. The theoretical calculations branch contains the necessary frameworks to estimate TexCAAMs detection efficiency and solid angle, estimated event rates for specific reactions, and FRESCO calculations. The third branch contains the majority of the framework. Raw GOOSY data are reduced and transferred to the online server. Histograms can be produced using an array of techniques. Peak fitting code and analysis calculations can be conducted on the produced histograms.

correction can be applied to the γ-ray energy. Doppler corrections reduce peak widths and enhance the observed γ-ray energy resolutions.

10.1.3 Si PSD

Pulse-shape discrimination (discussed in depth in Section 1.2.3.1) is widely used in neutron/γ-ray detecting scintillators to discriminate between the particles. PSD has also been demonstrated in single surface barrier detectors (i.e. Si detectors) [113, 114, 115]. In these detectors, pulse height is determined by the energy of the particle and the pulse shape is determined by the range of the

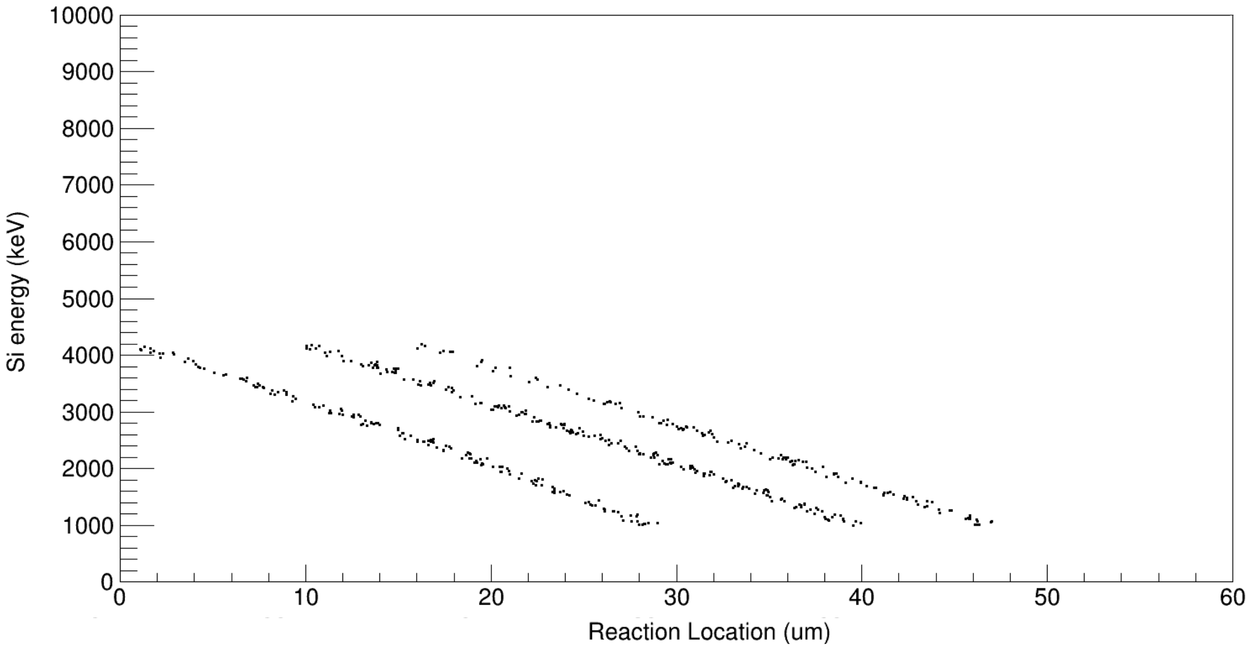

Figure 10.2: Results of reaction location reconstruction with a small data set. The three bands are from the three excited states that are populated in the ^{7}Be(^{6}Li,$d\gamma$)^{11}C reaction.

particle. The rise time of the pulse is determined by the collection time of the produced electrons and holes outside of the depletion layer of the semiconductor. The produced electrons and holes diffuse towards the depletion layer creating a tangible time difference for different ranges of a particle in the detector. Comparisons of the relative rise times for Si signals may lead to PID bands separating different particles (i.e. proton, deuterons, and tritons) as well as different nuclei (i.e. Li, Be, B, etc...). Furthermore, Si PSD has demonstrated the possibility of rejecting pile-up events and defective signals [116].

Early testing of PSD in the Si detector for TexCAAM has indicated the possibility of using PSD to distinguish particles (Figure 10.3). Two distinct bands can be observed with good separation, especially between ∼3 MeV to 10 MeV. One band is focused at lower energies where we would expect to see punch through events from particles such as protons. The other band is strongest above 3 MeV which is where we expect to observe deuterons, from the reactions of interest, stopping in the detector. Further testing is needed to verify PSD capabilities for TexCAAM.

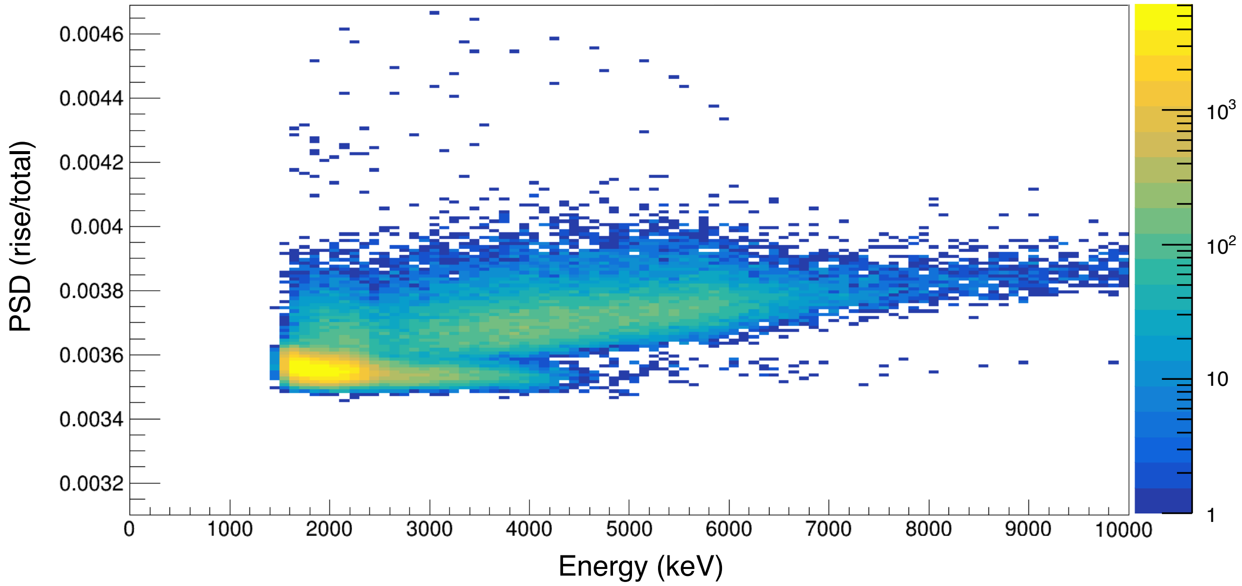

Figure 10.3: Early testing of Si pulse shape discrimination with ^{12}C(^{6}Li,$d\gamma$)^{16}O data. These tests demonstrate the possibility of using Si PSD techniques to assist future analyses.

10.1.4 γ-ray Addback Reconstruction

γ-ray addback reconstruction was incorporated in the production of the γ-ray histograms to account for multiple-crystal events. In the energy region of interest, the primary mode of γ-ray interactions is Compton scattering. The likelihood of a γ ray scattering in a CsI crystal is relatively large and the γ ray may scatter into an adjacent crystal before scattering again. Normally, this would be read out as two separate signals. However, a +/- 200 ns CsI-CsI coincidence time gate was applied to reconstruct the energy from a γ-ray interacting with two crystals. The addback reconstruction also requires that the two crystals are adjacent to one another (Figure 9.6). If both conditions are satisfied the energies are summed to produce the total γ-ray energy for the event.

10.2 Energy Calibration

Energy calibrations for the CsI detectors were performed using ^{22}Na, ^{137}Cs, and ^{60}Co sources as well as the ^{11}Be$(\beta,\gamma)^{11}$B decay. ^{22}Na β decays into ^{22}Ne and produces a 1274.5-keV γ ray during its decay. ^{137}Cs produces a 661.7-keV γ ray during its decay. ^{60}Co produces 1173.2- and

1332.5-keV γ rays during its decay. Figure 10.4 shows the decay scheme of ^{11}B. The states with the highest β feedings are the 7997.8-keV $\frac{3}{2}^+$ state, the 6791.8-keV $\frac{1}{2}^+$ state, the 2124.7-keV $\frac{1}{2}^-$ state, and the $\frac{3}{2}^-$ ground state. The γ rays used for the energy calibrations are the 7997.8-keV, the 6791.8-keV, and the 2124.7-keV γ rays. For each of the CsI detector channels, the γ-ray histograms for each of the sources were fit with one or more Gaussian functions in addition to a background estimate (Figure 10.5). The energy resolution for a single CsI crystal is generally around 10-12% at the 1 MeV region. The ADC channel number for each of the peaks was plotted against the known energy and fit with a second order polynomial to account for any non-linearity that is intrinsic to CsI detectors [117] (Figure 10.6). The energy calibrations are slightly non-linear over the energy ranges as expected.

Energy calibrations for the Si detector and SiPMs were performed with a multinuclide α source which produces energies of 3.11 MeV, 5.147 MeV, 5.474 MeV, and 5.787 MeV for ^{148}Gd, ^{239}Pu, ^{241}Am and ^{244}Cm respectively. The energy calibration trend for the Si and SiPM detectors were linear.

10.3 Absolute γ-ray Detection Efficiency

10.3.1 ^{60}Co Source

Efficiency calculations were conducted with a ^{60}Co source, both through experiment and GEANT4 simulations. ^{60}Co produces two γ rays, one at 1173 keV and one at 1332 keV. These two γ rays are a product of the same cascade, therefore they are correlated. Since they are correlated, if one is observed then the other must be observed unless it escapes without being detected. The number of coincidence events, events where both γ rays are observed, follows the equation

$$N_{Coincidence} = N_{decays} * \varepsilon_{E_1} * \varepsilon_{E_2}, \tag{10.1}$$

where N_{decays} is the total number of decays and ε_E is the efficiency at energy E. Similarly, the number of counts in each of the individual peaks follows the equation

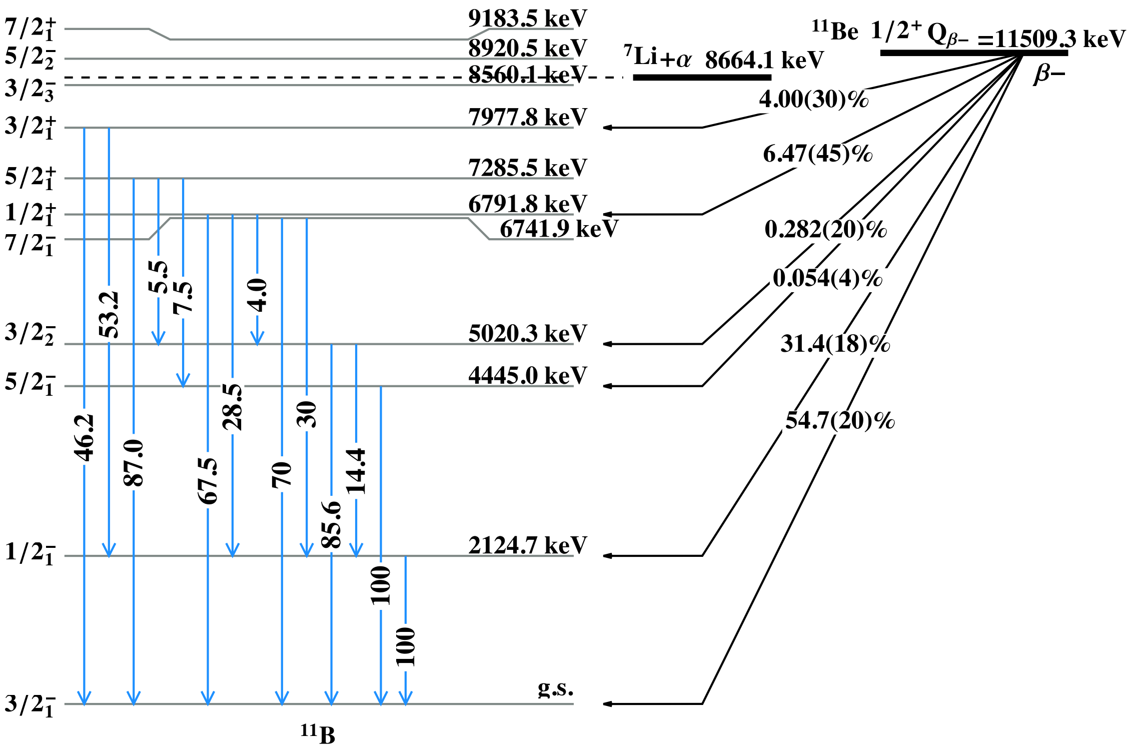

Figure 10.4: β-decay scheme for the ^{11}Be($\beta^-\gamma$)^{11}B decay. The right hand side shows the β feedings into the various states of ^{11}B accompanied by their β feeding strengths in percentage relative to unity. The blue arrows are the γ-ray transitions from a given state. The relative γ-ray transition strengths accompany each of the γ-ray transitions. The uncertainties for each of the γ-ray transition strengths were not included in order to create a legible decay scheme. Only the states populated in the experiment are portrayed and higher energy states are omitted from the decay scheme. The data that were used to construct this decay scheme are from [13].

$$N_E = N_{decays} * \varepsilon_E \tag{10.2}$$

The number of counts in each of the peaks is directly dependent on the number of events and the detection efficiency at that energy. By taking the ratio of equations 10.1 and 10.2, the efficiency of one energy can be determined with

$$\varepsilon_{E_1} = \frac{N_{Coincidence}}{N_{E_2}}, \tag{10.3}$$

where E_1 is one γ-ray energy and E_2 is the other γ-ray energy. $N_{Coincidence}$ was determined with

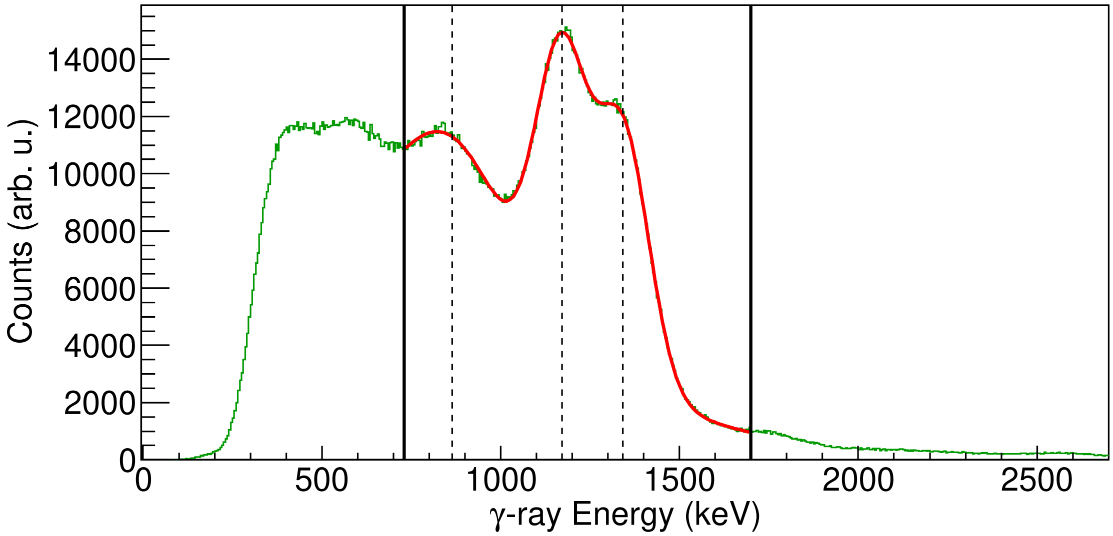

Figure 10.5: A triple Gaussian peak fit, in addition to a background estimation, for ^{60}Co source data. The fit has a χ^2/ν=1.69 and encompasses the two ^{60}Co photopeaks (1173.2 and 1332.5 keV) as well as their respective Compton edges. This histogram was produced by summing the signals of all 32 CsI crystals. The energy resolution for the sum of the detectors is approximately 14.5 and 13% for the 1.1 MeV and 1.3 MeV peaks, respectively. The dashed vertical lines show the centroid locations for each of the Gaussians and the solid vertical lines show the fit range.

γ-γ coincidences (Figure 10.7). The value is simply the total number of events where both the 1172 keV and 1332 keV γ rays are observed. The γ-γ coincidence gates are discussed in Section 10.3.2.4.

GEANT4 simulations were then performed for a ^{60}Co source to estimate the effect of anisotropy of the decay. It was found that the anisotropy has about a 2% effect on the efficiency and was therefore deemed to be a second-order effect. The simulated ^{60}Co efficiencies were found to be 36.7(9)% and 33.6(9)% for 1173 keV and 1332 keV, respectively. GEANT4 γ-ray efficiency uncertainties were determined via the statistical uncertainty from the number of simulated events ($\propto \frac{1}{\sqrt{N}}$). The ratio of the efficiencies for the simulated ^{60}Co source ($\frac{\varepsilon_{1173}}{\varepsilon_{1332}}$=1.09(4)) and the experimental ^{60}Co source ($\frac{\varepsilon_{1173}}{\varepsilon_{1332}}$=1.09(3)) are in agreement, providing evidence in the accuracy of the γ-ray efficiencies found with the GEANT4 simulations. The average ratio between the simulated and experimental efficiencies is 0.700, which is applied as an inflation on the GEANT4 simulated γ-ray

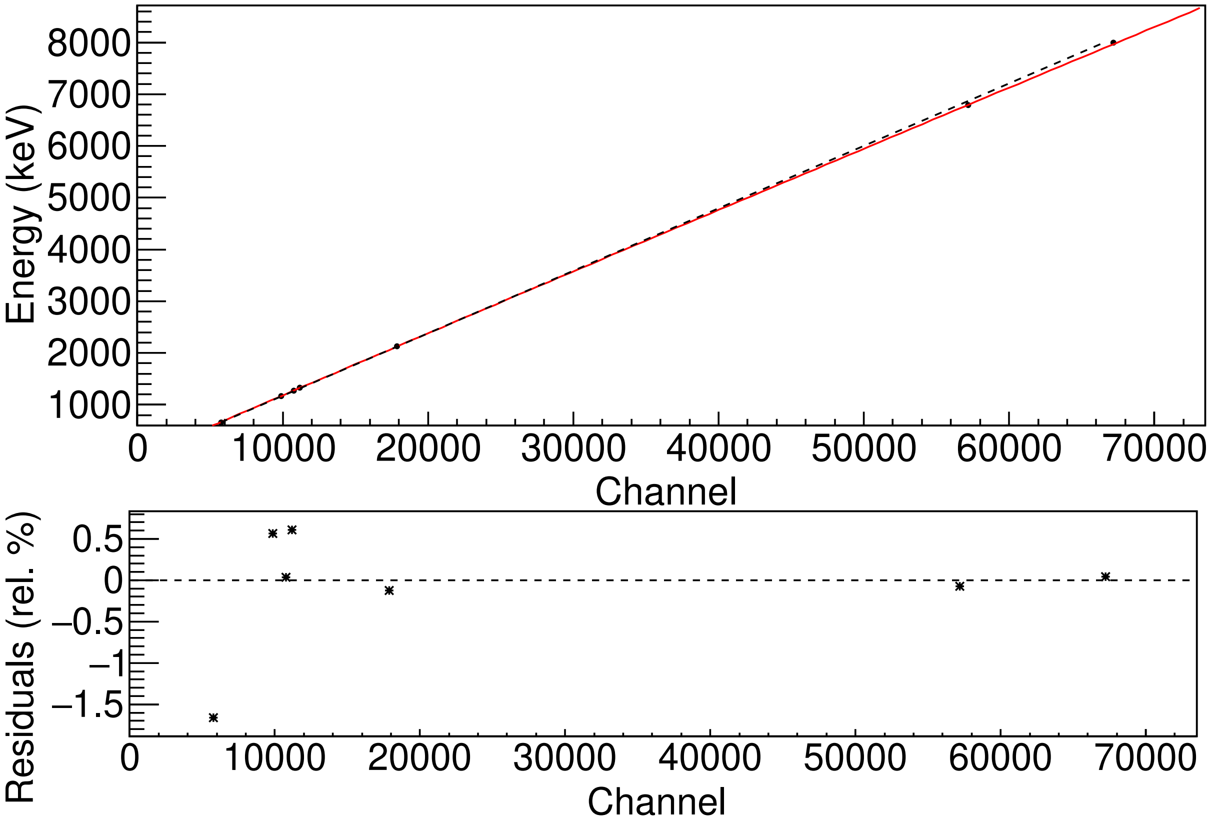

Figure 10.6: An example of the energy calibration performed for the CsI detectors in TexCAAM. Seven data points, from various source and experimental data, were used to determine the energy calibration for the energy range between 661.7 and 7997.8 keV. The data points were fit with a second order polynomial (χ^2/ν=1.89) that is slightly non-linear. The fit (red online) is compared to linearity (dashed line) and is only visibly different at higher energies. The residuals of the fit, in relative percentage, are shown in order to visualize the accuracy of the energy calibration fit. The maximum residual is approximately 1.5%.

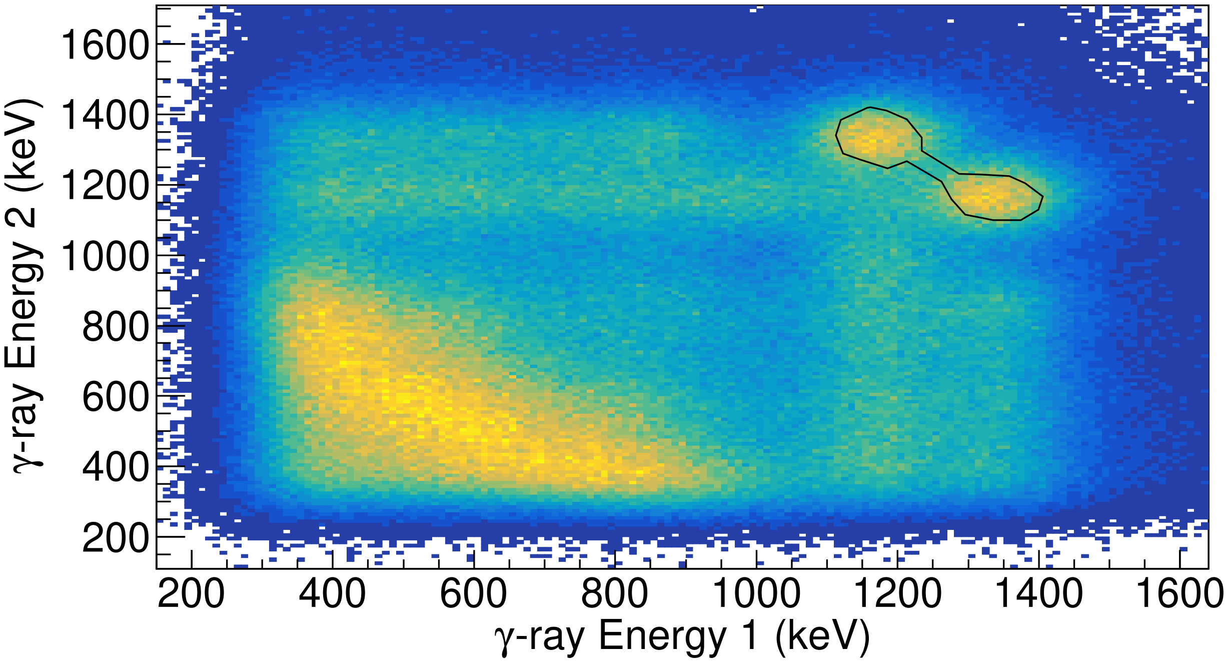

Figure 10.7: 2-dimensional CsI-CsI ($\gamma - \gamma$) coincidence histogram for a ^{60}Co source. The $\gamma - \gamma$ coincidence gate depicted in Figure 10.16 was used to determine coincidences. The γ-ray energies from one crystal are plotted against the γ-ray energies from a second crystal that is in coincidence. A strict gate was set on coincidence γ rays in order to determine N$_{coincidence}$ in equation 10.1.

efficiencies.

10.3.2 ^{11}Be($\beta^-\gamma$)^{11}B decay

In addition to the ^{60}Co study, the ^{11}Be($\beta^-\gamma$)^{11}B decay was studied to determine the γ-ray efficiencies for the energies at 2124.7 keV, 6791.8 keV, and 7977.8 keV. A ^{11}Be beam was implanted into the Si detector and populated states in ^{11}B up to the 7977.8 keV state (Figure 10.4). The β decay of ^{11}Be is well known [13], allowing us to replicate the study to determine the γ-ray efficiencies for the well fed states.

10.3.2.1 Experiment Setup

To study the ^{11}Be($\beta^-\gamma$)^{11}B decay, TexCAAM was attached to MARS with the arm raised to 5 degrees to optimize transmission of the rare isotope beam. A primary ^{13}C^{4+} beam was accelerated in the K500 Cyclotron to an energy of 30 MeV/u. A 1 mm ^{9}Be solid target was placed in the solid target ladder in MARS to induce the ^{13}C+^{9}Be reaction. ^{11}Be was produced through fragmentation with a yield of 32 ev/nC. A secondary product (^{8}Li) was produced at a rate of 3 ev/nC, implying a beam purity of approximately 91.4% ^{11}Be. ^{8}Li β decays to ^{8}Be but will only produce α particles since the decay wont populate any bound states. The product ^{11}Be beam after the solid target had a total kinetic energy of approximately 247.7 MeV ($\sim$22.5 MeV/u) and the ^{8}Li contaminant had a total kinetic energy of 191.3 MeV (23.9 MeV/u). Prior to the entrance of TexCAAM, the ^{11}Be beam was degraded to an energy of approximately 12.3 MeV/u, which is low enough to stop the beam completely inside of the 1500 μm Si detector, and the ^{8}Li beam was degraded to an energy of approximately 17 MeV/u, which will punch through the Si detector. The cyclotron ran in intervals of 30 seconds on and 30 seconds off during the course of the experiment. During the 30 seconds on, the beam would bombard the Si detector. During the 30 seconds off, the decay products (the β particles) were counted in the Si detector in coincidence with γ rays. A cycle time of 30 seconds was chosen to encompass approximately two half-lives of ^{11}Be ($T_{1/2}$=13.76 sec).

10.3.2.2 GEANT4 Simulations

As described in Section 9.2.4, the ^{11}Be($\beta^-\gamma$)^{11}B decay was simulated in GEANT4. Due to the simplicity of the decay scheme, only the γ-ray decay portion of the decay was simulated. The appropriate states were filled according to the β-decay feedings and the γ-ray cascades were recreated according to the relative γ-ray intensities (Figure 10.4). The γ-ray histogram (Figure 10.8) was fit to determine the integral values for each of the photopeaks and their corresponding escape peaks. The γ-ray efficiencies found with the simulated decay are: $\varepsilon_{2124.7}$=29.6(4)%, $\varepsilon_{6791.8}$=23.3(8)%, and $\varepsilon_{7977.8}$=23.1(17)%. If the inflation ratio found for the ^{60}Co data (0.700, Section 10.3.1) is applied, the efficiencies become: $\varepsilon_{2124.7}$=20.7(3)%, $\varepsilon_{6791.8}$=16.3(6)%, and $\varepsilon_{7977.8}$=16.1(12)%. The γ-ray efficiency uncertainties were estimated by taking the statistical uncertainties of the integral values from the fit and inflating them by the $\sqrt{\chi^2/\nu}$ of the fit.

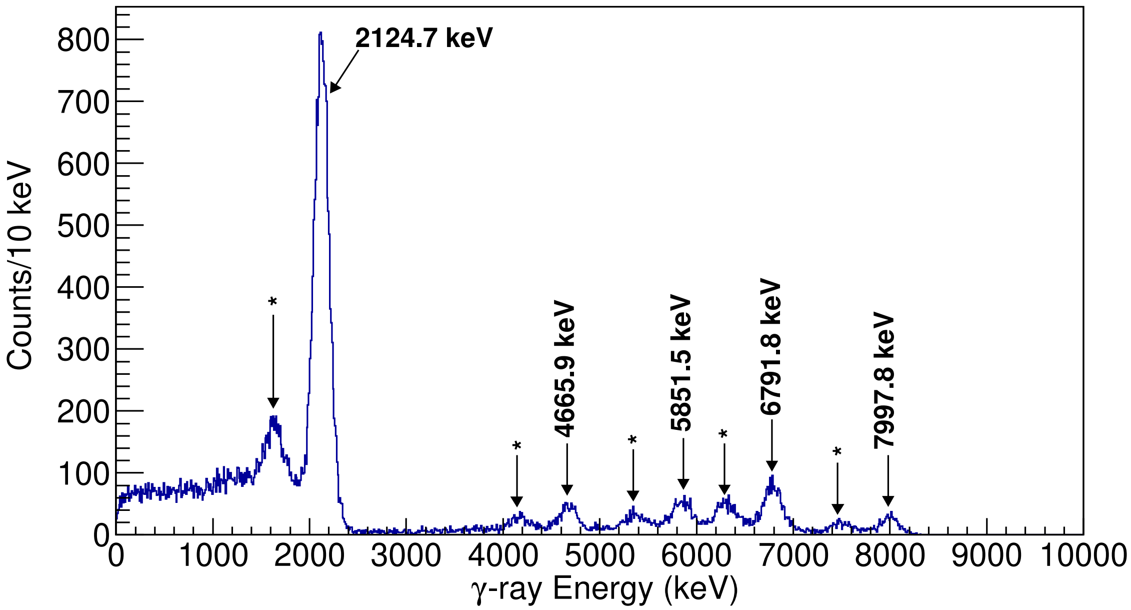

Figure 10.8: Geant4 simulation for the ^{11}Be($\beta^{-}\gamma$)^{11}B decay. The photopeaks are labelled according to their γ-ray energies and the single escape peaks are labeled with an asterisk (*).

10.3.2.3 γ-ray Efficiencies from the ^{11}Be($\beta^{-}\gamma$)^{11}B decay

The γ-ray histograms were produced in coincidence with the β-particle signals in the Si detector (β-γ timing coincidence, Figure 10.15). CsI signals outside of a 500 ns to 2750 ns time window, with respect to the Si signal, were rejected to eliminate random, non-coincident events. CsI signals were addback corrected, or adjacent CsI signals within a +/- 200 ns time gate were summed to account for Compton scattering between multiple detectors (Section 10.1.4). A total histogram was produced by summing the individual detector histograms (Figure 10.9). All peaks in the total histogram were fit with a multi-Gaussian function with the addition of a background estimation (examples of the fits are shown in Figures 10.10 and 10.11). The fit results are tabulated in Table 10.1.

Transition	**Observed Photopeak Energy (keV)**	**Integral Value (counts)**
**($1/2_1^- \rightarrow 3/2_1^-$)	1120.29	5881.7 ± 1185.5
*($1/2_1^- \rightarrow 3/2_1^-$)	1643.0 ± 3.4	67046.0 ± 3146.6
($1/2_1^- \rightarrow 3/2_1^-$)	2117.0 ± 0.2	184850.0 ± 758.9
*($1/2_1^+ \rightarrow 1/2_1^-$)	4150.1 ± 8.1	4133.9 ± 464.5
($1/2_1^+ \rightarrow 1/2_1^-$)	4602.8 ± 13.9	7772.07 ± 1899.9
*($3/2_1^+ \rightarrow 1/2_1^-$)	5311.6 ± 7.1	6570.4 ± 1460.5
($3/2_1^+ \rightarrow 1/2_1^-$)	5792.5 ± 4.8	10921.2 ± 1454.9
*($1/2_1^+ \rightarrow 3/2_1^-$)	6254.4 ± 4.2	11638.8 ± 2157.0
($1/2_1^+ \rightarrow 3/2_1^-$)	6790.4 ± 6.8	18625.7 ± 1409.0
*($3/2_1^+ \rightarrow 3/2_1^-$)	7419.8 ± 5.4	5341.2 ± 1198.7
($3/2_1^+ \rightarrow 3/2_1{}^-$)	7962.2 ± 9.2	7094.3 ± 268.1

Table 10.1: The observed energies and integral values for the photopeaks, the first escape peaks (*), and the second escape peaks (**) in the ^{11}Be($\beta^-\gamma$)^{11}B γ-ray histogram. the first column shows the γ-ray transitions (Figure 10.4). The uncertainties in the integral values were inflated by the $\sqrt{\chi^2/\nu}$ of the fit used to obtain the integral values.

The primary method of beam normalization was counting the total number of β particles in the Si detector during the beam-off cycles. A total of 8.83x10^6 β particles were recorded during the beam-off cycles, after Si background corrections. A secondary method of beam normalization was performed by fitting the beam related events in the beam-on Si spectrum (Figure 10.12). ^{8}Li contaminants punched through the Si detector, making the main peak of the Si beam-on histogram purely ^{11}Be events. Using this, a total of 7.488x10^6 beam particles were found to be implanted in the Si during the beam-on time of the experiment. The number of decays during each beam cycle is determined via

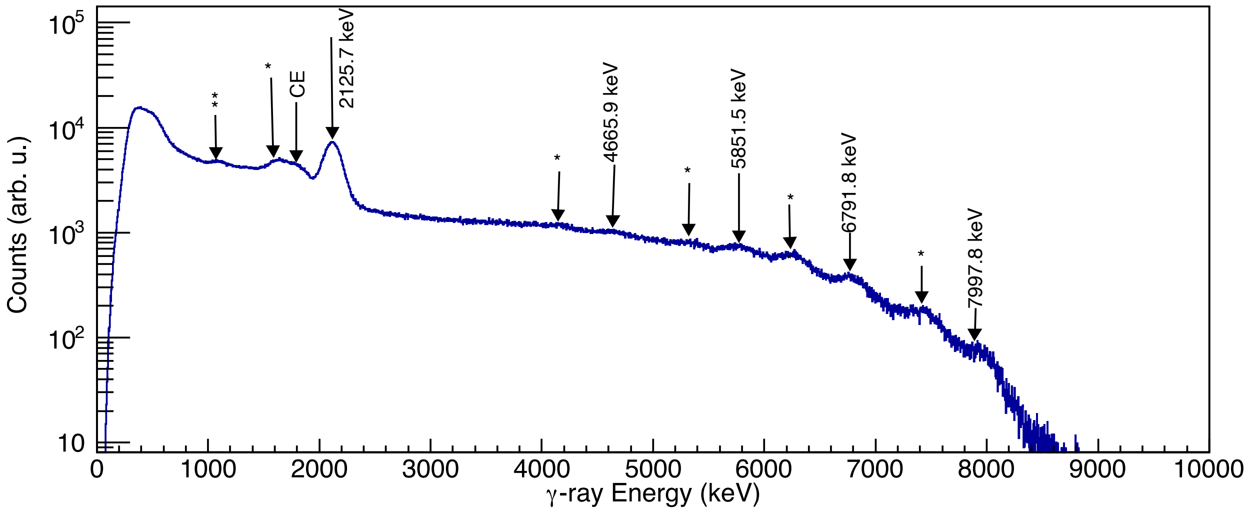

Figure 10.9: Labelled experimental γ-ray histogram for the ^{11}Be($\beta^{-}\gamma$)^{11}B decay. Asterisk (*) peaks are single escape peaks. CE is the Compton edge for the 2124.7 keV photopeak. The energies represent γ-ray photopeaks cascading from the three strongly populated excited states (2124.7 keV, 6791.8 keV, and 7997.8 keV).

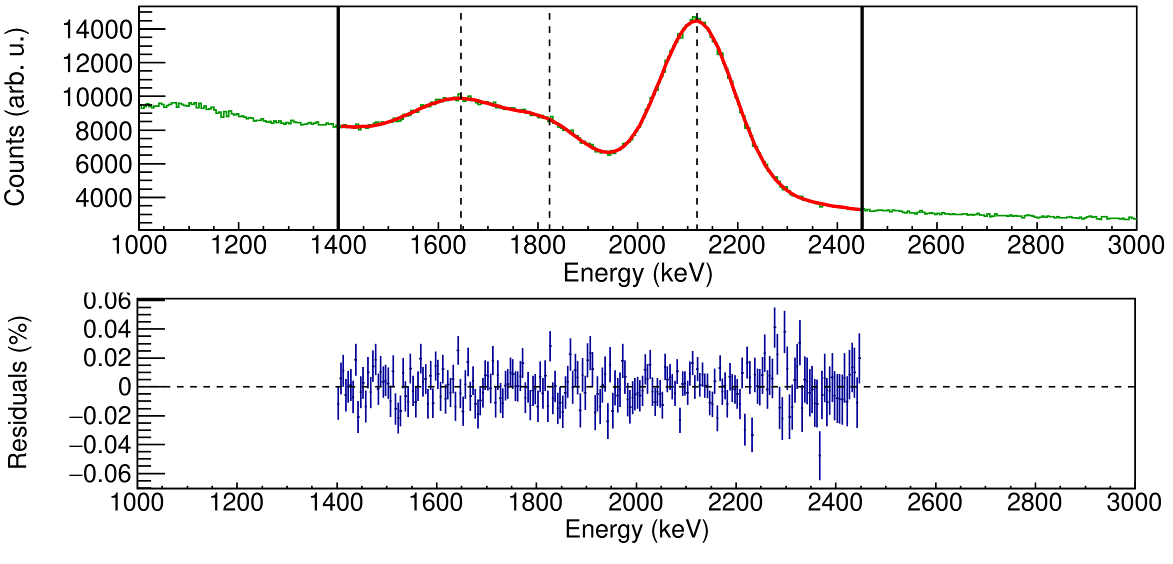

Figure 10.10: A triple Gaussian function with a quadratic background estimation to fit the 2124.7 keV photopeak as well as the first escape peak and the Compton edge. The fit has a χ^2/ν=1.226. The residual plot underneath the histogram shows the relative error of the fit compared to each bin in the histogram.

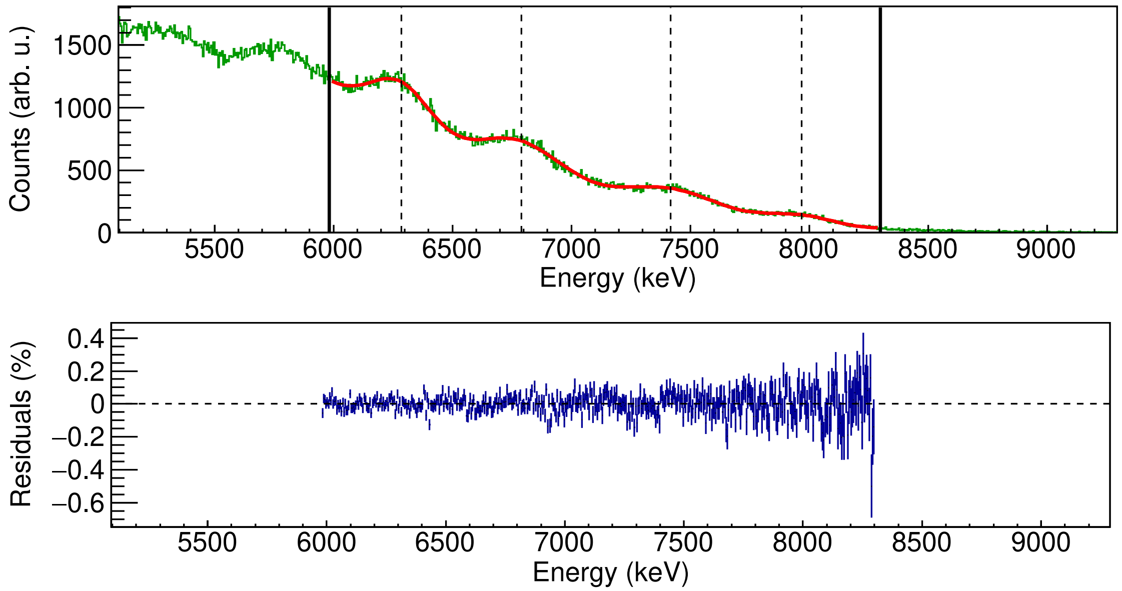

Figure 10.11: A quadruple Gaussian function with a quadratic background estimation to fit the 6791.8 keV and 7997.8 keV γ rays as well as their escape peaks. The fit has a χ^2/ν=1.17. The residual plot underneath the histogram shows the relative error of the fit compared to each bin in the histogram.

$$N = 1 - e^{-\lambda t}, \tag{10.4}$$

where λ is the decay constant and t is the mean lifetime. For each 30 second cycle, 77.9% implanted ^{11}Be ions have decayed. Since we are cycling on and off and the implanted particles decay during both cycles, the total number of implanted particles can be estimated by adjusted by twice the number of decayed particles (77.9%·77.9%=60.6%). This results in a total of 4.544x10^6 ^{11}Be decays during the experiment. The two beam normalization methods disagree in the total number of decays during the experiment. The reason for this discrepancy is unknown, but it may come from beam implantation on the Si detector frame or beamline. Instead of relying on either normalization method, the efficiencies were calculated using the second normalization method and inflated to match the efficiency curve found with the GEANT4 simulation (Section 10.3.3).

Using the second method of normalization, a total of 4.544x10^6 ^{11}Be decays were observed.

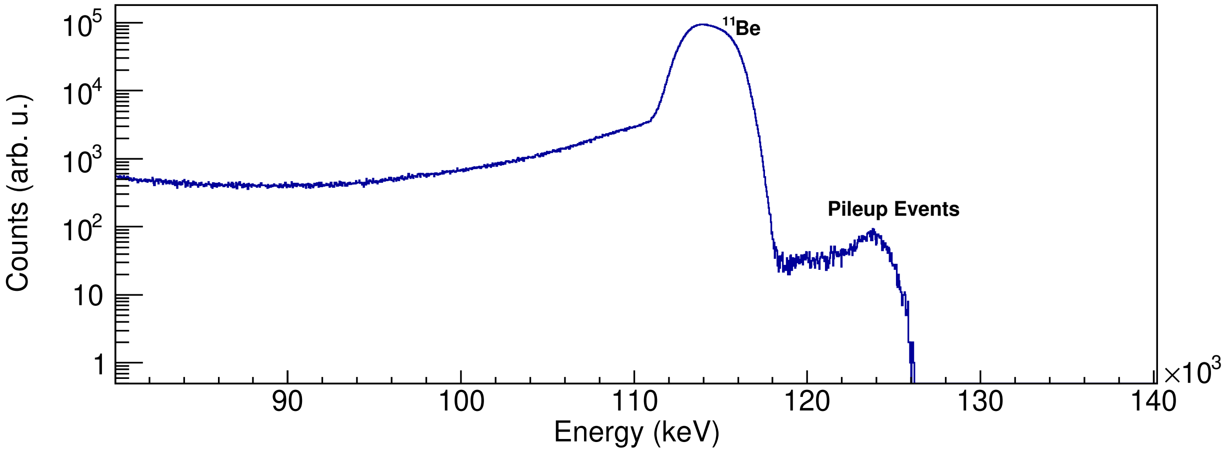

Figure 10.12: Beam-on histogram for the Si detector for one half of the total data collected during the experiment. The energy calibration was performed using the multinuclide source (Section 10.2) and extrapolated to over 100 MeV. Therefore, the energies observed in the Si beam-on spectrum are shifted from the correct energy values. Beam related events were confirmed with the Si beam-off spectrum.

The β-decay branches and the relative γ-ray intensities are known [13] (Figure 10.4). Since the 7997.8 keV and the 6791.8 keV states are only fed via β decay, calculating the expected number of events for the γ-ray cascades is straight forward. The ratio of the integral values (Table 10.1) and the expected number of events becomes the absolute efficiency (Table 10.2).

The 2124.7-keV first excited state is fed directly via β decay as well as γ-ray cascades from higher energy states. To take this into account, the contribution from the β feeding into 2124.7 keV state is calculated the same way as the other states and the γ-ray cascades are calculated from the β-branch to the initial excited state and the relative γ-ray intensity feeding to the 2124.7 keV state. The sum of all of the expected number of events becomes the total number of expected events in the 2124.7 keV photopeak. The ratio of the integral value (Table 10.1) for the 2124.7 keV photopeak and the total number of expected events becomes the absolute γ-ray efficiency (Table 10.3).

γ-ray Energy (keV)	**β Branch (%)**	**Rel. γ-ray Intensity (%)**	**Number of Expected Events**	**γ-ray Efficiency (%)**
4665.9	6.47(45)	28.5(11)	8.38(67)x10^4	9.28(74)
5851.5	4.0(3)	53.2(12)	9.67(76)x10^4	11.3(17)
6791.8	6.47(45)	67.5(11)	1.98(14)x10^5	9.39(98)
7997.8	4.0(3)	46.2(11)	8.40(66)x10^4	8.45(74)

Table 10.2: Calculations for the γ-ray efficiencies for the 4665.9 keV and 5851.5 keV γ-ray transitions and the 6791.8 keV and 7997.8 keV excited states (γ-ray transitions to the ground state). The efficiencies were calculated as the ratio of the integral values (Table 10.1) and the expected number of events for each of the energies.

The γ-ray efficiencies for the three strongly fed states were found to be: $\varepsilon_{2124.7}$=11.48(66)%, $\varepsilon_{6791.8}$=9.39(98)%, and $\varepsilon_{7977.8}$=8.45(74)%. When comparing to the simulated γ ray efficiencies, the ratio of efficiencies relative to the 2124.7 keV photopeak efficiency are in agreement (Table 10.4). A comparison between the ratio of escape peak to photopeak integral values was made between the GEANT4 simulated and the experimental ^{11}Be($\beta^-\gamma$)^{11}B decay data. Agreement between these ratios provides additional evidence for the accuracy of the GEANT4 simulated data (Figure 10.13). Further, intrinsic γ-ray efficiencies were calculated for each of the individual crystals and averaged for four rings of CsI detectors along the beam axis (Figure 10.14). Using the second method of beam normalization, the averaged intrinsic efficiencies were found to be 25.3(49)%, 27.1(49)%, 26.5(92)%, and 4.8(14)% for rings 1, 2, 3, and 4, respectively, for the 2.1 MeV state in ^{11}B. For the first three rings, the efficiencies agree well with those of the inflated GEANT4 γ-ray efficiency curve. It should be noted that the target (i.e. the Si detector) was not properly placed in the center of the array. As a result, the γ-ray detection coverage was lower than the anticipated, likely resulting in a lower absolute detection efficiency than expected. The cause of the lower efficiency found for the fourth ring is unknown, however it may be partially due to the CsI detectors being obstructed by the target arm. The comparisons between GEANT4 and experimental data, as well as the analysis of the intrinsic γ-ray efficiencies, implies accuracy in the constructed inflated GEANT4 γ-ray efficiency curve. Therefore, the experimental γ-ray efficiencies were inflated by the average ratio of efficiencies between experiment and simulation (inflation factor of 1.79) to produce: $\varepsilon_{2124.7}$=20.6(12)%, $\varepsilon_{6791.8}$=16.8(17)%, and $\varepsilon_{7977.8}$=15.1(13)%. Further, the inflated γ-ray efficiencies for the γ-ray cascades to the first excited state were found to be: $\varepsilon_{4665.5}$=16.6(13)%, $\varepsilon_{5851.5}$=20.2(31)%.

γ-ray Energy (keV)	**β Branch (%)**	**Rel. γ-ray Intensity (%)**	**Number of Expected Events**	**γ-ray Efficiency (%)**
2124.7	31.4(18)	100	1.43(8)x10^6	–
2895.6 ($3/2_2^- \rightarrow 1/2_1^-$)	0.282(20)	14.4(6)	1.85(10)x10^3	–
4665.9 ($1/2_1^+ \rightarrow 1/2_1^-$)	6.47(45)	28.5(11)	8.38(67)x10^4	–
5851.5 ($3/2_1^+ \rightarrow 1/2_1^-$)	4.0(3)	53.2(12)	9.67(76)x10^4	–
–	–	Total	1.61(9)x10^6	11.48(66)

Table 10.3: The calculation for the γ-ray efficiency for the 2124.7-keV first excited state. The expected number of events, according to the number of β particles observed during the experiment, is calculated and compared to the observed integral value for the 2124.7 keV photopeak (Table 10.1) to determine the γ-ray efficiency. The contribution from the β decay directly into the state is calculated in the first row. The three additional rows calculate the contribution from γ-ray cascades into the 2124.7 keV state from higher lying states. The last row, the total, is the sum of all expected events from the β decay and γ-ray cascades.

State (E_x) **(keV)**	**GEANT4** $\varepsilon/\varepsilon_{2124.7}$	**Experiment** $\varepsilon/\varepsilon_{2124.7}$
2124.7	1	1
6791.8	0.79(3)	0.82(10)
7997.8	0.78(6)	0.73(8)

Table 10.4: Comparison of γ-ray efficiency ratios for GEANT4 simulations and experimental data. The ratios are relative to the efficiency at 2124.7 keV. The experimental ratios are in agreement with those found with the GEANT4 simulations.

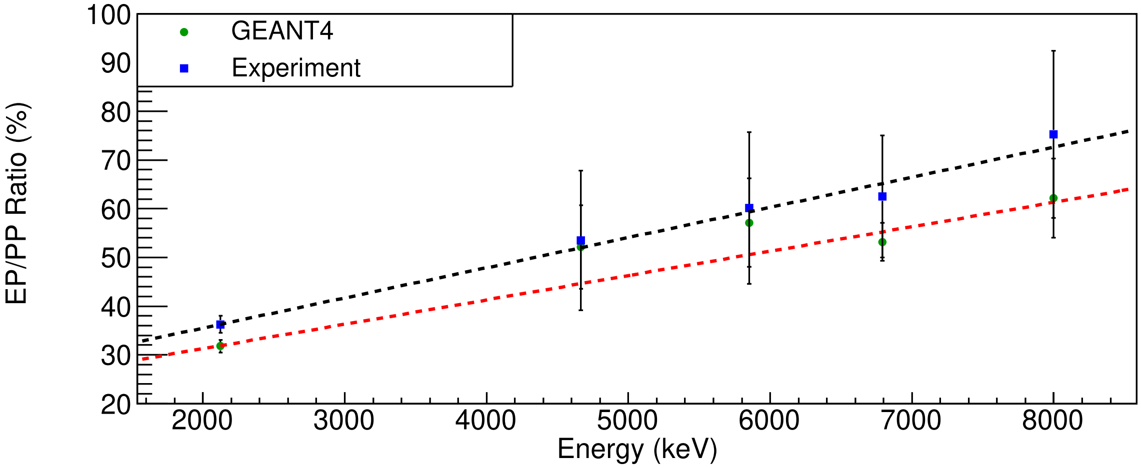

Figure 10.13: Comparison of the escape peak (EP) to photopeak (PP) ratios for the ^{11}Be($\beta^-\gamma$)^{11}B decay between GEANT4 simulations and experimental data. The ratios are in agreement with the furthest deviation of less than 2σ. The comparison of these ratios supports the accuracy of the GEANT4 simulations.

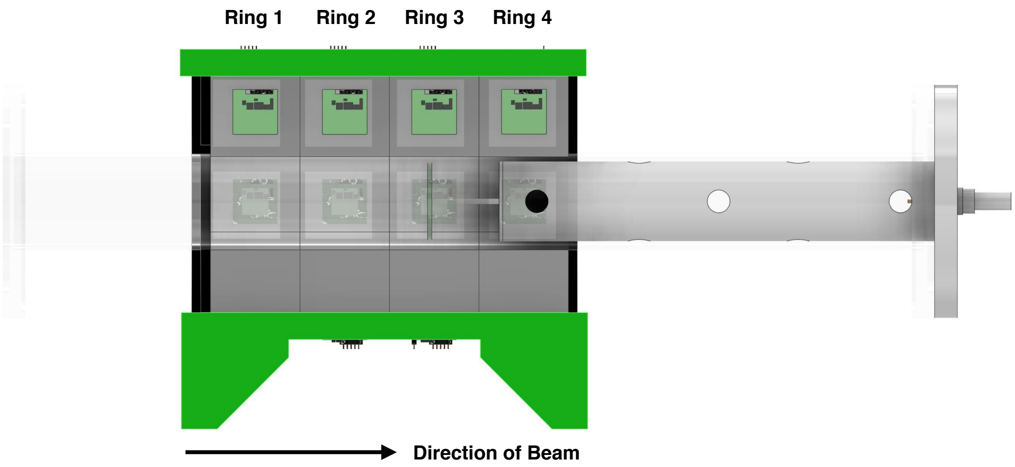

Figure 10.14: A CAD drawing that shows the location of the four CsI rings as well as the rough location of the Si detector, which also acted as the target, during the ^{11}Be($\beta^{-}\gamma$)^{11}B decay experiment. The Si detector was roughly positioned in the center of the third ring of CsI detectors. One row of CsI detectors are transparent to show the target arm assembly and the target location.

10.3.2.4 $\beta - \gamma - \gamma$ *Coincidences*

$\gamma - \gamma$ coincidences are a powerful tool to determine and verify γ-ray cascades. $\beta - \gamma$ coincidences, coincidences between the Si detector an a CsI detector, helps to remove uncorrelated events from the final histogram. Only CsI events that are directly related to an event in the Si, or a random coincidence event, are kept while the rest of the events are filtered out. The $\beta - \gamma$ coincidence gate was set between 500 ns and 2750 ns (Figure 10.15). The $\gamma - \gamma$ coincidence gate was set to +/- 200 ns which encompasses the range of correlated cascade events for the ^{60}Co source (Figure 10.16).

For the ^{11}Be($\beta^{-}\gamma$)^{11}B decay, β-γ-γ coincidences were be used to corroborate γ-ray cascades observed in the β-γ coincidence histogram (Figure 10.17). β-γ-γ coincidence matrices can be constructed to verify and assist in building more complex decay schemes with an abundance of γ-ray cascades, such as in [22].

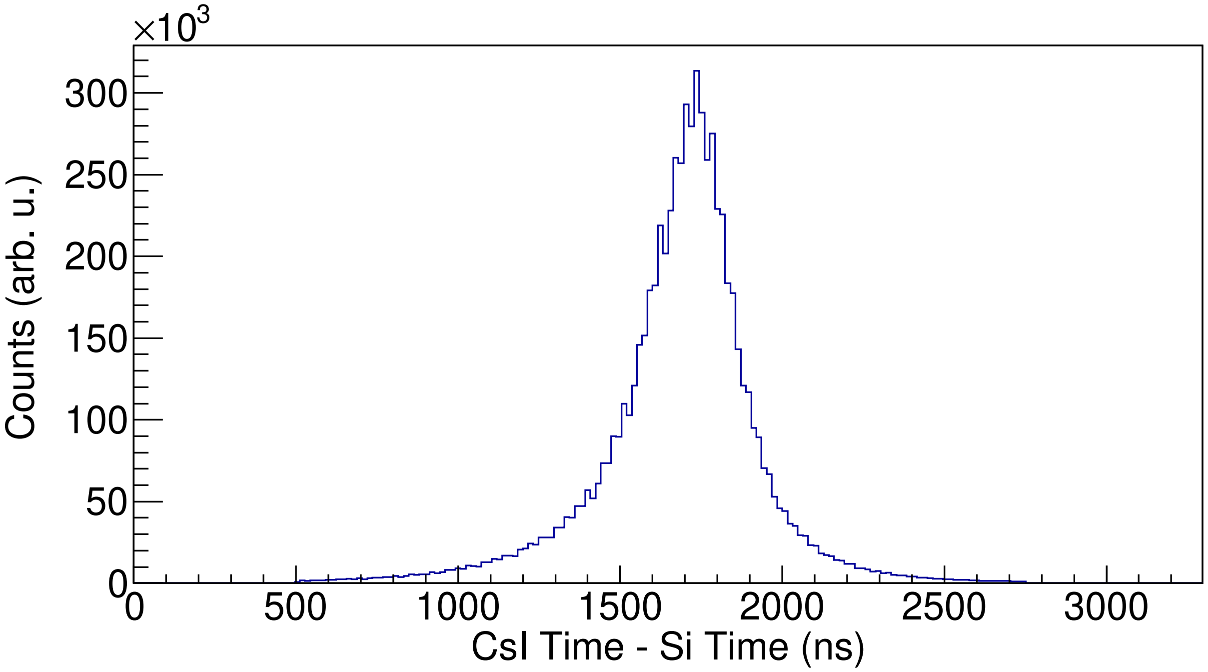

Figure 10.15: The CsI-Si timing histogram for the ^{11}Be($\beta^{-}\gamma$)^{11}B decay. The timing gate between β particle and γ ray events was set between 500 ns and 2750 ns to encompass off β-decay events while eliminating events that originate from background and noise.

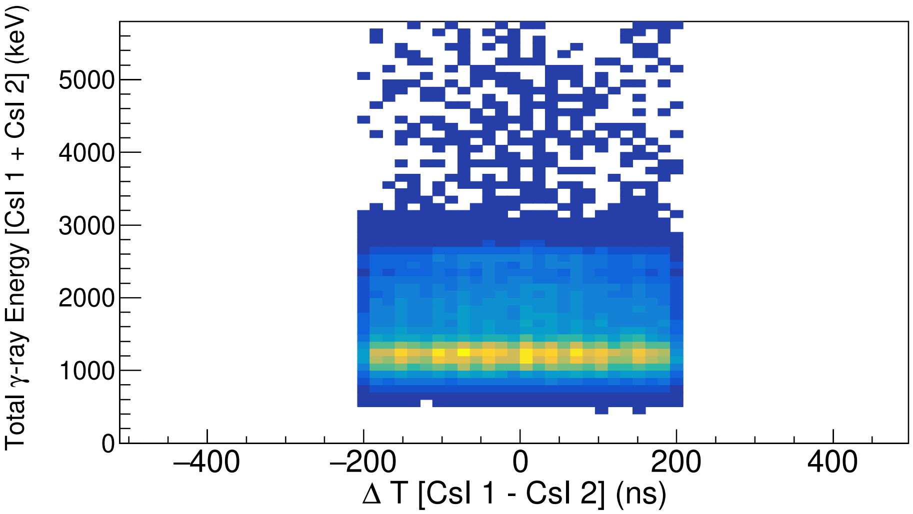

Figure 10.16: CsI-CsI timing histogram for a ^{60}Co source. The time difference between two CsI detectors is plotted against the sum of the γ-ray energy of the two CsI detectors. The CsI timing gate is set to +/- 200 ns, which is wide enough to encompass all coincidence events for the ^{60}Co source.

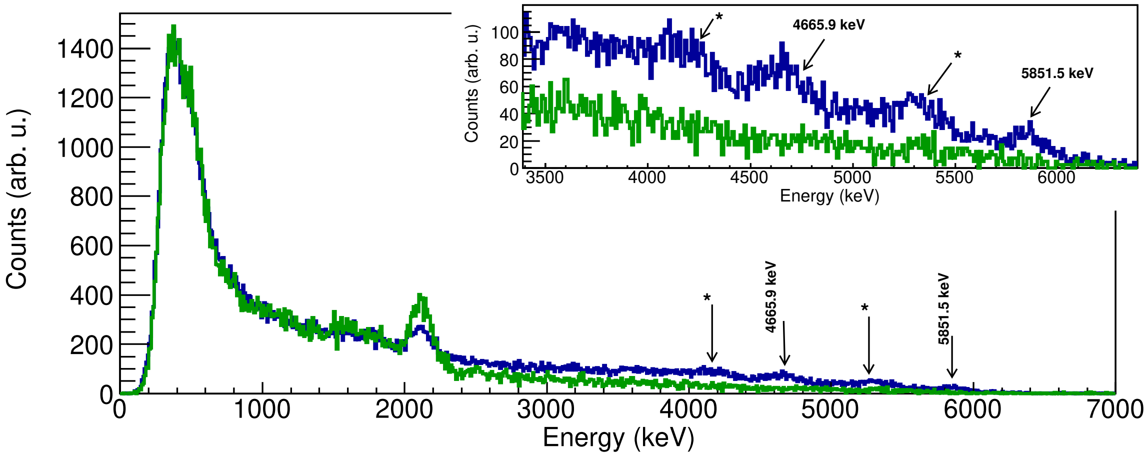

Figure 10.17: $\beta-\gamma-\gamma$ histogram (blue online) gated (+/- 60 keV) on the 2124.7 keV photopeak for the experimental ^{11}Be($\beta^{-}\gamma$)^{11}B decay data. A background histogram (green online) was produced using the same energy gate on the background next to the 2124.7 keV photopeak to estimate the coincidence background. The two photopeaks at 4665.9 keV and 5851.5 keV are present as well as their first escape peaks (labelled with an *) and are clearly identifiable above the estimated background. Both of these γ rays are a result of γ-ray cascades from higher energy excited states.

10.3.3 Monoenergetic GEANT4 Simulations

GEANT4 simulations were conducted for TexCAAM to estimate the absolute γ-ray detection efficiency for an array of energies spanning from 1 MeV to 9 MeV. The efficiency was simply calculated by taking the ratio of the photopeak counts and the number of γ rays produced. The γ-ray efficiencies were scaled by the average ratio of experimental and simulated γ-ray efficiencies found for the ^{60}Co source (0.700, Section 10.3.1). The γ-ray efficiencies found with the monoenergetic GEANT4 simulations were fit with an seventh order polynomial (χ^2/ν=0.364) to reconstruct the trend and allow for accurate interpolation (Figure 10.18). The efficiency curve was compared to a previous CsI γ-ray efficiency study [14] and the γ-ray efficiencies found for the ^{60}Co and the ^{11}Be($\beta^{-}\gamma$)^{11}B decay data.

10.4 Efficiency Curve Systematic Uncertainty

The uncertainties for the absolute γ-ray efficiencies were found purely based off of the statistical uncertainty in the fits and the statistics of the histograms. However, systematic uncertainties

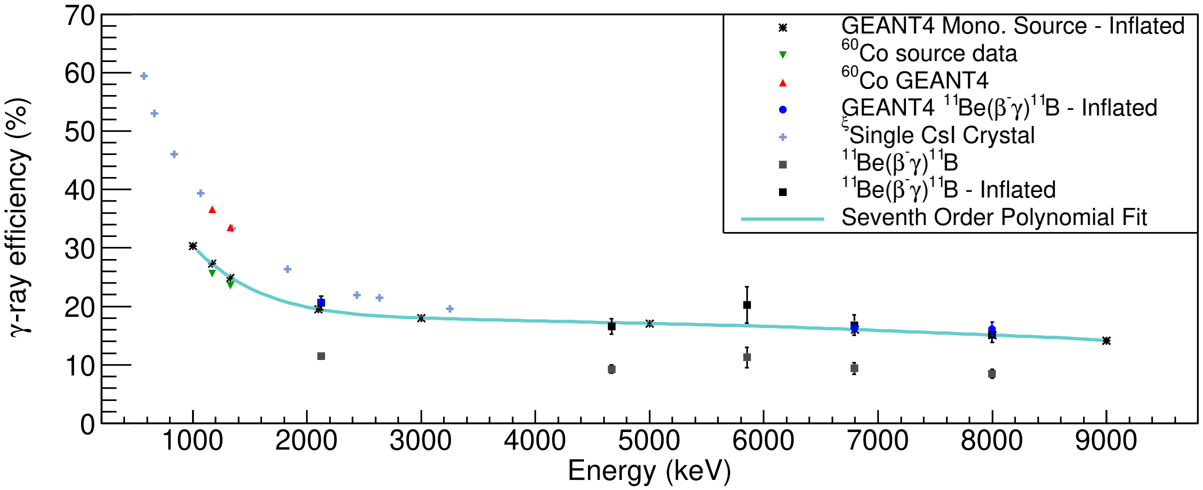

Figure 10.18: The absolute γ-ray efficiency curve constructed for TexCAAM. The γ-ray efficiencies found with the monoenergetic GEANT4 simulations (black asterisks) were inflated by the average ratio between the experimental ((green online) upside down triangles) and simulated ((red online) triangles) ^{60}Co source data (inflation ratio of 0.700). The monoenergetic efficiencies were fit with an seventh order polynomial (cyan online) (χ^2/ν=0.364) to allow for accurate interpolation. The ξ data ((blue online) crosses) are photopeak efficiencies for a single 2"x2" CsI(Tl) crystal [14]. The (blue online) circles are γ-ray efficiencies for the ^{11}Be($\beta^-\gamma$)^{11}B decay found via GEANT4 simulations and inflated by the same 0.700 factor. The (red online) squares are the γ-ray efficiencies found directly from the analysis of the experimental ^{11}Be($\beta^-\gamma$)^{11}B decay. As described in Section 10.3.2.3, the γ-ray efficiencies from the experimental ^{11}Be($\beta^-\gamma$)^{11}B decay data were inflated (black squares) to match the monoenergetic GEANT4 efficiencies.

also have to be addressed. To calculate the systematic uncertainties in the γ-ray efficiencies, the maximal deviation between the efficiency curve and the experimental data points for the ^{60}Co source and the three main γ-rays from the ^{11}Be($\beta^{-}\gamma$)^{11}B decay were taken as the systematic uncertainties. An uncertainty envelope was produced based off of these systematic uncertainties to encompass the entirety of the γ-ray efficiency curve (Figure 10.19). The systematic uncertainties will be folded into the total uncertainties for the γ-ray intensities found with TexCAAM in future experiments.

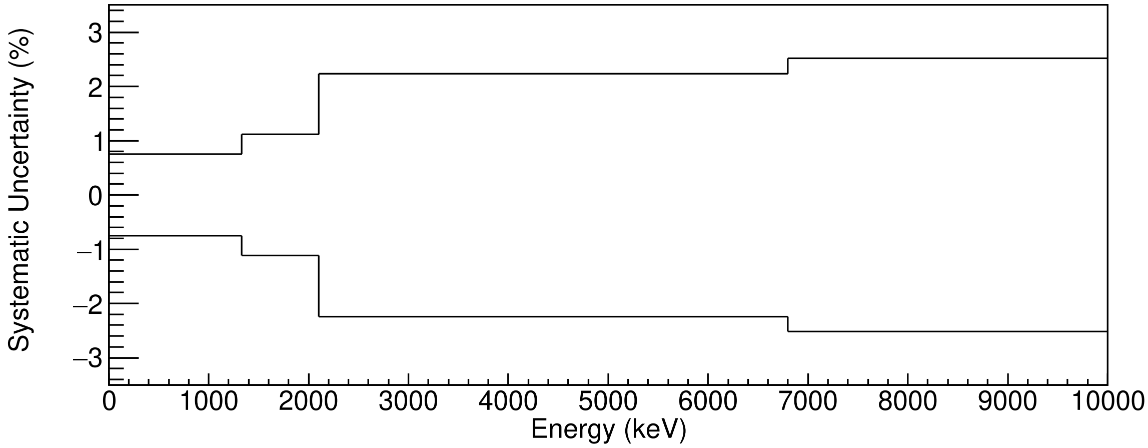

Figure 10.19: Systematic uncertainty envelope for the absolute γ-ray efficiencies found for TexCAAM.

III CONCLUSION AND OUTLOOK

11. CONCLUSIONS

The MCNP6 simulations for the next-generation fast neutron detector have illuminated the possibility of using a large-scale *p*-terphenyl scintillator array for portal monitoring. Unlike current-generation portal monitors, the proposed detector doesn't rely on increasingly rare ^{3}He nor does it rely on fast neutron thermalization. Instead, fast neutrons can be directly detected allowing for source localization and the use of active interrogation techniques. To determine the viability of such a detector, MCNP6 simulations were used to accurately reconstruct the environments expected in portal monitoring situations by simulating real-world ambient neutron measurements as well as appropriate thermal neutron induced fission of special nuclear materials (SNMs). The proposed detector, used as a singular neutron counter, was compared to current-generation thermal neutron detectors. It was found that, if accounting for the volume difference between the proposed detector and the current-generation detectors, the neutron detection efficiency may be up to $\sim$10 times higher than current-generation thermal neutron detectors. The utilization of the Uniformly Most Powerful Bayesian Tests (UMPBT) statistical model increases the neutron detection confidence levels by orders of magnitude above the confidence levels observed for current-generation thermal neutron detectors. Using the statistical model, it was also found that an $\sim$81 mg HEU (^{235}U) source may be positively identified in as little as 192 seconds. Construction of *pseudo*-bars for a full-scale neutron detector is currently underway. Testing of the neutron detector in fundamental science applications is planned for this winter. Testing of the neutron detector for portal monitoring purposes may be done to confirm the results of the MCNP6 simulations.

Various techniques were produced and used to develop and characterize TexCAAM. TexCAAM consists of an array of 32 CsI(Tl) γ-ray detectors and a target arm that contains a lithium foil target backed by a Si-SiPM telescope. The Si detector acts as confirmation gate, detecting the light ejectile particle coming from a reaction, or as a β-decay counter. The SiPMs are used as a veto to reject events where a particle punches through the Si detector. TexCAAM has $\sim$90.5% solid angle coverage for γ-ray detection and has absolute γ-ray efficiencies adequate for the series of reactions of interest. An array of GEANT4 simulations were used to estimate the γ-ray efficiencies and were confirmed via ^{60}Co source data and the ^{11}Be($\beta^{-}\gamma$)^{11}B decay data. An analysis suite was constructed to assist in the analysis of TexCAAM data through data reduction, histogram analysis, GEANT4 simulations, and theoretical calculations. A number of critical analysis steps including peak fitting, FRESCO calculations, and GEANT4 simulations have already been implemented, needing only adjustments and/or inputs in order to complete many of the analyses that TexCAAM is intended for.

Studying specific reactions, such as the ^{7}Be(^{6}Li, $d\gamma$)^{11}C reaction, are of great interest for TexCAAM. Constraining the reaction rate of the ^{7}Be(α, γ)^{11}C reaction can illuminate the ^{12}C production issue in pop-III stars. Further, the ^{7}Li(^{6}Li, $d\gamma$)^{11}B reaction, the analogue to the ^{7}Be(^{6}Li, $d\gamma$)^{11}C reaction, can be used to verify the results for the ^{7}Be(α, γ)^{11}C reaction rate as well as determine the reaction rate for the ^{7}Li(α, γ)^{11}B reaction. Resonance reactions may also be studied with TexCAAM in order to determine the nuclear structure of important isotopes such as ^{11,12}N, ^{18}Ne, and ^{8}B. The study of well-known reactions, such as the ^{12}C(^{6}Li, $d\gamma$)^{16}O reaction, can be performed to further verify the functionality and characterization of TexCAAM. As it stands, TexCAAM is ready to study the sub-Coulomb α-transfer reactions and resonance reactions of interest. TexCAAM will become the first detector in the community designed and used to study sub-Coulomb α-transfer reactions with rare-isotope beams.

REFERENCES

[1] K. S. Krane, D. Halliday, *et al.*, *Introductory nuclear physics*, vol. 465. Wiley New York, 1988.

[2] D. Brown, M. Chadwick, R. Capote, and *et al.*, "Endf/b-viii.0: The 8th major release of the nuclear reaction data library with cielo-project cross sections, new standards and thermal scattering data," *NUCL DATA SHEETS*, vol. 148, pp. 1 – 142, 2018. Special Issue on Nuclear Reaction Data.

[3] M. Chadwick, M. Herman, and et al., "Endf/b-vii.1 nuclear data for science and technology: Cross sections, covariances, fission product yields and decay data," *NUCL DATA SHEETS*, vol. 112, no. 12, pp. 2887 – 2996, 2011. Special Issue on ENDF/B-VII.1 Library.

[4] M. Salaris and S. Cassisi, *Evolution of stars and stellar populations*, vol. 400. Wiley Online Library, 2005.

[5] C. E. Rolfs, W. S. Rodney, and W. S. Rodney, *Cauldrons in the cosmos: Nuclear astrophysics*. University of Chicago press, 1988.

[6] P. Marigo, L. Girardi, C. Chiosi, and P. R. Wood, "Zero-metallicity stars I. Evolution at constant mass," *Astronomy and Astrophysics*, vol. 371, pp. 152–173, 2001.

[7] M. Wiescher, J. Görres, S. Graff, L. Buchmann, and F.-K. Thielemann, "THE HOT PROTON-PROTON CHAINS IN LOW-METALLICITY OBJECTS," *The Astrophysical Journal*, vol. 343, pp. 352–364, 1989.

[8] P. Descouvemont, "The ^{7}Be(α, γ)^{11}C and ^{7}Li(α, γ)^{11}B reactions in a microscopic three-cluster model," *Nuclear Physics, Section A*, vol. 584, no. 3, pp. 532–546, 1995.

[9] G. R. Caughlan, W. A. Fowlert, G. R. Caughlan, and W. A. Fowler, "Atomic Data and Nuclear Data Tables," *Atomic Data and Nuclear Data Tables*, vol. 40, no. 2, pp. 283–334, 1988.

[10] J. Kelley, E. Kwan, J. Purcell, C. Sheu, and H. Weller, “Energy levels of light nuclei A=11,” *Nuclear Physics A*, vol. 880, pp. 88–195, 2012.

[11] N. Glendenning, *Direct nuclear reactions*. Elsevier, 2012.

[12] H. Jayatissa, *α-CAPTURE REACTION RATES FOR ^{22}Ne(α,N)^{25}Mg AND ^{22}Ne(α,γ)^{26}Mg REACTIONS VIA SUBCOULOMB α-TRANSFER AND THEIR EFFECTS ON FINAL ABUNDANCES OF S-PROCESS ISOTOPES*. PhD thesis, 2019.

[13] D. Millener, D. Alburger, E. Warburton, and D. Wilkinson, “Decay scheme of ^{11}Be,” *Physical Review C*, vol. 26, no. 3, p. 1167, 1982.

[14] M. Irfan and R. Prasad, “Relative photopeak efficiencies and photofractions of a 2" x 2” CsI(Tl) crystal,” *Nuclear Instruments and Methods*, vol. 88, no. 2, pp. 165–176, 1970.

[15] S. S. M. Wong, *Introductory nuclear physics*. Wiley Online Library, 1998.

[16] R. T. Kouzes, J. H. Ely, L. E. Erikson, W. J. Kernan, A. T. Lintereur, E. R. Siciliano, D. C. Stromswold, and M. L. Woodring, “Alternative neutron detection testing summary,” tech. rep., Pacific Northwest National Lab.(PNNL), Richland, WA (United States), 2010.

[17] C. Iliadis, *Nuclear physics of stars*. John Wiley & Sons, 2015.

[18] F. Soddy, “The interpretation of radium and the structure of the atom, (1909), reprint edition,” 1922.

[19] B. A. Brown, “Lecture notes in nuclear structure physics,” November 2005.

[20] W. Nazarewicz, “Lecture notes in fission,” February 2018.

[21] P. Möller, D. Madland, A. Sierk, and A. Iwamoto, “Nuclear fission modes and fragment mass asymmetries in a five-dimensional deformation space,” *Nature*, vol. 409, no. 6822, pp. 785–790, 2001.

[22] E. Aboud, M. Bennett, C. Wrede, M. Friedman, S. Liddick, D. Pérez-Loureiro, D. Bardayan, B. Brown, A. Chen, K. Chipps, *et al.*, “Toward complete spectroscopy using β decay: The example of ^{32}Cl($\beta\gamma$)^{32}S,” *Physical Review C*, vol. 98, no. 2, p. 024309, 2018.

[23] G. F. Knoll, *Radiation detection and measurement*. John Wiley & Sons, 2010.

[24] T. Yanagida, K. Watanabe, and Y. Fujimoto, "Comparative study of neutron and gamma-ray pulse shape discrimination of anthracene, stilbene, and p-terphenyl," *NUCL INSTRUM METH A*, vol. 784, pp. 111–114, 2015.

[25] "What is an sipm and how does it work?." `https://hub.hamamatsu.com/jp/en/technical-note/how-sipm-works/index.html`.

[26] M. L. Roush, M. Wilson, and W. F. Hornyak, "Pulse shape discrimination," *Nuclear Instruments and Methods*, vol. 31, no. 1, pp. 112–124, 1964.

[27] T. Sanderson, C. Scott, M. Flaska, J. Polack, and S. Pozzi, "Machine learning for digital pulse shape discrimination," in *2012 IEEE Nuclear Science Symposium and Medical Imaging Conference Record (NSS/MIC)*, pp. 199–202, IEEE, 2012.

[28] R. T. Kouzes, E. R. Siciliano, J. H. Ely, P. E. Keller, and R. J. McConn, "Passive neutron detection for interdiction of nuclear material at borders," *NUCL INSTRUM METH A*, vol. 584, no. 2, pp. 383 – 400, 2008.

[29] J. L. Lacy, A. Anthanasiades, C. S. Martin, L. Sun, and G. J. Vazques-Flores, "Straw-Based Portal Monitor 3He Replacement Detector with Expanded Capabilities," *IEEE NUCL SCI CONF R*, pp. HE2–4, 2011.

[30] R. T. Kouzes and J. H. Ely, "PNNL-19360: Status Summary of ^{3}He and Neutron Detection Alternatives for Homeland Security," Tech. Rep. April, 2010.

[31] D. A. Shea and D. L. Morgan, "The Helium-3 shortage: Supply, demand, and options for congress," 2010.

[32] P. E. Vanier, L. Forman, and D. R. Norman, "Thermal Neutron Imaging in an Active Interrogation Environment," *AIP CONF PROC*, vol. 1099, p. 583, 2009.

[33] C. E. Moss, C. L. Hollas, G. W. McKinney, and W. L. Myers, "Comparison of active interrogation techniques," *IEEE NUCL SCI CONF R*, vol. 1, pp. 329–332, 2005.

[34] R. C. Runkle, D. L. Chichester, and S. J. Thompson, "Rattling nucleons: New developments in active interrogation of special nuclear material," *NUCL INSTRUM METH A*, 2011.

[35] D. Dietrich, C. Hagmann, P. Kerr, L. Nakae, M. Rowland, N. Snyderman, W. Stoeffl, and R. Hamm, "A kinematically beamed, low energy pulsed neutron source for active interrogation," *NUCL INSTRUM METH B*, vol. 241, pp. 826–830, 2005.

[36] C. A. Hagmann, D. D. Dietrich, J. M. Hall, P. L. Kerr, L. F. Nakae, R. J. Newby, M. S. Rowland, N. J. Snyderman, and W. Stoeffl, "Active detection of shielded SNM with 60-keV neutrons," *IEEE T NUCL SCI*, vol. 56, no. 3, pp. 1215–1217, 2009.

[37] P. Kerr, M. Rowland, D. Dietrich, W. Stoeffl, B. Wheeler, L. Nakae, D. Howard, C. Hagmann, J. Newby, and R. Porter, "Active detection of small quantities of shielded highly-enriched uranium using low-dose 60-kev neutron interrogation," *NUCL INSTRUM METH B*, 2007.

[38] P. Hausladen, M. A. Blackston, E. Brubaker, D. Chichester, P. Marleau, and R. J. Newby, "Fast neutron coded-aperture imaging of special nuclear material configurations," *53rd Annual Meeting of the INMM*, pp. 1–10, 2012.

[39] P. B. Rose, A. S. Erickson, M. Mayer, J. Nattress, and I. Jovanovic, "Uncovering Special Nuclear Materials by Low-energy Nuclear Reaction Imaging," *Sci. Rep.*, vol. 6, p. 24388, apr 2016.

[40] M. C. Hamel, J. K. Polack, M. L. Ruch, M. J. Marcath, S. D. Clarke, and S. A. Pozzi, "Active neutron and gamma-ray imaging of highly enriched uranium for treaty verification OPEN," *Sci. Rep.*, 2017.

[41] M. C. Hamel, J. K. Polack, A. Poitrasson-Rivière, M. Flaska, S. D. Clarke, S. A. Pozzi, A. Tomanin, and P. Peerani, "Stochastic image reconstruction for a dual-particle imaging system," *NUCL INSTRUM METH A*, 2016.

[42] D. Scriven, G. Christian, G. Rogachev, C. Parker, L. Sobotka, S. Ahn, G. Chubarian, S. Ota, E. Aboud, J. Bishop, E. Koshchiy, and A. Thomas, "A position and pulse shape discrimi-

nant p-terphenyl detector module," *Nuclear Instruments and Methods in Physics Research Section A: Accelerators, Spectrometers, Detectors and Associated Equipment*, vol. 1010, p. 165492, 2021.

[43] A. Sardet, C. Varignon, B. Laurent, T. Granier, and A. Oberstedt, "p-Terphenyl: An alternative to liquid scintillators for neutron detection," *NUCL INSTRUM METH A*, vol. 792, pp. 74–80, 2015.

[44] J. Iwanowska, L. Swiderski, M. Moszynski, T. Szczesniak, P. Sibczynski, Z. Galunov, and L. Karavaeva, "Neutron/gamma discrimination properties of composite scintillation detectors," *J INSTRUM*, vol. 6, no. 7, p. 7007, 2011.

[45] M. L. Ruch, M. Flaska, and S. A. Pozzi, "Pulse shape discrimination performance of stilbene coupled to low-noise silicon photomultipliers," *NUCL INSTRUM METH A*, 2015.

[46] T. Goorley, M. James, T. Booth, F. Brown, J. Bull, L. Cox, J. Durkee, J. Elson, M. Fensin, R. Forster, *et al.*, "Initial MCNP6 release overview," *NUCL TECHNOL*, vol. 180, no. 3, pp. 298–315, 2012.

[47] J. K. Shultis and R. E. Faw, "An MCNP primer," tech. rep., 2011.

[48] G. E. McMath, G. W. McKinney, and T. Wilcox, "MCNP6 Cosmic & Terrestrial Background Particle Fluxes–Release 4," tech. rep., Los Alamos National Lab.(LANL), Los Alamos, NM (United States), 2015.

[49] C. Matei, F. J. Hambsch, and S. Oberstedt, "Proton light output function and neutron efficiency of a p-terphenyl detector using a ^{252}Cf source," *NUCL INSTRUM METH A*, vol. 676, pp. 135–139, 2012.

[50] V. E. Johnson, "Uniformly most powerful bayesian tests," *ANN STAT*, vol. 41, no. 4, p. 1716, 2013.

[51] "National Nuclear Data Center, information extracted from the NuDat 2 database." `https://www.nndc.bnl.gov/nudat2/`.

[52] K. Shibata, O. Iwamoto, T. Nakagawa, N. Iwamoto, A. Ichihara, S. Kunieda, S. Chiba, K. Furutaka, N. Otuka, T. Ohsawa, T. Murata, H. Matsunobu, A. Zukeran, S. Kamada, and J. I. Katakura, "JENDL-4.0: A new library for nuclear science and engineering," *J NUCL SCI TECHNOL*, vol. 48, no. 1, pp. 1–30, 2011.

[53] G. Lemaitre, "UN UNIVERS HOMOGENE DE MASSES CONSTANTE ET DE RAYON CROISSANT RENDANT COMPTE DE LA VITESSE RADIALE DES NEBULEUSES EXTRA-GALACTIQUES," *Annales de la Société Scientifique de Bruxelles*, vol. A47, 1927.

[54] P. J. E. Peebles, "PRIMEVAL HELIUM ABUNDANCE AND THE PRIMEVAL FIREBALL," tech. rep., 1966.

[55] K. A. Olive, D. N. Schramm, G. SteigmanS, and T. P. Walker, "Big-Bang Nucleosynthesis Revisited," tech. rep., 1989.

[56] R. D. Atkinson, "Atomic Synthesis and Stellar Energy. III," *Astrophysical Journal*, vol. 84, no. 73A, 1936.

[57] H. A. Bethe, C. L. Critchfield, and H. A. Bethe, "The Formation of Deuterons by Proton Combination," tech. rep.

[58] C.-F. von Weizsäcker, "Über elementumwandlungen in innern der sterne. ii," *Physikalische Zeitschrift*, vol. 39, p. 633, 1938.

[59] F. Hoyle, M. Wilson, and P. Observatories, "ON NUCLEAR REACTIONS OCCURRING IN VERY HOT STARS. I. THE SYNTHESIS OF ELEMENTS FROM CARBON TO NICKEL," tech. rep.

[60] F. Hoyle, "THE SYNTHESIS OF THE ELEMENTS FROM HYDROGEN *," tech. rep.

[61] E. E. Salpeter, "NUCLEAR REACTIONS IN STARS WITHOUT HYDROGEN," tech. rep., 1952.

[62] K. M. Burbidge, G. R. Burmdge, A. Fowl, and F. Hqylk, "Synthesis of the Elements in Stars," tech. rep., 1957.

[63] A. G. W. Cameron, "NUCLEAR REACTIONS IN STARS AND NUCLEOGENESIS," Tech. Rep. 408, 1957.

[64] W. Baade, "109. The Resolution of Messier 32, NGC 205, and the Central Region of the Andromeda Nebula," in *A Source Book in Astronomy and Astrophysics, 1900–1975*, 1944.

[65] O. Struve, "Elementary astronomy," *New York, Oxford University Press, 1959.*, 1959.

[66] H. E. Bond, "Where is Population III?," *The Astrophysical Journal*, vol. 248, 1981.

[67] J. H. Jeans, "I. the stability of a spherical nebula," *Philosophical Transactions of the Royal Society of London. Series A, Containing Papers of a Mathematical or Physical Character*, vol. 199, no. 312-320, pp. 1–53, 1902.

[68] W. C. Saslaw and D. Zipoy, "Molecular hydrogen in pre-galactic gas clouds," *Nature*, vol. 216, no. 5119, pp. 976–978, 1967.

[69] V. Bromm and R. B. Larson, "The First Stars," *Annual Review of Astronomy and Astrophysics*, vol. 42, no. 1, pp. 79–118, 2004.

[70] N. Christlieb, M. S. Bessell, T. C. Beers, B. Gustafsson, A. Korn, P. S. Barklem, T. Karlsson, M. Mizuno-Wiedner, and S. Rossi, "A stellar relic from the early milky way," *Nature*, vol. 419, no. 6910, pp. 904–906, 2002.

[71] H. Uehara and S.-i. Inutsuka, "Does deuterium enable the formation of primordial brown dwarfs?," *The Astrophysical Journal Letters*, vol. 531, no. 2, p. L91, 2000.

[72] G. Rakavy and G. Shaviv, "Instabilities in highly evolved stellar models," *The Astrophysical Journal*, vol. 148, p. 803, 1967.

[73] G. S. Fraley, "Supernovae explosions induced by pair-production instability," *Astrophysics and Space Science*, vol. 2, no. 1, pp. 96–114, 1968.

[74] A. J. Korn, F. Grundahl, O. Richard, P. Barklem, L. Mashonkina, R. Collet, N. Piskunov, and B. Gustafsson, "A probable stellar solution to the cosmological lithium discrepancy," *Nature*, vol. 442, no. 7103, pp. 657–659, 2006.

[75] S. G. Ryan, J. E. Norris, and T. C. Beers, “The spite lithium plateau: ultrathin but postprimordial,” *The Astrophysical Journal*, vol. 523, no. 2, p. 654, 1999.

[76] M. Spite and F. Spite, “Lithium abundance at the formation of the galaxy,” *Nature*, vol. 297, no. 5866, pp. 483–485, 1982.

[77] R. H. Cyburt, B. D. Fields, and K. A. Olive, “An update on the big bang nucleosynthesis prediction for ^{7}Li: the problem worsens,” *Journal of Cosmology and Astroparticle Physics*, vol. 2008, no. 11, p. 012, 2008.

[78] M. Hartos, C. Bertulani, A. Mukhamedzhanov, S. Hou, *et al.*, “Impact of the ^{7}Be$(\alpha,\gamma)^{11}$C reaction on the primordial abundance of ^{7}Li,” *The Astrophysical Journal*, vol. 862, no. 1, p. 62, 2018.

[79] C. Angulo, M. Arnould, M. Rayet, P. Descouvemont, D. Baye, C. Leclercq-Willain, A. Coc, S. Barhoumi, P. Aguer, C. Rolfs, R. Kunz, J. W. Hammer, A. Mayer, T. Paradellis, S. Kossionides, C. Chronidou, K. Spyrou, S. Degl’Innocenti, G. Fiorentini, B. Ricci, S. Zavatarelli, C. Providencia, H. Wolters, J. Soares, C. Grama, J. Rahighi, A. Shotter, and M. Lamehi Rachti, “A compilation of charged-particle induced thermonuclear reaction rates,” *Nuclear Physics A*, 1999.

[80] G. M. Fuller, S. E. Woosley, and T. A. Weaver, “The evolution of radiation-dominated stars. I - Nonrotating supermassive stars,” *The Astrophysical Journal*, vol. 307, p. 675, 1986.

[81] R. Mitalas, “Unconventional ^{12}C production in population III stars,” *Astrophysical Journal*, vol. 290, pp. 273–275, 1985.

[82] R. V. Wagoner, “Synthesis of the elements within objects exploding from very high temperatures,” *The Astrophysical Journal Supplement Series*, vol. 18, p. 247, 1969.

[83] M. J. Harris, W. A. Fowler, G. R. Caughlan, and B. A. Zimmerman, “Thermonuclear Reaction Rates, III,” tech. rep., 1983.

[84] G. Hardie, B. W. Filippone, A. J. Elwyn, M. Wiescher, and R. E. Segel, “Resonant alpha capture by ^{7}Be and ^{7}Li,” *Physical Review C*, vol. 29, no. 4, pp. 1199–1206, 1984.

[85] E. Norbeck Jr and C. Littlejohn, "Experimental survey of nuclear transformations caused by 2-Mev lithium ions," *Physical Review*, vol. 108, no. 3, p. 754, 1957.

[86] J. Kelley, J. Purcell, and C. Sheu, "Energy levels of light nuclei A=12," *Nuclear Physics A*, vol. 968, pp. 71–253, 2017.

[87] C. Brune, W. Geist, R. Kavanagh, Veal, and KD, "Sub-coulomb α transfers on ^{12}C and the ^{12}C(α, γ)^{16}O S Factor," *Physical review letters*, vol. 83, no. 20, p. 4025, 1999.

[88] M. Avila, G. Rogachev, E. Koshchiy, L. Baby, J. Belarge, K. Kemper, A. Kuchera, A. Mukhamedzhanov, D. Santiago-Gonzalez, and E. Uberseder, "Constraining the 6.05 Mev 0+ and 6.13 Mev 3- cascade transitions in the ^{12}C(α, γ)^{16}O reaction using the Asymptotic Normalization Coefficients," *Physical review letters*, vol. 114, no. 7, p. 071101, 2015.

[89] D. Cortina-Gil, K. Markenroth, F. Attallah, T. Baumann, J. Benlliure, M. Borge, L. Chulkov, U. D. Pramanik, J. Fernandez-Vazquez, C. Forssén, *et al.*, "Experimental evidence for the ^{8}B ground state configuration," *Physics Letters B*, vol. 529, no. 1-2, pp. 36–41, 2002.

[90] V. Gol'dberg, G. Rogachev, M. Golovkov, V. Dukhanov, I. Serikov, and V. Timofeev, "Study of the proton-rich nucleus ^{8}B in the resonance scattering of radioactive ^{7}Be by hydrogen," *Journal of Experimental and Theoretical Physics Letters*, vol. 67, no. 12, pp. 1013–1017, 1998.

[91] G. V. Rogachev, J. Kolata, F. Becchetti, P. DeYoung, M. Hencheck, K. Helland, J. Hinnefeld, B. Hughey, P. Jolivette, L. Kiessel, *et al.*, "Proton elastic scattering from ^{7}Be at low energies," *Physical Review C*, vol. 64, no. 6, p. 061601, 2001.

[92] H. Yamaguchi, Y. Wakabayashi, S. Kubono, G. Amadio, H. Fujikawa, T. Teranishi, A. Saito, J. He, S. Nishimura, Y. Togano, *et al.*, "Low-lying non-normal parity states in ^{8}B measured by proton elastic scattering on ^{7}Be," *Physics Letters B*, vol. 672, no. 3, pp. 230–234, 2009.

[93] J. Mitchell, G. Rogachev, E. Johnson, L. Baby, K. Kemper, P. Peplowski, A. Volya, I. Wiedenhoever, and A. Moro, "Low-lying states in ^{8}B," *Physical Review. C, Nuclear Physics*, vol. 82, no. 1, 2010.

[94] S. Paneru, C. Brune, R. Giri, R. Livesay, U. Greife, J. Blackmon, D. Bardayan, K. Chipps, B. Davids, D. Connolly, *et al.*, “s-wave scattering lengths for the ^{7}Be+p system from an R-matrix analysis,” *Physical Review C*, vol. 99, no. 4, p. 045807, 2019.

[95] F. Ajzenberg-Selove, “Energy levels of light nuclei A=5-10,” *Nuclear Physics A*, vol. 490, no. 1, pp. 1–225, 1988.

[96] R. Robertson, W. Chien, and D. Goosman, “Complete isobaric quintet,” *Physical Review Letters*, vol. 34, no. 1, p. 33, 1975.

[97] M. Dufour and P. Descouvemont, “The ^{17}F(p,γ)^{18}Ne reaction at stellar energies,” *Nuclear Physics A*, vol. 730, no. 3-4, pp. 316–328, 2004.

[98] A. Kim, N. Lee, I. Hahn, J. Yoo, M. Han, S. Kubono, H. Yamaguchi, S. Hayakawa, Y. Wakabayashi, D. Binh, *et al.*, “Direct measurement of the ^{14}O(α,α)^{14}O cross section for astrophysically important ^{14}O+α resonances,” *Journal of the Korean Physical Society*, vol. 57, no. 1, pp. 40–43, 2010.

[99] B. Harss, C. Jiang, K. Rehm, J. Schiffer, J. Caggiano, P. Collon, J. Greene, D. Henderson, A. Heinz, R. Janssens, *et al.*, “Widths of astrophysically important resonances in ^{18}Ne,” *Physical Review C*, vol. 65, no. 3, p. 035803, 2002.

[100] A. Dreyfuss, K. Launey, J. Escher, G. Sargsyan, R. Baker, T. Dytrych, and J. Draayer, “Clustering and α-capture reaction rate from ab initio symmetry-adapted descriptions of ^{20}Ne,” *Physical Review C*, vol. 102, no. 4, p. 044608, 2020.

[101] H. Schatz, “Lecture notes in resonance reactions,” April 2013.

[102] G. R. Satchler, *Introduction to nuclear reactions*. Macmillan International Higher Education, 1990.

[103] I. Thompson, “Getting started with fresco,” *Comput. Phys. Rep*, vol. 7, pp. 167–212, 1988.

[104] P. Kunz, “Instructions for the use of dwuck: A distorted wave born approximation program.,” tech. rep., Colorado Univ., Boulder. Dept. of Physics, 1969.

[105] A. Mukhamedzhanov, H. Clark, C. A. Gagliardi, Y.-W. Lui, L. Trache, R. E. Tribble, H. Xu, X. Zhou, V. Burjan, J. Cejpek, *et al.*, "Asymptotic normalization coefficients for ^{10}B$\rightarrow$^{9}Be+p," *Physical Review C*, vol. 56, no. 3, p. 1302, 1997.

[106] G. Tabacaru, D. May, J. Arje, G. Chubarian, H. Clark, G. Kim, and R. Tribble, "Production of rare isotope beams at the Texas A&M University Cyclotron Institute," *Review of Scientific Instruments*, vol. 83, no. 2, p. 02A905, 2012.

[107] R. Tribble, A. Azhari, C. Gagliardi, J. Hardy, A. Mukhamedzhanov, X. Tang, L. Trache, and S. Yennello, "Radioactive beams at Texas A&M University," *Nuclear Physics A*, vol. 701, no. 1-4, pp. 278–281, 2002.

[108] E. Koshchiy, G. Rogachev, E. Pollacco, S. Ahn, E. Uberseder, J. Hooker, J. Bishop, E. Aboud, M. Barbui, V. Goldberg, C. Hunt, H. Jayatissa, C. Magana, R. O'Dwyer, B. Roeder, A. Saastamoinen, and S. Upadhyayula, "Texas Active Target (TexAT) detector for experiments with rare isotope beams," *Nuclear Instruments and Methods in Physics Research Section A: Accelerators, Spectrometers, Detectors and Associated Equipment*, vol. 957, p. 163398, 2020.

[109] J. F. Ziegler, M. D. Ziegler, and J. P. Biersack, "SRIM–the stopping and range of ions in matter (2010)," *Nuclear Instruments and Methods in Physics Research Section B: Beam Interactions with Materials and Atoms*, vol. 268, no. 11-12, pp. 1818–1823, 2010.

[110] O. Tarasov and D. Bazin, "LISE++: Radioactive beam production with in-flight separators," *Nuclear Instruments and Methods in Physics Research Section B: Beam Interactions with Materials and Atoms*, vol. 266, no. 19-20, pp. 4657–4664, 2008.

[111] H. Essel, J. Hoffmann, W. Ott, M. Richter, D. Schall, H. Sohlbach, and W. Spreng, "GOOSY-VME: the data acquisition and analysis system at GSI," *IEEE transactions on nuclear science*, vol. 39, no. 2, pp. 248–251, 1992.

[112] "SIS3316 16 channel VME digitizer user manual." STRUCK Documentation. Accessed: 2021-10-22.

[113] P. Siffert and A. Coche, "Low energy α-p pulse-shape discrimination with silicon surface barrier detectors," *IEEE Transactions on Nuclear Science*, vol. 13, no. 1, pp. 757–761, 1966.

[114] W.-D. Emmerich, K. Frank, A. Hofmann, A. Dittner, J. Klein, and R. Stock, "Pulse-shape discrimination with surface barrier detectors," *Nuclear Instruments and Methods*, vol. 83, no. 1, pp. 131–132, 1970.

[115] M. Mutterer, W. Trzaska, G. Tyurin, A. Evsenin, J. Von Kalben, J. Kemmer, M. Kapusta, V. Lyapin, and S. Khlebnikov, "Breakthrough in pulse-shape based particle identification with silicon detectors," in *1999 IEEE Nuclear Science Symposium. Conference Record. 1999 Nuclear Science Symposium and Medical Imaging Conference (Cat. No. 99CH37019)*, vol. 1, pp. 148–151, IEEE, 1999.

[116] K. Sjöland and P. Kristiansson, "Pile-up and defective pulse rejection by pulse shape discrimination in surface barrier detectors," *Nuclear Instruments and Methods in Physics Research Section B: Beam Interactions with Materials and Atoms*, vol. 94, no. 3, pp. 333–337, 1994.

[117] D. Dell'Aquila, S. Sweany, K. Brown, Z. Chajecki, W. Lynch, F. Teh, C.-Y. Tsang, M. Tsang, K. Zhu, C. Anderson, *et al.*, "Non-linearity effects on the light-output calibration of light charged particles in CsI(Tl) scintillator crystals," *Nuclear Instruments and Methods in Physics Research Section A: Accelerators, Spectrometers, Detectors and Associated Equipment*, vol. 929, pp. 162–172, 2019.